Linac Coherent Light Source: The first five years

Christoph Bostedt,[*] Sébastien Boutet, David M. Fritz, Zhirong Huang, Hae Ja Lee, Henrik T. Lemke,[†] Aymeric Robert, William F. Schlotter, Joshua J. Turner, and Garth J. Williams[‡]

SLAC National Accelerator Laboratory, 2575 Sand Hill Road, Menlo Park, California 94025, USA

(published 9 March 2016)

A new scientific frontier opened in 2009 with the start of operations of the world's first x-ray free-electron laser (FEL), the Linac Coherent Light Source (LCLS), at SLAC National Accelerator Laboratory. LCLS provides femtosecond pulses of x rays (270 eV to 11.2 keV) with very high peak brightness to access new domains of ultrafast x-ray science. This article presents the fundamental FEL physics and outlines the LCLS source characteristics along with the experimental challenges, strategies, and instrumentation that accompany this novel type of x-ray source. The main part of the article reviews the scientific achievements since the inception of LCLS in the five primary areas it serves: atomic, molecular, and optical physics; condensed matter physics; matter in extreme conditions; chemistry and soft matter, and biology.

DOI: 10.1103/RevModPhys.88.015007

CONTENTS

[*]Current address: Argonne National Laboratory, 9700 South Cass Avenue, Lemont, IL 60439, USA and Department of Physics and Astronomy, Northwestern University, 2145 Sheridan Road, Evanston, IL 60208, USA.

[†]Current address: Paul Scherrer Institut, CH-5232 Villigen, Switzerland.

[‡]Current address: Brookhaven National Laboratory, PO Box 5000, Upon, NY 11973, USA.

I. INTRODUCTION

On 10 April 2009, accelerator physicists working at SLAC National Accelerator Laboratory in Menlo Park, California sent an extremely high-brightness beam of 13.6 GeV electrons from the SLAC linear accelerator down a series of precisely aligned undulator magnets for the first time. After the beam traversed approximately 30 m of active undulators, lasing was observed at a wavelength of 1.5 Å. The first hard x-ray free-electron laser (FEL) was born (Emma *et al.*, 2010).

The realization of a femtosecond source of transversely coherent, high-intensity x-ray photons opened a new frontier of science. Since first light at the Linac Coherent Light Source (LCLS), as the SLAC FEL was named, extensive work has gone on to optimize the source itself and explore the limits of parameter control. In addition, experimental tools and methodologies have been developed to exploit the features of the x-ray FEL as a probe for numerous science areas and to shed light on atomic, molecular, and optical physics, condensed matter physics, chemistry and soft condensed matter, matter in extreme conditions, and biology (White, Robert, and Dunne, 2015).

This review focuses on what was accomplished in the first five years of LCLS operations, including a brief review of work at previous free-electron lasers with longer wavelengths that was particularly influential on the development of LCLS. It concludes with a look at what is to come in the next decade as major new hard x-ray FEL facilities turn on and the science served by these tools starts to approach maturity.

A. Brief history of x-ray FELs

The free-electron laser was invented by Madey (1971) and subsequently demonstrated experimentally by his group at Stanford University in the 1970s (Deacon *et al.*, 1977).

A free-electron laser exploits the interaction between a relativistic beam of electrons and the radiation emitted as the beam passes through a periodic magnetic structure. The result of the interaction is to pump energy from a wide bandwidth and unphased reservoir (the relativistic electron beam) into one particular mode of an electromagnetic wave. In this general sense, the FEL does what traditional lasers do, and hence it is called a laser. However, the FEL effect does not rely on quantum effects such as atomic energy levels or stimulated emission. FELs now operate over a very wide range of wavelengths—from microwaves through terahertz and infrared radiation to the visible, ultraviolet, and x-ray spectral regions.

The first FEL employed an optical cavity and operated as an oscillator in the infrared wavelengths (Deacon *et al.*, 1977). It was soon recognized that, with sufficient gain, the FEL could operate as an amplifier in the so-called self-amplified spontaneous emission (SASE) mode, where the initial random field of spontaneous radiation is amplified exponentially until a single mode dominates (Kondratenko and Saldin, 1980; Bonifacio, Pellegrini, and Narducci, 1984; Murphy and Pellegrini, 1985; Kim, 1986; Wang and Yu, 1986). SASE operation does not require an optical cavity and thus is very attractive for an x-ray FEL, since creating such a cavity is challenging.

Achieving the high FEL gain needed for SASE operation required a close match between the phase space occupied by the electron beam and that of the radiation mode that is being pumped. At x-ray wavelengths, matching these phase space volumes requires a very high-brightness electron beam.

Tremendous progress in the production and control of high-energy electron beams during the 1980s and 1990s was critical to the realization of an x-ray FEL. A detailed history of this development is recounted in a recent paper (Pellegrini, 2012). Among the enabling technologies, the invention of the photocathode radio frequency (rf) gun in the 1980s opened up the possibility of generating extremely short and bright electron bunches (Fraser, Sheeld, and Gray, 1986; Carlsten, 1989). In addition, operation of the SLAC Linear Collider (Seeman, 1991) advanced the precise control of electron beams, and the development of synchrotron undulator x-ray sources advanced precision magnetic array construction (Halbach, 1985). Based on these advances in technology and theoretical understanding of SASE FELs, Claudio Pellegrini proposed in 1992 that it would be feasible to create a SASE FEL operating in the 1–40 Å wavelength range based on the SLAC linear accelerator (Pellegrini, 1992).

Detailed design studies and development activities followed the initial concept (Winick *et al.*, 1993), finally resulting in a proposal to build a large FEL facility based on the SLAC linac (Arthur *et al.*, 2002). Although at first there was some skepticism about whether the tolerances for an x-ray FEL could actually be met and whether its scientific utility would justify its large cost, eventually the idea gained credibility (Birgeneau and Shen, 1997; Leone, 1999). Meanwhile, test facilities operating in the infrared and visible spectral regions proved the SASE concept viable (Hogan *et al.*, 1998; Milton *et al.*, 2001; Tremaine *et al.*, 2002).

In the mid-1990s, scientists at the Deutsches Elektronen-Synchrotron (DESY) in Hamburg, Germany recognized an opportunity to build a free-electron laser operating in the far ultraviolet (UV) region, subsequently named FLASH (Free electron Laser in Hamburg) (Ackermann *et al.*, 2007). It would be built in conjunction with a superconducting linac test facility that was being constructed for the electron-positron linear collider project (TESLA) (Ayvazyan *et al.*, 2002). FLASH was commissioned starting in 1999. All the data obtained in these pioneering high-gain experiments agreed well with the theoretical predictions on exponential growth, intensity fluctuations, saturation, and dependence on electron beam parameters. They also provided strong support for the feasibility of an x-ray FEL and important experience for the design and construction of short-wavelength FELs.

By the mid-2000s, LCLS was under construction with anticipated first light in 2009. Also under construction by the end of the decade was the SACLA x-ray FEL at the RIKEN SPring-8 Center in Japan with anticipated first light in 2011 (Ishikawa *et al.*, 2012) and the European XFEL, with anticipated first light in 2017 (Altarelli *et al.*, 2006). These high-gain x-ray FELs, when operated in the SASE mode, can generate multi-gigawatt and femtosecond-duration coherent x-ray pulses. The science community recognized that the extremely high peak power and excellent transverse coherence of these sources could provide about 9 to 10 orders of magnitude higher peak brightness than offered by existing synchrotron radiation sources based on electron storage rings, making FELs probes for both the ultrasmall (nm) and the ultrafast (fs) worlds. The goal was to operate all of these FELs as user facilities where x-ray beams are provided to the community to allow a wide range of experimental studies to take place.

B. X-ray FELs as user facilities

For x-ray FELs to succeed, accelerator and undulator technology had to be developed as described in the previous section. The FEL also had to deliver stable beams in a variety of configurations to users who would write peer-reviewed proposals to access the beams. Stability, reproducibility, and reliability of operations would be critical. The transition from accelerator research to developing a new technology such as a SASE FEL to running a user facility that delivers stable beams is a difficult one. This transition was anticipated to be particularly challenging for the x-ray community, which was accustomed to the stable, user-friendly conditions developed over several decades at synchrotron sources.

For LCLS and the new generation of x-ray FELs this transition was greatly aided by pioneering work at the FLASH facility at DESY, the first short-wavelength FEL user facility. FLASH started user operations in 2005, initially delivering x rays at wavelengths of 13 to 47 nm to five beam lines (Tiedtke *et al.*, 2009). As each shot of the fluctuating SASE source is unique, the machine parameters must be synchronized to the user experiment. FLASH spearheaded the development of novel diagnostics and data acquisition concepts needed for this new type of source (Tiedtke *et al.*, 2009).

FLASH immediately attracted the attention of the international science community, and within the first few years ground-breaking experiments in a wide range of disciplines were performed (Bostedt *et al.*, 2009). Many techniques were developed to exploit the features of the FEL source. Notable examples include the first demonstration of single-shot coherent diffractive imaging (Chapman *et al.*, 2006, 2007), the investigation of fundamental interaction of intense short-wavelength pulses with atoms (Moshammer *et al.*, 2007; Sorokin *et al.*, 2007), clusters (Bostedt *et al.*, 2008), plasmas (Nagler *et al.*, 2009), and time-resolved photoemission studies in materials science (Pietzsch *et al.*, 2008).

FLASH has been continuously upgraded, and it is now delivering extreme ultraviolet (XUV) and soft x-ray pulses well into the water window (2.3–4.4 nm). Photon energies presently reach up to 300 eV (4.2 nm), with pulse energies up to a few hundred μJ. Currently the FLASH facility is being extended to FLASH-II, which will use the existing accelerator to feed a new variable-gap undulator.

In Japan, Riken constructed the SPring-8 Compact SASE Source test accelerator (SCSS) as a prototype x-ray FEL machine in 2005 (Shintake *et al.*, 2001, 2008). First lasing was observed at 49 nm with an electron beam energy of 250 MeV and SCSS started user operations in 2008 (Yabashi *et al.*, 2013). SCSS was decommissioned in 2013 and is now part of the upgrade plan of SACLA (Yabashi, Tanaka, and Ishikawa, 2015).

C. LCLS science case

Before LCLS began operation, speculation about its scientific uses was hampered by the fact that its expected

characteristics lay far beyond what was then available. Nevertheless, many workshops were held to discuss the potential applications of a hard x-ray FEL. LCLS would be the world's first hard x-ray laser and offered the potential to characterize matter on both the atomic length and time scales using scattering and spectroscopic techniques in a regime previously inaccessible by either longer wavelength FELs or storage ring-based x-ray sources with considerably lower peak brightness and coherent flux. The consensus that developed was captured in the "LCLS First Experiments" report (Shenoy and Stohr, 2003). This document identified five scientific fields in which it was believed LCLS would have a strong impact. The initial experimental stations were optimized for science in these areas.

Atomic, molecular, and optical physics: LCLS would expose atoms to photon field conditions never before created in a laboratory. This would present opportunities to advance measurements, experimental techniques, and theories in the area of fundamental atomic physics. Experiments were suggested that would directly observe multiple core-hole formation in an atom, extend nonlinear optics into the x-ray regime, produce and characterize energetic clusters with high-charge states, and produce lasing from LCLS-excited matter.

Nanoscale dynamics: Coherent x-ray scattering techniques, such as x-ray photon correlation spectroscopy, were envisioned for use at LCLS to elucidate the dynamics of intermolecular interactions over micron to angstrom characteristic length scales. In addition, new split-pulse techniques were foreseen that could access ultrafast dynamics spanning femtoseconds to nanoseconds. Such measurements are inaccessible at synchrotron x-ray sources due to the limited available coherent flux and temporal resolution. These advances were expected to reveal the dynamics of entangled polymers, the structural basis of glassy dynamics, and the collective mode dynamics in liquids and glasses.

Matter in extreme conditions: LCLS was viewed as having the potential to profoundly impact both the creation and characterization of matter in extreme conditions of temperature and density. It was anticipated that focusing LCLS on a solid-state target could generate plasmas at solid densities and temperatures that would reach the warm dense matter (WDM) regime, where correlated effects would emerge due to the strong coupling between electrons and atoms and ions. Used in combination with very high-energy and high-peak-power optical-laser systems, LCLS could offer additional capabilities for warm dense matter research, laser probing of near-solid-density plasmas, and laser-plasma spectroscopy of ions in plasmas.

Chemistry: It was anticipated that the femtosecond-duration, angstrom-wavelength pulses of LCLS could provide the necessary temporal and spatial resolution to observe molecular motion during the initial stages of fast chemical reactions. The ability to directly follow the evolution of bond lengths and angles could have a profound impact on the field of femtochemistry. LCLS experiments were expected to advance fundamental understanding of photochemically induced bond breakage in both gas and solution phase systems, photosynthetic processes, the melting of the long-range order of crystalline samples under extreme levels of photoexcitation, and dynamical processes in nanoparticles.

Structural biology: The x-ray pulse parameters of LCLS offered the potential to image important biological structures at atomic resolution without the need for crystallization. Detailed calculations were performed to understand the intensity and time scale limits above which damage-induced changes in the sample would occur and compromise diffraction data (Neutze *et al.*, 2000). With femtosecond pulses, the allowable intensity limit exceeds the limit for conventional x-ray methods by several orders of magnitude. As a result, LCLS was expected to image important biological structures that could not be solved by other means. It would allow the use of focused x-ray beams on very small samples, including systems difficult to crystallize, such as membrane proteins and nonreproducible structures such as cells and viruses.

Advances in FEL physics at longer wavelength sources, along with decades of advances at synchrotrons, enabled the successful turn-on and early operation of LCLS. However, FEL physics is still very young. The capabilities of LCLS have expanded since turn-on and the field is continuing to advance. And while not all of the early scientific goals of LCLS have been realized, significant progress has been made in all areas and is described in this review.

II. THE LCLS X-RAY FEL SOURCE

A. X-ray FEL physics and LCLS performance

In a free-electron laser, a small fraction of the kinetic energy of a relativistic electron beam is pumped into an intense beam of electromagnetic radiation by the resonant interaction between the electron bunch and the radiation in an undulator. In this section, a summary of basic FEL physics is presented to support discussions of the science that can be accessed with an x-ray FEL such as LCLS. More detailed reviews that focus specifically on the physics and technology of the FEL can be found in Murphy and Pellegrini (1990), Saldin, Schneidmiller, and Yurkov (2000), Huang and Kim (2007), and Schmüser *et al.* (2014).

A review of the physics of x-ray free-electron lasers is published concurrently in this edition of the Review of Modern Physics (Pellegrini, Marinelli, and Reiche, 2016) and includes a much more detailed discussion of the accelerator physics involved in making a machine like LCLS work. In this article and this section, the physics of free-electron lasers is briefly reviewed for the general reader.

1. SASE FEL basics of operation

Consider a planar magnetic undulator with a sinusoidal vertical magnetic field as shown in Fig. 1(a). The peak field strength is B_0, and the undulator period is λ_u. An electron beam with the energy γmc^2 executes a nearly sinusoidal trajectory in the undulator and emits fundamental undulator radiation at the wavelength

$$\lambda_r = \frac{\lambda_u}{2\gamma^2}\left(1+\frac{K^2}{2}\right) = \frac{2\pi c}{\omega_r}, \tag{1}$$

where $K = eB_0\lambda_u/(2\pi mc)$ is the undulator strength parameter, e is the charge of the electron, c is the speed of light in

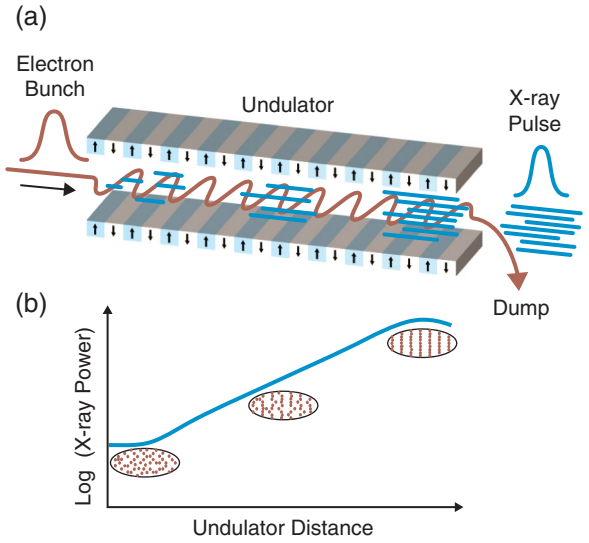

FIG. 1. Schematic of a high-gain self-amplified spontaneous emission (SASE) free-electron laser, in which both the radiation power and the electron beam microbunching grow as a function of the undulator distance until saturation.

vacuum, m is the electron mass, and ω_r is the fundamental undulator frequency. Higher harmonic radiation, especially odd harmonics, also exists with reduced intensity.

For a sufficiently bright electron beam and a sufficiently long undulator, the resonant interaction leads to an exponential growth of the fundamental radiation intensity along the undulator distance as illustrated in Fig. 1(b). Such a high-gain FEL does not require an optical cavity or external seed and can amplify the initial spontaneous undulator radiation in the SASE process. Microbunching is essential. The resonant beam-radiation interaction first induces energy modulation in the electron bunch with the periodicity λ_r from an initially monoenergetic electron beam. Since electrons losing energy to the radiation travel on a sinusoidal trajectory of larger amplitude than electrons gaining energy from the radiation, the higher-energy electrons catch up to the lower-energy electrons, leading to the formation of microbunches. The electrons within a microbunch radiate like a single particle of high charge and contribute to the radiation growth. The growing radiation field enhances the microbunching further and leads to an exponential growth and eventual saturation of the radiation power. The radiation is linearly polarized in the horizontal direction, perpendicular to both the magnetic field and the electron beam trajectory.

The scaling behavior of a high-gain FEL amplifier in the one-dimensional (1D) limit can be well characterized by the so-called FEL Pierce parameter (Bonifacio, Pellegrini, and Narducci, 1984)

$$\rho = \left[\frac{1}{64\pi^2}\frac{I_p}{I_A}\frac{K^2[JJ]^2\lambda_u^2}{\gamma^3\sigma_x^2}\right]^{1/3}, \tag{2}$$

where the Bessel function factor $[JJ]$ is equal to $[J_0(\xi) - J_1(\xi)]$ with $\xi = K^2/(4+2K^2)$ for a planar undulator, I_p is the electron peak current, $I_A \approx 17$ kA is the Alfvén current, and σ_x is the rms transverse size of the electron beam. The power grows exponentially with undulator distance z: $P[z] \propto \exp(z/L_G)$ with the power gain length

$$L_G \approx \frac{\lambda_u}{4\pi\sqrt{3}\rho}. \tag{3}$$

At FEL saturation the peak power is given by

$$P_{\text{sat}} \approx \frac{\rho\gamma mc^2 I_p}{e}. \tag{4}$$

Here ρ characterizes the efficiency of the FEL in terms of the electron beam power. For x-ray FELs, ρ is typically on the order of 10^{-3}.

The SASE FEL has excellent transverse coherence, as the high-gain process selects a dominant fundamental mode. However, due to the finite bandwidth of SASE and shot noise start-up, SASE FEL radiation has limited temporal coherence and exhibits shot-to-shot fluctuations in intensity. The normalized rms bandwidth and coherence length of SASE radiation at saturation are (Kim, 1986; Wang and Yu, 1986)

$$\frac{\sigma_\omega}{\omega_r} \approx \rho, \tag{5}$$

$$L_{\text{coh}} \approx \frac{\sqrt{\pi}c}{\sigma_\omega} = \frac{\lambda_r}{2\sqrt{\pi}\rho}. \tag{6}$$

For a "flat-top" electron bunch of length $L_b > L_{\text{coh}}$, the average number of temporal spikes of SASE is $M = L_b/L_{\text{coh}}$. For typical parameters of operation of LCLS, the output of roughly 1000 microbunches results in a 0.3 to 3 fs coherent spike. A typical FEL pulse of 10^{12} to 10^{13} photons will be made of a few tens to hundreds of coherent spikes with no fixed phase relation to each other. In the exponential-gain regime, the relative rms fluctuation of the SASE intensity is proportional to $1/\sqrt{M}$ since these spikes are independent radiation sources.

We now conclude this section with a qualitative discussion of the radiation brightness, which is defined as the number of photons per second in 0.1% bandwidth over the transverse phase space areas. Compared to incoherent synchrotron radiation sources, the exponential amplification of coherent radiation in x-ray FELs increases the number of photons by about a factor of a million. The x-ray FEL pulse duration also decreases from tens of picoseconds to tens of femtoseconds with excellent transverse coherence. All together, the x-ray FELs provide 9 to 10 orders of magnitude higher peak brightness than offered by existing synchrotron radiation facilities.

2. Accelerator physics challenges of an x-ray FEL

Extremely bright electron beams and very high-quality undulator arrays are required to drive x-ray FELs. A high-energy linear accelerator, or linac, with an appropriate injector and electron transport optics can deliver electron beam brightness at requisite levels for successful x-ray FEL operations. While other options are possible, an electron beam from a linac source is typically more than 1000 times brighter

than those from standard storage rings, and so was a natural choice for initial x-ray FEL studies. Once such a high-brightness beam is created in a linac, it must be compressed to achieve a high peak current and then accelerated to the undulator entrance with a small transverse cross section.

a. High-brightness electron beams

Both higher peak currents and smaller transverse cross sections increase the FEL Pierce parameter and reduce the 1D gain length [cf. Eqs. (2) and (3)], while the electron beam energy spread and angular spread, due to finite emittance, increase the overall gain length from the 1D limit. The FEL design optimization is therefore multidimensional and is well beyond our scope here, but the typical requirements on electron beams are

$$I_p \geq 1 \text{ kA}, \qquad \frac{\sigma_\gamma}{\gamma} \leq \rho/2, \qquad \frac{\varepsilon_N}{\gamma} \sim \frac{\lambda_r}{4\pi}, \tag{7}$$

where ε_N is the normalized emittance in the transverse directions. Note that these requirements apply to the time-sliced beam qualities defined on the scale of the coherence length [cf. Eq. (6)], instead of beam qualities projected over the entire bunch length. This adds additional challenges to the electron bunch diagnostics.

The electron injector is typically based on an rf photocathode gun (Fraser, Sheeld, and Gray, 1986), which rapidly accelerates the photoelectrons from the cathode in order to minimize the effects of space charge forces on beam brightness. A solenoid magnet positioned immediately after the cathode focuses the beam into the next accelerating section and accomplishes a compensation of the space charge-induced correlated emittance growth (Carlsten, 1989). The challenge is to extract up to 1 nC of bunch charge in a few-picosecond pulse length with the transverse normalized emittance $\varepsilon_N \leq 1$ μm. Based on the experience gained from the prototype gun (Batchelor *et al.*, 1992; Palmer *et al.*, 1997), this challenge was clearly met by the LCLS photocathode rf gun with extensive rf design and engineering (Akre *et al.*, 2008). An alternative high-voltage pulsed electron gun, developed for the low-emittance injector system of the SACLA FEL (Togawa *et al.*, 2007), is based on single-crystal CeB_6 cathode.

The linac accelerates and compresses the electron bunch while preserving beam brightness. Acceleration reduces the relative energy spread and angular spread, while compression increases the peak current by shortening the bunch length, fulfilling Eq. (7). Figure 2 shows the LCLS accelerator layout from the electron gun to the main dump, with two bunch compressors and a 132-m-long undulator. Bunch compression is typically accomplished by accelerating at an off-crest rf phase, providing a nearly linear energy correlation, or chirp, along the bunch length. A series of dipole magnets, usually a simple four-dipole chicane, generates an energy-dependent path length so that the chirped bunch compresses in length. For more information, a comprehensive review of electron beam dynamics in a linear accelerator for x-ray FELs has recently been published (DiMitri and Cornacchia, 2014).

One of the most challenging issues associated with magnetic bunch compression is the effect of coherent synchrotron radiation (CSR) in the bends (Saldin, Schneidmiller, and Yurkov, 1997). The coherent radiation originating from the very short electron bunch can interact with the bunch, leading to increased energy spread and emittance. The bunch compressors must be designed to minimize CSR effects. These effects have been measured in both LCLS compressors and show reasonably good agreement with available computer modeling codes (Bane *et al.*, 2009).

Another important collective effect associated with bunch compression is the microbunching instability. A small density or energy modulation of an electron beam with small energy spread can be strongly amplified by CSR and longitudinal space charge fields of the bunch, degrading the bunch longitudinal phase space before the FEL interaction in the undulator (Borland *et al.*, 2002; Huang *et al.*, 2004; Saldin, Schneidmiller, and Yurkov, 2004). A special laser heater located at the end of the injector can be used to add a small level of slice energy spread (~10 to 20 keV) before the bunch compressors to "Landau damp" the instability (Huang *et al.*, 2004; Saldin, Schneidmiller, and Yurkov, 2004). Such a laser heater device is implemented at LCLS (cf. Fig. 2) and has been shown to improve the FEL gain length and saturation power (Huang *et al.*, 2010).

b. FEL undulators

To accommodate SASE saturation at angstrom wavelengths, which is required for power stability, the SASE FEL undulator is typically on the order of 100 m long. The undulator beam line needs focusing to keep the beam size small and nearly constant. Quadrupole magnets are typically inserted between undulator sections for this purpose, along with beam position monitors and correctors to measure and control the beam trajectory.

Among the various design considerations and tolerances on FEL undulators, two very stringent requirements are

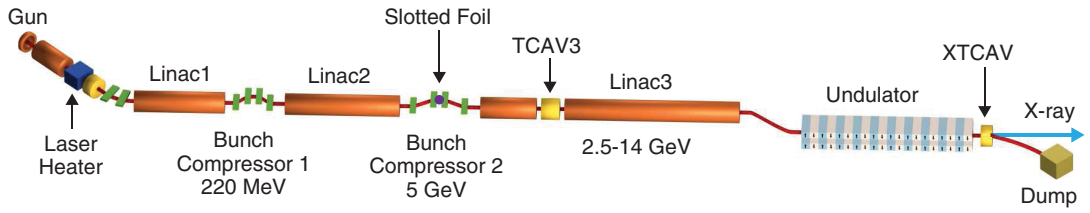

FIG. 2. Linac Coherent Light Source accelerator layout from the electron gun to the beam dump, including a laser heater, two bunch compressors, three linac sections, and a 132-m-long undulator. Also included are the slotted foil in the middle of bunch compressor 2 for x-ray pulse length control and two transverse deflecting cavities (TCAV3 and XTCAV) for pulse length measurements.

necessary to ensure lasing at angstrom wavelengths. The first requirement is that the magnetic field quality of each undulator section, quantified by the strength parameter K, must be very uniform over the entire beam line to maintain the resonant interaction. The rms relative variation in K from segment to segment should be much less than the FEL parameter ρ, and hence should be at or below 1×10^{-4}. This requirement is met with state-of-the-art permanent magnet undulators.

The second challenging requirement is that the trajectory along the 100 m undulator should be absolutely straight at the level of 5 μm rms over an FEL gain length (typically 4–5 m). The tolerances for electron beam straightness can be met through a beam-based alignment method (Emma, Carr, and Nuhn, 1999), which is implemented using large electron energy variations and submicron-resolution cavity beam position monitors, with precise conventional alignment used to set the starting conditions (Nuhn, 2009; Loos *et al.*, 2010).

3. LCLS first lasing and performance

The principal LCLS performance goals were to produce x-ray pulses of 200 fs duration or shorter, photon energies ranging from 0.8 to 8 keV, and 10^{12} photons per pulse at 8 keV.

LCLS construction, funded by the United States Department of Energy (DOE), started in 2005 after several years of preliminary design and engineering. The SLAC linac, originally built starting in 1962, was modified to achieve the necessary low-emittance, high-brightness electron beam for FEL operation. The electron gun and accelerator commissioning started in 2007 and progressed for two years. Undulator commissioning started in April 2009 and all of the principal design goals were achieved or exceeded promptly at the outset of the FEL commissioning in April–May 2009. Decades of SLAC accelerator experience and expertise were a major contributing factor to the rapid success of the LCLS turn-on.

FEL lasing was observed immediately after just 12 (of 33) undulator segments were inserted, and within four days the SASE FEL was fully saturated at the shortest design wavelength of 1.5 Å (8 keV), well before the full undulator length (Emma *et al.*, 2010). The FEL power as a function of the undulator length at first lasing is shown in Fig. 3. The relative FEL power was measured for each shot by integrating the intensity measured on an intercepting yttrium aluminum garnet (YAG) screen (cf. Fig. 3 inset) located 50 m downstream of the last undulator segment. A 3.3 m gain length was obtained through a linear fit to the logarithm of the relative power measurements (30 beam shot averages at each data point) as a function of the location of the last inserted undulator segment. The FEL power values were estimated by scaling to the simulation results from the computer code GENESIS (Reiche, 1999) and were in reasonable agreement with independent measurements (10–20 GW at saturation in this early case).

The absolute FEL pulse energy was estimated by measuring the electron energy loss across the undulator due to the lasing process. This measurement, the average energy loss per electron multiplied by the electron bunch charge, yielded a

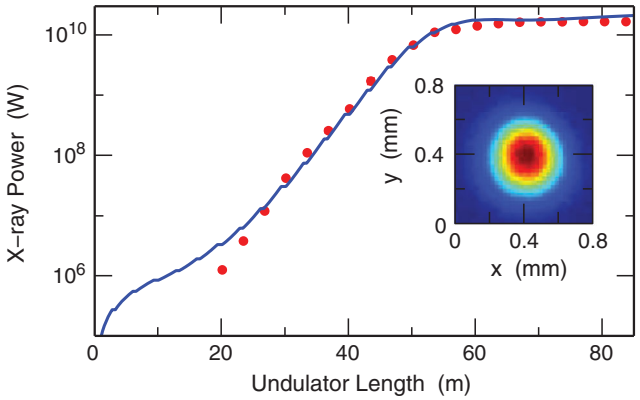

FIG. 3. Linac Coherent Light Source free-electron laser power (red points) at 1.5 Å vs active undulator length. The measured gain length is 3.3 m and a GENESIS simulation is overlaid in blue with electron beam parameters measured. The x-ray image on the yttrium aluminum garnet screen is shown in the inset. Adapted from Emma *et al.*, 2010.

1 mJ pulse energy with $< 5\%$ rms precision for the nominal 250 pC bunch charge throughout the entire wavelength range.

In October 2009, five months after first lasing, LCLS began its first round of x-ray experiments. The facility rapidly attained and surpassed its design goals in terms of spectral tuning range, energy per pulse, and pulse duration. A summary of the typical LCLS x-ray beam characteristics is shown in Table I.

B. LCLS developments and improvements over five years

Despite the early success of first lasing and subsequent operation, it is widely recognized that such a source continues to have significant potential for improvement. The constant interaction between x-ray experimenters and FEL physicists has driven the development of new modes of FEL operation and improved capability. The major directions for improvements are the following: ultrashort x-ray pulse generation and characterization, seeding to enhance temporal coherence, and control of radiation spectra such as wide bandwidth and

TABLE I. Design and typical measured LCLS x-ray beam characteristics for soft x-ray (SXR) and hard x-ray (HXR) photon energies.

Parameter	Design	Typical	Unit
Photon energy range	800–8000	270–11 200	eV
Peak x-ray power	10	Up to 100	GW
X-ray pulse energy	2	2–4	mJ
Pulse repetition rate	120	120	Hz
SXR[a] bandwidth (FWHM)	0.1	0.2–2	%
SXR pulse duration (FWHM)	200	50–500	fs
SXR pulse energy jitter (rms)	20	3–10	%
SXR wavelength jitter (rms)	0.2	0.15	%
HXR[b] bandwidth (FWHM)	0.1	0.2–0.5	%
HXR pulse duration (FWHM)	200	30–100	fs
HXR pulse energy jitter (rms)	20	5–12	%
HXR wavelength jitter (rms)	0.2	0.05	%

[a]Typical soft x-ray photon energy is 830 eV.
[b]Typical hard x-ray photon energy is 8.3 keV.

two-color operations. The latest capability enhancement at LCLS is to control the radiation polarization through a purposely built undulator (Nuhn *et al.*, 2015).

1. Ultrashort x-ray pulse generation

One of the significant attributes of x-ray FEL sources is the availability of femtosecond x-ray pulses for ultrafast science. Owing to the exceptional electron beam quality and feedback control, the electron bunch length can easily be varied during FEL operation. To accommodate user requests, LCLS has developed two operating modes to deliver pulses with durations in the few-fs range: a low-charge operating mode (Ding *et al.*, 2009) and a slotted-foil method (Emma *et al.*, 2004). Both ultrashort pulse modes are delivered in routine operations and applied in various atomic, molecular, and optical physics experiments (cf. Secs. IV.A.1 and IV.A.3).

In the low-charge mode (20 pC), the reduced bunch charge provides improved transverse emittance from the gun compared to nominal operation and also mitigates collective effects in the accelerator, allowing for extreme bunch compression. The compressed electron bunch length is estimated to be <5 fs FWHM. Stable saturated FEL operations with estimated power levels similar to the nominal charge (150–250 pC) are routinely achieved over the entire LCLS wavelength range. The total x-ray pulse energy is lower in the short pulse modes compared to the nominal case by almost an order of magnitude, approximately in proportion to the pulse duration. In this low-charge mode, the FEL pulse consists of only one or two coherent spikes of radiation in the soft x-ray regime and has better temporal coherence (cf. Fig. 5).

Another method for femtosecond pulse generation is to use an emittance-spoiling slotted foil, which was first proposed in 2004 and has been used at LCLS since 2010. When the dispersed electron beam passes through a foil with single or double slots, most of the beam emittance is spoiled, leaving very short unspoiled time slices to produce femtosecond x rays. To achieve a variable pulse duration and separation, an aluminum foil (3 μm thickness) with different slot arrays was implemented. Depending on the bunch charge and the final current, a single slot with variable slot width can control the soft x-ray duration from 50 down to 6 fs, while V-shaped double slots with different slot separation can provide two short soft x-ray pulses separated by about 10 to 80 fs for pump-probe experiments (Schorb *et al.*, 2012b).

2. Self-seeding

As described in Sec. II.A.1, typical LCLS pulses are made of a few tens to hundreds of coherent spikes of fs duration, each with no fixed phase relation to the others due to the SASE process. Longitudinal coherence can be imposed by a post-SASE monochromator, but typically with reduced intensity and increased intensity fluctuations. However, seeding the FEL process with a highly longitudinally coherent source could, in principle, create Fourier transform limited pulses of enhanced intensity compared to the post-SASE monochromator. External seeding at radiation wavelengths down to a few nanometers was demonstrated at the FERMI FEL at Synchrotron Trieste with high-gain harmonics generation from an external UV laser (Yu, 1991; Allaria *et al.*, 2012, 2013). More efficient frequency up-conversion schemes such as echo-enabled harmonic generation are under active development (Stupakov, 2009; Xiang *et al.*, 2010; Zhao *et al.*, 2012). Nevertheless, at shorter radiation wavelengths around 1 nm or below, external laser seeding becomes increasingly difficult.

However, it was pointed out that self-seeding could be a viable alternative (Feldhaus *et al.*, 1997), accomplished using two undulators with an x-ray monochromator between them. The first undulator operates in the exponential-gain regime of a SASE FEL. After exiting the first undulator, the electron beam is guided through a dispersive bypass, namely, a four-dipole chicane, that smears out the microbunching induced in the first undulator. The SASE output from the first undulator enters the monochromator, which selects a narrow band of radiation as the seed. At the entrance of the second undulator the monochromatic x-ray seed is combined with the electron beam from the chicane and amplified to saturation.

Following a proposal from DESY (Geloni, Kocharyan, and Saldin, 2011), a collaboration between SLAC, Argonne National Laboratory, and the Technical Institute for Superhard and Novel Carbon Materials in Russia successfully implemented hard x-ray self-seeding at LCLS in 2012. As shown in Fig. 4, one undulator section (U16) was removed in order to install a chicane and an in-line single diamond crystal. The thin crystal transmits most of the SASE pulse but also generates a trailing monochromatic seed pulse. The chicane can delay the electron bunch to temporally overlap with the seed and to amplify the seed in the second part of the

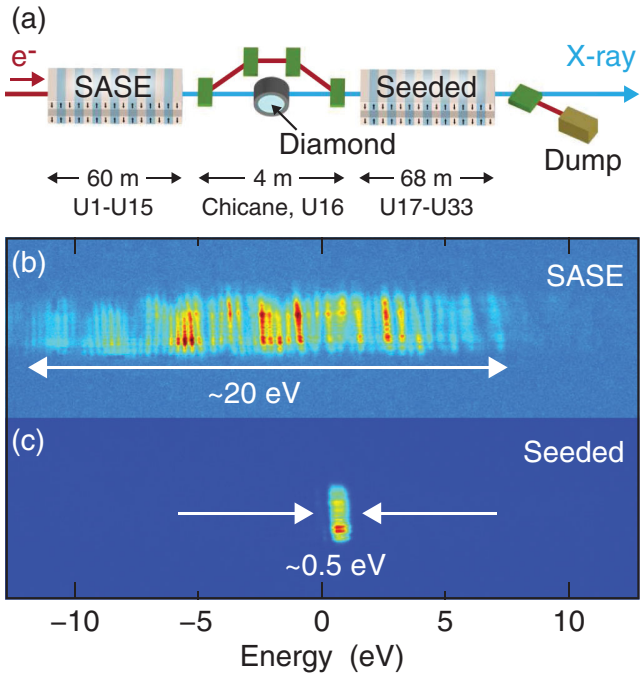

FIG. 4. Overview of hard x-ray self-seeding operation at the Linac Coherent Light Source (LCLS). (a) The LCLS hard x-ray self-seeding setup at 1.5 Å (seeding diamond is not drawn to scale). (b) The self-amplified spontaneous emission (SASE) and (c) seeded spectra recorded on single shots. The seeded bandwidth (0.5 eV FWHM) is about a factor of 40 narrower than the SASE bandwidth (20 eV FWHM).

undulator array (U17-U33). Self-seeding at the angstrom-wavelength scale, with a factor of about 40 bandwidth reduction, was demonstrated as illustrated by the data shown in Fig. 4 (Amann *et al.*, 2012). Currently, hard x-ray self-seeding provides beams from 5.5 to 9.5 keV with 2 to 4 times more photons per pulse than SASE using a postmonochromator. A representative application of this capability has been published (Fletcher *et al.*, 2013).

After the success of hard x-ray self-seeding, a compact soft x-ray self-seeding system was designed and implemented upstream of the hard x-ray self-seeding section in 2013 (Feng *et al.*, 2012; Cocco *et al.*, 2013). This system covers the photon energy range from 0.5 to 1 keV with a bandwidth of 2×10^{-4}. Although still being optimized, the soft x-ray self-seeding system has demonstrated a bandwidth of $(2-5) \times 10^{-4}$, wavelength stability of 1×10^{-4}, and an increase in peak brightness by a factor of 2–5 across the photon energy range. By avoiding the need for a monochromator at the experimental station, the soft x-ray self-seeded beam can deliver as much as 50-fold higher brightness to users (Ratner *et al.*, 2015).

3. Wide bandwidth mode

Wide bandwidth FEL pulses can be produced by electron bunches with relatively large energy spread if the energy deviation is correlated with its longitudinal coordinate. In this case, the energy spread over an FEL slice, defined by the coherence length in Eq. (6), can still be much smaller than the FEL parameter ρ since the coherence length is typically a small fraction of the bunch length. The output SASE pulse will be frequency chirped and will possess a relatively wide bandwidth. Such a wide bandwidth pulse can be useful for crystallography applications in order to index a large number of Bragg peaks within a single pulse for crystal orientation determination.

At LCLS, since the electron bunch is so short after the second bunch compressor (BC2 in Fig. 2) in comparison with the rf wavelength, accelerating the bunch off the crest of the rf phase will generate negligible energy spread or chirp. A more effective way to generate energy spread is to use the linac wakefield. In normal operating conditions the energy spread generated by the wakefield cancels, in large part, the electron energy spread created prior to BC2, which is necessary for bunch compression. This leads to a very small projected final energy spread that does not dilute the SASE bandwidth. However, if BC2 is operated in overcompression, where the head and tail of the bunch switch their relative longitudinal positions, the energy spread generated by the linac wakefield adds to the initial energy spread, leading to a relatively large projected energy spread of the electron beam (0.5%–1% level). Part, or even all, of the electron bunch will contribute to lasing and will generate an FEL with a bandwidth on the order of 1%–2% (Welch *et al.*, 2011; Turner *et al.*, 2014), depending on the machine tuning and photon energies (cf. Table I).

4. Two-color FEL

Two-color pulses are another example of custom-made x rays from an FEL, where two pulses of different photon energy are generated with a variable time delay.

According to the undulator resonant condition [Eq. (1)], the FEL radiation wavelength is determined by the undulator parameter K and the electron Lorentz factor γ for a fixed-period undulator. Thus, the two-color methods developed so far in the x-ray region fall into two classes. One class relies on generating two x-ray colors by using two distinct values of K with a quasimonoenergetic electron beam (Hara *et al.*, 2013; Lutman *et al.*, 2013; Marinelli *et al.*, 2013). In this case, the LCLS undulator beam line is divided into two sections longitudinally with a distinct K associated with each section. The electron bunch generates one color at each section, and a delay chicane can be used between the sections to control the time delay between two colors. While this "split undulator" approach can achieve full control of the time and energy separation, the intensity of both pulses is compromised because the same electron beam is used for lasing twice, yielding a total power typically between 5% and 15% of the full saturation power. The time delay depends on the strength of the chicane and can be up to 1 ps.

The second method generates two colors simultaneously in one undulator using two electron bunches of different energies (Marinelli *et al.*, 2015). This method requires generation, acceleration, and compression of double electron bunches within the rf wavelength of the accelerator system. Each x-ray pulse is generated by one electron bunch and can reach the full saturation power, improving the two-color intensity by 1 order of magnitude in comparison with the first method. This "twin-bunch" approach can also be combined with hard x-ray self-seeding using appropriate crystal orientations to generated two-seeded hard x-ray colors (Lutman *et al.*, 2014). The time delay between pulses can be adjusted from nearly overlapping to ~100 fs (Marinelli *et al.*, 2015).

5. X-ray pulse length characterization

The first experiment performed at LCLS postulated that the x-ray pulse length was shorter than the electron bunch length (Young *et al.*, 2010). Subsequent experiments aimed at studying the average pulse length with laser-assisted Auger decay (Düsterer *et al.*, 2011) or x-ray–optical cross-correlation techniques (Schorb *et al.*, 2012a) confirmed that on average the x-ray pulse length was ~70% of the electron bunch length. Measuring the x-ray pulse length on a shot-by-shot basis with femtosecond precision is challenging. A promising route to realizing single-pulse x-ray temporal information is photoelectron streaking (Grguras *et al.*, 2012), which has yielded temporal x-ray pulse information down to a few femtoseconds (Helml *et al.*, 2014); see Sec. IV.A.3.

An alternative approach to directly measuring the x-ray pulse length is to determine it from the characteristics of the electron bunch. The absolute electron bunch duration after the second bunch compressor can be obtained with a transverse deflecting cavity (TCAV) operating at 2.856 GHz (TCAV3 in Fig. 2). The rf fields of the transverse cavities are perpendicular to the beam direction and can impart a horizontal or vertical time-dependent kick to the bunch. The amount of deflection is a function of the phase between the cavity and the bunch. If the bunch travels through the structure at one of the zero crossings of the field the centroid of the bunch experiences a zero kick, but the head and tail are

deflected to opposing directions. This effectively maps the time coordinate to a transverse position that is measured with a beam profile screen.

While sufficient in resolution (∼10 fs rms) for normal bunch charge operation (150–270 pC), TCAV3 cannot resolve the ultrashort, submicron bunches generated in low-charge mode at 20–40 pC. This diagnostic is also destructive to the beam. An XTCAV operating at 11.4 GHz can achieve a much higher resolution from the increased frequency and the higher deflecting voltage (Dolgashev and Wang, 2012). Two such 1-m-long structures with a total deflecting voltage of 48 MV are installed downstream of the undulators and provide ∼10 times higher resolution than TCAV3 (Krejcik *et al.*, 2012). In combination with the magnetic bends in the main electron dump downstream of the XTCAV, it is possible to observe the full longitudinal phase space with the energy measured in the vertical direction and the temporal distribution in the horizontal direction.

The XTCAV measurement of the longitudinal phase space provides a time-resolved measure of the electron energy distribution along the bunch and can be used to compare the time-resolved energy with and without FEL interactions. The energy loss distribution along the bunch can then be used to reconstruct the x-ray temporal profile (Ding *et al.*, 2011). Such measurements have achieved a resolution of less than 1 fs rms in the soft x-ray regime (∼1 keV) and ∼4 fs rms in the hard x-ray regime (∼10 keV) (Behrens *et al.*, 2014). Example measurements of the longitudinal phase space for 20 pC bunch charge with the FEL off and on are shown in Figs. 5(a) and 5(b), respectively, while the reconstructed 1 keV x-ray pulse profile with 2.6 fs FWHM duration is shown in Fig. 5(c). This measurement is nondestructive to the FEL x-ray beam, as the XTCAV is located after the undulators where the electron beam is being discarded. The reconstructed x-ray pulse profiles are made available to the experimental data acquisition system.

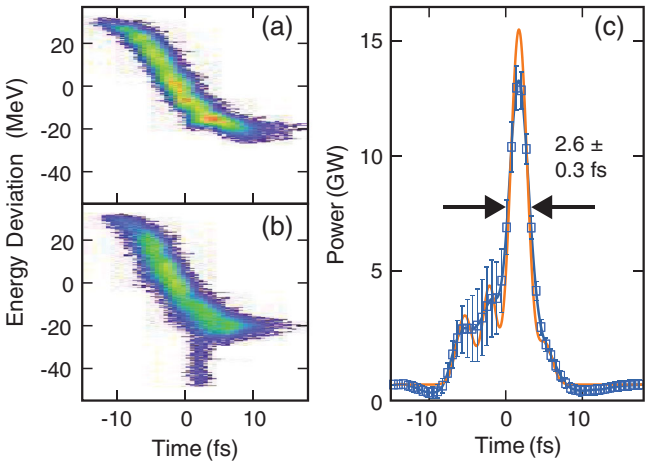

FIG. 5. *X*-band deflecting cavity (XTCAV) measurements of sub-5 fs, 1 keV x-ray pulse. The electron bunch charge is 20 pC with electron beam energy of 4.7 GeV. (a) One single-shot lasing-off image, (b) one single-shot lasing-on image, and (c) reconstructed x-ray profile with a calculated 2.6 fs FWHM duration. Adapted from Behrens *et al.*, 2014.

III. EXPERIMENTAL CHALLENGES, STRATEGIES, AND INSTRUMENTATION

A. Challenges of an x-ray FEL source

The x-ray science community today is benefiting from decades of progress made in synchrotron radiation technology. X-ray FEL sources, in contrast, are in their infancy and present many challenges that will need to be solved before fully exploiting their capabilities.

1. Restricted access to beams

X-ray FELs presently require long, complex undulator arrays to function (see Sec. II.A.1). These are costly and thus cannot be replicated to the extent that insertion devices are at storage ring-based x-ray light sources. As a consequence, the x-ray FEL facilities in operation or under construction have a limited number of independent FEL beams (one to three). This is in significant contrast to synchrotron facilities where many tens of independent x-ray beams permit dozens of experiments to operate simultaneously. As a consequence, the amount of beam time available at x-ray FEL facilities is severely restricted and users must go through a highly competitive process to gain access. This situation is not anticipated to change in the foreseeable future, even with new facilities coming on line and new techniques being developed that allow multiple simultaneous experiments (Boutet *et al.*, 2015; Feng *et al.*, 2015).

2. Source fluctuations

LCLS pulses fluctuate significantly in space (∼10% of the beam size), arrival time with respect to the linac reference clock (∼200 fs rms), per pulse energy (∼10% rms), central photon wavelength (∼0.1% rms), spectral shape, and temporal shape (cf. Table I). These fluctuations are a result of the stochastic nature of the SASE process as well as inherent limitations on the stability of the electron beam. The SASE process is very sensitive to the electron beam properties, and small fluctuations in these properties lead to amplified fluctuations in the produced x-ray beam. Understanding and eventually controlling these fluctuations has led to a diverse set of, and continual development of, advanced diagnostics such as timing correction (see Sec. III.C.2.c).

3. Beam coherence

X-ray FEL sources in general produce pulses of x rays with near-full transverse coherence (Vartanyants *et al.*, 2011; Gutt *et al.*, 2012; Lehmkühler *et al.*, 2014). While this characteristic offers many scientific opportunities, it presents a challenge to the x-ray optical systems used to manipulate the x-ray beam. For example, small deviations in the height error of mirrors produce phase shifts on the beam that manifest as undesirable intensity variations across the beam profile. In order to preserve the natural wave front profile of the source, such mirrors must maintain tolerances at the state of the art of typically <1 nm height error across a 1 m mirror profile. Stringent tolerances must also be adhered to for grating optics, monochromator crystals, and other transmissive optics for attenuation or diagnostics.

4. Damage

With single-pulse energies on the mJ level, x-ray FEL pulses are capable of raising the temperature of materials by thousands of degrees. A single shot can cause damage, even when unfocused. This presents significant challenges in the design and construction of optics and diagnostics systems. Unfortunately, cooling methods cannot address single-pulse damage due to the ultrashort duration of the pulse, which is much shorter than typical electron-phonon coupling times. This near-instantaneous temperature rise cannot be avoided and can generally be mitigated only by using materials that have a high melting point, high specific heat capacity, and low photoabsorption coefficient over the wavelengths of interest. In the case of experiment samples, either the pulses must be attenuated to a degree that allows the sample to return to its ground state before exposure to a subsequent pulse or the sample must be refreshed.

B. Experimental opportunities enhanced by x-ray FELs

1. Diffraction before destruction

When the LCLS beam is focused to a small spot size it can produce peak intensities of $10^{17} - 10^{21}$ W cm^{-2}. These high power densities are often required to generate a useful signal from a small sample, but inevitably destroy the sample in a single pulse. While this, at first glance, seems experimentally challenging and perhaps even undesirable, it also offers experimental opportunities. Very short pulses can traverse samples faster than radiation-induced atomic motions produce problematic structural changes. This can be especially useful in biological studies, where radiation damage represents a significant limitation. This was identified as a key advantage of x-ray FEL sources before they were built (Neutze *et al.*, 2000) and is now known as the diffraction-before-destruction concept, conceptually shown in Fig. 6. Since then, it has been realized that overcoming radiation damage is not only useful in diffraction studies but the concept can now more broadly be referred to as probe-before-destruction where, for example, damage-free spectroscopic information can also be obtained using short x-ray FEL pulses.

The first diffraction-before-destruction concept tests took place at the FLASH FEL in 2006 when it began operations at 32 nm. Instrumentation developed to support these experiments included novel detector systems with central holes capable of passing the transmitted FEL beam (Chapman *et al.*, 2006; Bajt *et al.*, 2008), substrate-free sample delivery (Bogan *et al.*, 2008), imaging of gas-phase clusters (Bostedt *et al.*, 2010), dynamic measurements (Barty *et al.*, 2008), and conceptual demonstration of 2D crystallography (Mancuso *et al.*, 2009). Methods that use sample design to enhance signal interpretations obtained with single FEL pulses were developed, using reference objects, such as point references and uniformly redundant arrays, to aid in image reconstruction (Boutet *et al.*, 2008; Marchesini *et al.*, 2008). These developments eventually led to the analysis of multiple diffraction patterns from similar samples to produce three-dimensional information (Loh *et al.*, 2010) and to the imaging of cells (Seibert *et al.*, 2010). Parallel technique development also took place at the SCSS (Shintake *et al.*, 2008; Yabashi *et al.*, 2013) with studies of radiation damage in coherent imaging (Park *et al.*, 2012).

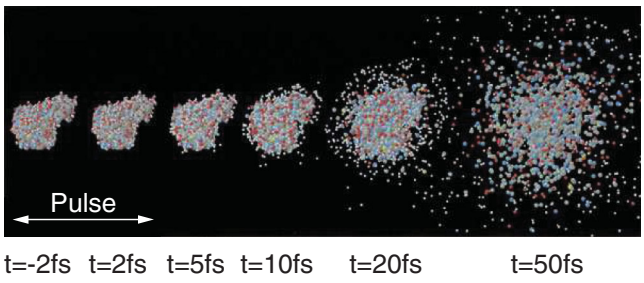

FIG. 6. The diffraction-before-destruction concept showing how nuclear motions caused by an x-ray FEL pulse can occur primarily after a suitably short pulse has passed through the sample. From Neutze *et al.*, 2000.

The FLASH facility enabled the first experimental verification of the diffraction-before-destruction concept, using a modern version of Newton's dusty mirror to study the time evolution of exposed samples (Chapman *et al.*, 2007), and to demonstrate the feasibility of using tamper layers to reduce sample motion during the pulses (Hau-Riege *et al.*, 2010b).

The operations start of LCLS with user-assisted commissioning in October 2009 immediately led to diffraction-before-destruction experiments (see Sec. IV.A) and structural biology measurements using the relatively long wavelengths usable at the time, with photon energies between 500 and 2000 eV (see Sec. IV.E). The availability of x rays above 2 keV a year later, which were capable of achieving atomic resolution, opened the door to high-resolution studies that could make full use of the capabilities of diffraction-before-destruction techniques. This allows mitigation, if not elimination, of the deleterious effects of radiation damage. Hard x rays allowed a resolution of 1.9 Å to be achieved with no observable damage using small protein crystals at room temperature (Boutet *et al.*, 2012).

Today the diffraction-before-destruction method is widely used at LCLS, and a large and growing literature describes simulations of damage during the x-ray FEL pulse and the theoretical range of applicability of the technique, including a recent review article (Chapman, Caleman, and Timneanu, 2014). The application of this technique is ubiquitous in the many science fields being advanced at LCLS and many examples are described in Sec. IV.

2. Nonlinear spectroscopy

X-ray based spectroscopic techniques have been essential for our understanding of the electronic structure of matter. So far, they have been limited to the linear regime where at most one photon is interacting with one atom in the sample at a given time. In the intense, focused beam of LCLS this picture changes dramatically, as multiple photons can interact with an atom during the pulse or even during the lifetime of a core-excited state (see Sec. IV.A.1).

Core-level photoelectron spectroscopy is a routine tool for electronic structure determination in atoms, molecules, and solids (Siegbahn, 1981). For studies of molecules with very similar species, e.g., of organic molecules, the binding energy

differences between the various entities can be smaller than the experimental resolution. This changes when double core-hole states are created through multiple ionization during the core-hole lifetime. The creation of such a double vacancy significantly shifts and separates the energy levels in the x-ray excited sample. In an atom, so-called hypersatellite Auger lines from double core-hole decay can be observed at hundreds of eV higher kinetic energy (Young *et al.*, 2010). In molecules, if the core holes are created at two different atoms, the binding energies associated with the double core-hole state become very sensitive to the local chemical environment, providing electronic structure information far beyond what can be accessed with linear x-ray spectroscopy (Cederbaum *et al.*, 1986; Santra, Kryzhevoi, and Cederbaum, 2009). The feasibility of using two-site double core-hole spectroscopy for chemical analysis with x-ray lasers was demonstrated with small molecules (Berrah *et al.*, 2011; Salen *et al.*, 2012). Combining this approach with time-resolved studies provides x-ray based tools for electronic dynamics investigations with unprecedented sensitivity.

Another powerful tool for electronic structure investigations with x rays is resonant inelastic x-ray scattering (RIXS) (Ament *et al.*, 2011). As a photon-in–photon-out technique, RIXS is the method of choice for investigations of bulk properties or samples with complex chemical environments. In the soft x-ray regime, in particular, RIXS suffers from limited resolution and poor efficiency as the core-vacancy decay is dominated by Auger processes. Extending RIXS to stimulated emission holds promise for increasing the efficiency of the technique by beating the competing Auger processes and directing the emission signal along the beam axis. First steps toward this goal have been taken at LCLS with atomic targets. In first experiments a $1s$-$2p$ inner-shell resonance in single ionized neon could be cycled, as evidenced by changes in the competing Auger-decay channel line shape (Kanter *et al.*, 2011). Shortly afterward, an x-ray FEL pumped x-ray laser in a dense neon gas target was demonstrated with a nonlinear gain curve spanning many orders of magnitude (Rohringer *et al.*, 2012). Subsequently, and also in a dense neon target, stimulated inelastic x-ray scattering was measured with many orders of magnitude amplification of the Raman signal before saturation (Weninger *et al.*, 2013). A recent experiment at FLASH has detected an increased directionality in the RIXS signal from crystalline silicon with about twice the intensity of the spontaneous background emission, exemplifying the concept of x-ray stimulated processes in the solid phase (Beye *et al.*, 2013b).

Future high-repetition-rate FELs offer the potential to produce multiple intense x-ray pulses with tunable wavelength. These sources promise to extend multidimensional and nonlinear spectroscopic techniques from the optical to the x-ray spectral regime (Mukamel *et al.*, 2013), far beyond what has been demonstrated to date (see Sec. V).

3. Time-resolved pump-probe dynamics

Pump-probe techniques with ultrafast lasers have proven fruitful for investigating and characterizing atomic motions and electronic structure changes that are the driving forces in a majority of physical, chemical, and biological processes (Zewail, 2000). A dynamic process is excited in an ensemble of atoms or molecules by an ultrashort light pulse (pump) and probed by a second, delayed pulse (probe). The dynamics of the process can be determined by combining the information from different delays between pump and probe pulses. Using this method, nonequilibrium states of matter during chemical reactions or phase transitions, for example, can be experimentally studied.

Typically, optical light can resolve only ~1-μm-sized structures, and as a result ultrafast optical pump-probe measurements are limited to spectroscopic information about outer atomic shell energy levels or to changes in optical constants in bulk materials that yield indirect structural information. Subpicosecond x-ray sources have been limited by the pulse intensities and were predominantly used for studying long-range order in solid sample systems (Siders *et al.*, 1999; Sokolowski-Tinten *et al.*, 2003). Intense picosecond pulses from synchrotron sources were able to resolve less-ordered or liquid samples, but the experimental results are limited by time resolution to dynamics of larger structures or kinematic transitions (Plech *et al.*, 2004). The accessibility of the different time and length scales for different light sources is conceptually shown in Fig. 7.

The intense, short x-ray FEL pulses provide a probe on the atomic length scale with the time scale of atomic motions. Additionally, x rays provide a powerful spectroscopic tool because their interactions with well-defined inner-shell electrons make them an element-specific and thereby a local probe by tuning the photon energy to specific transitions. Therefore, x-ray FELs can provide insight complementary to established ultrafast pump-probe techniques, as described in many examples in Sec. IV.

4. Coherent scattering

Over the past 20 years, experiments have been performed using synchrotron radiation sources to develop schemes and techniques that take advantage of partially coherent x-ray beams to study matter. This successfully paved the road to the development of robust coherent x-ray scattering techniques, which has mainly focused on coherent x-ray diffractive imaging (CXDI). In the CXDI method, coherent x-ray speckle patterns are detected and iterative phasing algorithms are

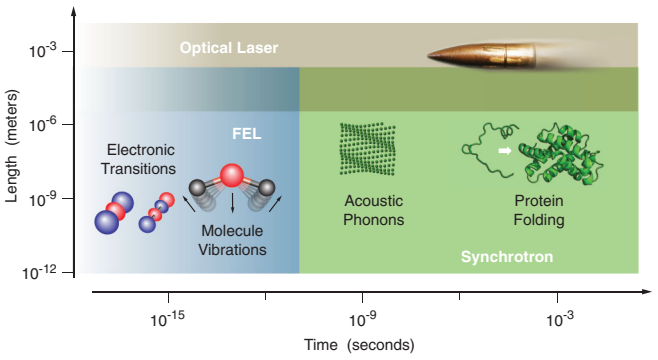

FIG. 7. Schematics of typical time scales and length scales of physical, chemical, and biological processes. Shaded regions indicate the time scales and length scales accessed by different light sources.

employed to reconstruct images without the use of imaging optics (Miao *et al.*, 1999). CXDI offers the possibility of reconstructing the projected or three-dimensional electronic density of materials or small objects with nanometer resolution and can, in some cases, provide even more information such as the three-dimensional strain field in a material (Miao *et al.*, 2015). Other x-ray methods rely on correlating coherent scattering speckle patterns, either in time to study dynamical processes using x-ray photon correlation spectroscopy (Sutton *et al.*, 1991; Shpyrko *et al.*, 2007; Grübel, Madsen, and Robert, 2008; Turner *et al.*, 2008) or with respect to other variables such as magnetic fields to study magnetic domain evolution (Pierce *et al.*, 2005).

X-ray FELs provide beams with nearly full transverse coherence (Vartanyants *et al.*, 2011; Gutt *et al.*, 2012; Lehmkühler *et al.*, 2014) although, as previously discussed, the longitudinal coherence is relatively poor and exhibits strong shot-to-shot fluctuations as a result of the SASE process (S. Lee *et al.*, 2012; Lee *et al.*, 2013). The coherent x-ray scattering techniques developed at synchrotrons can all be applied at x-ray FELs. These techniques are pursued using various LCLS instruments, where the large single-shot coherent flux and femtosecond pulse duration is leveraged to observe matter at the atomic length scale and to investigate ultrafast dynamical phenomena.

C. LCLS instrumentation

The LCLS beam (see Sec. II) is directed into six scientific instruments located in two experimental halls as illustrated in Fig. 8. The development of the instruments was primarily supported by the DOE Office of Basic Energy Sciences through different modalities. The Atomic, Molecular, and Optical (AMO) instrument was developed within the LCLS construction project. The X-ray Pump-Probe (XPP), X-ray Correlation Spectroscopy (XCS), and Coherent X-ray Imaging (CXI) instruments were built as a major item of equipment project called the LCLS Ultrafast Science Instrumentation (LUSI). Funding for the Matter in Extreme Conditions (MEC) instrument came from the DOE Office of Fusion Energy Sciences. The Soft X-Ray (SXR) instrument was funded by a third-party consortium whose membership included LCLS, Stanford University, Lawrence Berkeley National Laboratory (LBNL), University of Hamburg, and the Center for Free Electron Laser (CFEL). All six instruments are now operated by LCLS at SLAC.

1. X-ray instruments

Each instrument was designed and constructed to address the scientific thrust areas identified at the conception of LCLS (see Sec. I.C). Many fulfill a broader scientific reach than anticipated. For example, although XPP was the only instrument dedicated to pump-probe measurements (see Sec. III.B.3), nearly every instrument now employs an ultrafast optical pump laser system capable of generating excitation pulses tunable from THz to UV (Minitti *et al.*, 2015b). The x-ray transport and experimental systems were optimized by dividing the instruments into two spectral ranges. The AMO and SXR instruments accept soft x rays (250–2000 eV) and the XPP, XCS, CXI, and MEC instruments exploit hard x rays (>4 keV).

a. AMO

The AMO instrument is designed to provide a tight-focus, high-flux beam (Bozek, 2009; Bostedt *et al.*, 2013; Ferguson *et al.*, 2015). The instrument consists of Kirkpatrick-Baez (KB) mirror-focusing optics, beam diagnostics, and an optional split-and-delay unit capable of providing two x-ray pulses separated by up to 200 fs. Three end stations are used, with varying sample delivery and detection capabilities.

The LAMP experimental end station is similar to its predecessor, the CAMP instrument (Strüder *et al.*, 2010), a versatile apparatus for coherent diffractive imaging and spectroscopy applications. It consists of an interaction chamber, two pnCCD photon area detectors, and a double-sided electron and ion spectrometer. The High-Field Physics (HFP) end station is optimized for high-resolution ion and electron spectroscopy. It is lined with a double layer of μ metal to shield the interaction region from extraneous magnetic fields and consists of five electron time-of-flight spectrometers and one ion time-of-flight spectrometer. A third experimental end station, the diagnostics end station, is designed to house

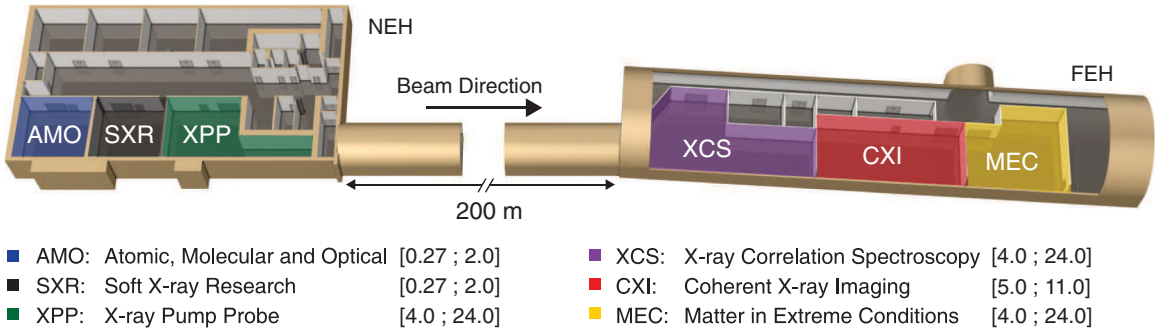

FIG. 8. The three instruments in the Near Experimental Hall (NEH) were commissioned first in a phased approach starting in October of 2009 with user science experiments on the AMO instrument, followed by SXR in July 2010 and XPP in October 2010. In the Far Experimental Hall (FEH) experiments began on CXI in February 2011 followed by XCS in November 2011 and MEC in April 2012 to form the complete facility. The x-ray energy range in keV is specified for each instrument in brackets. Third harmonic radiation is used for photon energies greater than 12.7 keV.

x-ray-optical pump-probe experiments with a large in-vacuum footprint.

b. SXR

The SXR instrument uses soft x-ray spectroscopic and resonant scattering methods for applications in ultrafast chemistry, magnetic imaging, and strongly correlated materials (Dakovski, Heimann *et al.*, 2015). The key component of the SXR instrument is the variable-line-spacing plane grating monochromator (Heimann *et al.*, 2011), which provides further control of the bandwidth of the FEL pulses (Tiedtke *et al.*, 2014). Adjustable focal length KB optics are used to create foci as small as $2.5 \times 2.3\ \mu m^2$ (Chalupský *et al.*, 2011) and which can be characterized using imprint methods and numerical phase recovery algorithms (Chalupský *et al.*, 2015).

The SXR instrument employs a wide range of experimental end stations (Schlotter *et al.*, 2012). The resonant coherent imaging end station features an area detector and flexible sample manipulation platform (Wang *et al.*, 2012). The resonant soft x-ray scattering end station hosts a cryogenic in-vacuum diffractometer and motorized THz optical setup (Doering *et al.*, 2011; Turner *et al.*, 2015). The liquid jet end station uses an x-ray emission grating spectrometer and various liquid sample delivery jets (Kunnus *et al.*, 2012). The surface science end station features a similar spectrometer, but in an ultrahigh vacuum environment with gas dosing capabilities to study surface chemistry (Katayama *et al.*, 2013). Finally, an electron beam ion trap has been integrated to study highly charged ions (Bernitt *et al.*, 2012). Each end station features a specialized experimental geometry and sample environment, as well as specialized detectors and timing diagnostics (Krupin *et al.*, 2012; Eckert *et al.*, 2015).

c. XPP

The XPP instrument is tailored for studying ultrafast phenomena with hard x rays in the 4–25 keV range using pump-probe techniques (Chollet *et al.*, 2015). The x-ray beam entering the XPP instrument can be transported to the sample with the full SASE bandwidth or it can be bandpass filtered by either of two monochromator systems.

The main sample stage is formed by a large-load-capacity goniometer that allows positioning of larger-scale sample environments such as vacuum chambers. The goniometer stage can be configured into an ambient environment diffractometer. A ceiling-mounted robot arm positions x-ray area detectors with 50 μm precision, which is less than a typical detector pixel size, throughout the space accessible around the sample. The XPP instrument can use a Cornell-SLAC pixel array detector (CSPAD) 2.3 megapixel camera with single-photon sensitivity (Koerner *et al.*, 2009; Hart *et al.*, 2012a, 2012b; Carini *et al.*, 2014; Blaj *et al.*, 2015), as well as a Rayonix MX170-HS detector, which combines high dynamic range with a large sensitive area ($170 \times 170\ mm^2$). The CSPAD is a multimegapixel area detector that can operate at 120 Hz to collect diffraction patterns from every pulse. The sample environments on the XPP instrument are specialized and include a multipurpose vacuum chamber, a liquid jet chamber for diffuse scattering and spectroscopy experiments, and a nitrogen cryostream for temperature control in ambient environment experiments.

d. XCS

The XCS instrument is primarily designed to study equilibrium dynamics in condensed matter systems with coherent scattering techniques using 4–25 keV x rays (Robert *et al.*, 2013; Alonso-Mori *et al.*, 2015). The main experimental method is x-ray photon correlation spectroscopy (see Sec. III.B.4), which probes the temporal correlations of systems in equilibrium on the nanometer to micrometer length scale (Grübel, Madsen, and Robert, 2008). The study of dynamics on the XCS instrument is divided into two regimes: Slow (millisecond) dynamics are studied using the 120 Hz pulse structure of LCLS and fast (subnanosecond) dynamics are studied by the division, delay, and recombination of x-ray pulses.

Crystal monochromators are used to tailor the energy resolution, or longitudinal coherence length, of the x-ray beam. A split-and-delay unit can be inserted to access dynamics on the subnanosecond time scale (Roseker *et al.*, 2009, 2012). Sample environments can range from ultrahigh vacuum to liquid injector in air. A four-circle diffractometer provides precise manipulation for sample environments with a sphere of confusion of less than 20 μm. X-ray area detectors can be rotated up to 55 deg in the horizontal plane as far as 7.5 m from the sample.

e. CXI

The CXI instrument is primarily an in-vacuum forward scattering instrument using hard x rays in the 5–11 keV range (Boutet and Williams, 2010; Liang *et al.*, 2015). The design of CXI is optimized for diffraction-before-destruction measurements on biological samples as described in Sec. III.B.1. Multiple experimental geometries exploit this capability, with the ability to interface with a variety of sample delivery techniques such as liquid jet injectors (Sierra *et al.*, 2012; Weierstall, 2014; Weierstall *et al.*, 2014) and fixed-target systems (Frank *et al.*, 2014; Hunter *et al.*, 2014). CXI is also well suited for coherent diffractive imaging experiments using hard x rays, where removal of scattering from ambient gas is required to study very small objects such as viruses and molecules.

Two independent KB mirror pairs are used to produce nominally 1 μm and 100 nm FWHM foci (Siewert *et al.*, 2012). The beam delivered to CXI is used with minimal optical elements to maximize the number of photons incident on the sample. X-ray scattering patterns are collected with in-vacuum CSPAD detectors (Koerner *et al.*, 2009; Hart *et al.*, 2012a, 2012b; Carini *et al.*, 2014; Blaj *et al.*, 2015) and represent a key enabling technology that is central to almost every experiment using the CXI instrument.

f. MEC

The MEC instrument is specifically designed to study high-energy density (HED) matter whose energy density exceeds $10^{11}\ Jm^{-3}$, or where the pressure exceeds 1 Mbar (Lee, 2007; Nagler *et al.*, 2015). HED matter is transient and very difficult

to simultaneously create, characterize, and measure in a laboratory. The hard x-ray photon energies, high flux, and short pulse duration of the LCLS beam are well suited to examine time-dependent changes in HED matter.

The MEC instrument incorporates high peak power and high-energy optical-laser systems and a suite of dedicated diagnostics tailored for the particular needs of this field of science. Two optical-laser systems are installed at MEC: a 2.4 mHz (i.e., every ~7 min) Nd:glass laser system providing variable pulse length from 2 up to 200 ns at a wavelength of 527 nm and a 5 Hz Ti:sapphire laser system delivering 1.5 J in a 50 fs pulse duration at a wavelength of 800 nm. The nanosecond laser pulse from the Nd:glass laser system can produce a shock wave in materials, resulting in dynamic high-pressure conditions ranging from tens to hundreds of GPa and temperatures as high as tens of eV. The femtosecond laser system enables high harmonic generation or hot electron generation, resulting in secondary sources such as betatron x-ray radiation, proton beams, or ion beams. Target diagnostics allow direct measurement of materials thermodynamic properties in a single shot and provide insight into the dynamics of phase transitions. The MEC vacuum chamber simultaneously accommodates 6-degrees-of-freedom sample stages, spectrometers, area detectors, and relay optics.

2. Diagnostics

LCLS x-ray pulses exhibit significant fluctuations in pulse energy, spectrum, time, and space as a result of the SASE process described in Secs. II.A.1 and III.A.2, and inherent limitations on the stability of the electron beam that drives the FEL. Such pulse-by-pulse variations limit experimental sensitivity unless diagnostic measurements can be used to correct the variations.

a. Pulse energy diagnostics

Pulse energy diagnostics play a particularly important role for experiments, such as pump-probe experiments, measuring difference signals between a ground and excited state. There are various types of these devices deployed at LCLS: gas fluorescence detectors (Hau-Riege *et al.*, 2010a), photon scattering monitors (Feng *et al.*, 2011), and charged particle collectors (Moeller *et al.*, 2015). All of these devices operate on a pulse-by-pulse basis and detect the pulse energy (relative or absolute) in a noninvasive manner.

b. Spectral diagnostics

Quantitative measurement of the spectral content of each x-ray pulse is critical for many experimental applications and for tuning the FEL performance parameters. The SXR grating monochromator (see Sec. III.C.1.b) is used for spectral measurements and FEL tuning in the soft x-ray wavelength range (Heimann *et al.*, 2011) and achieves a 300 meV or better spectral resolution below 2 keV. A transmissive single-shot x-ray spectrometer was developed for operation in the hard x-ray regime (Zhu *et al.*, 2012). This spectrometer has a ~100 meV spectral resolution, which can separate the individual spectral spikes that are characteristic of the SASE process.

c. Timing diagnostics

For time-resolved measurements, the level of synchronization of the external source (e.g., an ultrafast pump laser) with the FEL pulse is often the factor that limits the achieved time resolution. Arrival time fluctuations or jitter between the pump (optical laser) and probe (FEL) can be as large as a few hundred femtoseconds due to the stability of the electron beam acceleration with respect to a rf timing reference, the SASE process, and the synchronization of the optical laser to the rf timing reference. Minimization of the timing uncertainty is achieved by stabilizing drift in the distribution of the rf reference signals as well as measuring the electron bunch arrival to correct drift (Minitti *et al.*, 2015b). Additionally, diagnostics capable of measuring the relative pulse arrival times allow postprocessing of the experimental data and significantly improve the achieved temporal resolution (Beye *et al.*, 2012; Schorb *et al.*, 2012a; Harmand *et al.*, 2013; Bionta *et al.*, 2014; Hartmann *et al.*, 2014). The relative arrival time is determined to ~10 fs with these methods.

d. X-ray detectors

Efficient x-ray detection at LCLS is a challenge due to the very short pulse duration of the source and the large number of photons per pulse. The most practical approach for addressing these issues has been to employ integrating detectors with short collection times. In most cases, it is also highly desirable to capture the outcome of every pulse from the source, leading to the specification of a detector that operates at a rate of at least 120 Hz. A detailed overview of LCLS detectors is presented by Blaj *et al.* (2015).

IV. SCIENCE WITH LCLS

As described in Sec. II, LCLS differs from existing x-ray sources in a number of important ways; the time structure, intensity, and coherence properties of its pulses encourage a reimagining of many traditional methods. The combination of femtosecond-scale pulse duration with as many photons per pulse as are typically available in 1 s at synchrotron sources naturally fits certain types and areas of science. The opportunities stemming from the source characteristics described in Sec. III.A lead directly to novel techniques that make the best use of the capabilities of the beam, as described in Sec. III.B. The identification of areas of science where LCLS was expected to have an impact are outlined in Sec. I.C, followed from the source properties and the techniques that could take advantage of them.

LCLS, via multiple projects, built a suite of instruments, described in Sec. III.C, primarily aimed at the expected science cases best matched to the source. These areas of science have naturally flourished, with user demand and access to specific instruments driving the level of scientific results.

LCLS is a user facility open to scientists worldwide. There are typically two calls for proposals per year and an external peer-review committee evaluates proposals based on scientific merit and instrument suitability. Over the first five years of operation, LCLS performed 266 experiments covering a broad range of scientific disciplines: atomic, molecular, and optical

physics (20%), condensed matter physics (22%), matter in extreme condition (11%), chemistry and soft matter (13%), and biology (26%). The scientific results for each of these disciplines, generated from work published prior to the submission of this article, are described in detail in this section. It is important to note that the typical average time between the realization of an experiment and the publication of the scientific results is about two years. At times, in order to further illustrate the various points described in these sections, published references from experiments performed after the first five years have been included wherever appropriate.

A. Atomic, molecular, and optical physics

The first experiments at LCLS were targeted at understanding the fundamental physics of the interaction of intense x-ray pulses with atoms, molecules, and clusters, but also at making use of the intense x-ray pulses for novel spectroscopy approaches. The field then rapidly developed and incorporated pump-probe techniques to investigate dynamical processes or prepared transient states. First experiments were performed in the field of nonlinear x-ray physics, proving concepts that had sometimes been envisioned decades ago but could only be fully explored with LCLS. Single-shot imaging applications now merge into AMO physics and open completely new possibilities for investigating dilute gas-phase samples and quantum phenomena.

1. High-intensity x-ray-matter interaction

With LCLS delivering power densities of 10^{18} W cm^{-2} in the soft x-ray regime and in excess of 10^{20} W cm^{-2} in the hard x-ray regime, a new chapter in the history of intense light-matter interaction opened. Compared to the optical regime, the intense x-ray photon field cannot be well described by a quasistatic description for intense light-matter interaction, assuming that the oscillating light field is slow compared to the bound electron motion. Further, x rays predominantly interact with inner-shell electrons, and therefore the intense x-ray pulses ionize atoms from the inside out, with the inner-shell vacancies decaying on time scales comparable to the x-ray pulse length. As an example, focusing intense LCLS pulses containing on the order of 10^{12} photons per pulse to a typical spot size of 1 μm^2 results in a fluence of 10^{20} photons cm^{-2} per pulse. Typical nonresonant absorption cross sections in the soft x-ray regime range from $\sigma = 0.1$ for light atoms to $\sigma = 1$ Mbarn for heavy atoms. Thus, in the focused x-ray pulses of LCLS, about 10 to 100 photons fall into the cross section of each atom, and it can be immediately concluded that multiphoton ionization is the rule, not the exception.

a. Absorption of highly intense x rays in atoms

The initial experiments were aimed at understanding the ionization of neon in intense x-ray pulses (Young *et al.*, 2010). Neon was chosen as a model system with a simple electronic structure, and an absorption edge comfortably in the x-ray spectral regime at 870 eV. The experiment showed that the atoms are efficiently ionized to the highest charge state energetically accessible by one-photon ionization as schematically shown in Fig. 9. In the most extreme case, an x-ray pulse with photon energy greater than the Ne^{9+} ionization potential stripped all ten electrons from the neon atom, leaving only a naked nucleus behind. In the ion yield spectra, the even charge states were generally enhanced over the odd charge states due to Auger decay following each photoionization step. For higher charge states, deviations from the photoionization and Auger-decay alternation were identified, stemming from increasing core-hole lifetimes in highly charged ions, which increased the probability of double core-hole ionization and also the yield of the fluorescence decay channel. The experiment firmly established that sequential single-photon ionization (cf. Fig. 9) is the dominant absorption process in the soft x-ray regime at intensities up to 10^{18} W cm^{-2}, confirming preceding theoretical predictions (Rohringer and Santra, 2007). A subsequent study aimed at nonsequential ionization of neon found evidence for nonlinear two-photon absorption (Doumy *et al.*, 2011). Even though the process is weak compared to the sequential ionization, the study found that the nonlinear two-photon ionization cross section is larger than expected, possibly due to near resonance behavior, setting the stage for nonlinear x-ray physics.

While the world of intense x-ray absorption looked clean and simple when using neon as a target, a study of high Z elements produced surprises (Rudek *et al.*, 2012). First, xenon atoms exposed to 10^{17} W cm^{-2} at a photon energy of 1500 eV revealed charge states up to Xe^{36+}, far beyond the single-photon ionization limit from the ground state of Xe^{26+}. Second, xenon atoms irradiated with 1500 eV photons show higher charge states and more abundance at high-charge states than xenon atoms irradiated at 2000 eV with a similar power density. These results are a reminder of the efficient multiphotoionization of xenon observed in intense extreme ultraviolet pulses (Sorokin *et al.*, 2007), but in the x-ray spectral regime they appear at a first glance at odds with the sequential

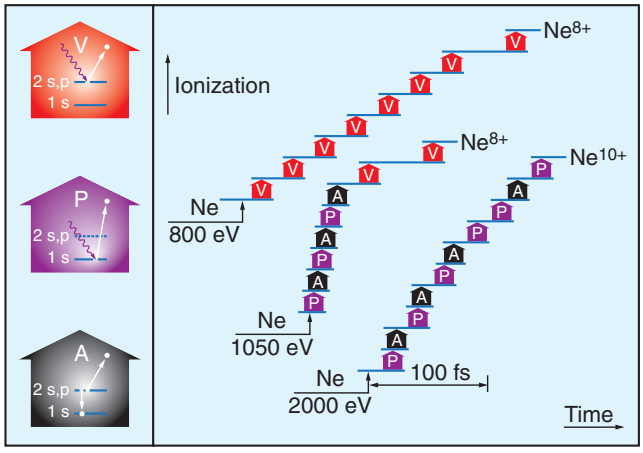

FIG. 9. Diagram of sequential x-ray multiphoton ionization in neon. The highest possible charge states are the ones energetically accessible by one-photon ionization. Below the Ne 1*s* threshold only valence electrons are ionized (V process); above the threshold, photoionization (P) and Auger (A) decay processes alternate. For increasing charge states the core-hole lifetimes increase, leading to subsequent photoionization (P–P) processes and x-ray induced x-ray transparency. From Young *et al.*, 2010.

ionization picture. However, they can be explained when resonance effects are considered. In the present case of Xe ionization at 1500 eV, unoccupied orbitals and densely packed Rydberg states can be energetically pulled down below the ionization energy for the higher charge states created during the x-ray pulse, opening resonant transition channels. The electrons in the outer shells can then undergo Auger decay or autoionizing transitions involving other outer-shell electrons. This process was dubbed resonance enhanced x-ray multiple ionization. It becomes particularly efficient in the energy windows above inner-shell ionization thresholds, explaining the experimentally observed strong enhancement of Xe ionization at 1500 compared to 2000 eV.

The x-ray ionization is further enhanced through bound-to-bound transitions that can become accessible during the x-ray pulse. These "hidden" resonances were first observed in subthreshold ionization of neon (Kanter *et al.*, 2011). In this experiment, the leading edge of the x-ray pulse opened a $2p$ valence hole, and subsequently the $1s \rightarrow 2p$ transition could be driven. While this may appear to be a rather specialized case, such bound-to-bound transitions are essential for understanding the production of high-charge states with ionization potentials far beyond the incoming photon energy in argon (Ho *et al.*, 2014). From a theoretical perspective, the ionization of atoms in intense x-ray pulses is a rather daunting challenge, but the computational methods are rapidly evolving. Even though the ionization processes can be described by a sequence of one-photon ionization and decay processes, the number of possible electronic configurations can become extremely large. Son and Santra (2012) developed a Monte Carlo scheme to solve the rate equation model for ionization of atoms in intense x-ray pulses. In this approach, the cross sections for photoionization and vacancy decay are calculated for all multiple-hole configurations, and then Monte Carlo sampling finds the probable pathway to reach the final charge states with the help of precalculated tables of atomic data. This approach was extended to include bound-to-bound transitions, which vastly increases the number of possible electronic configurations over nonresonant conditions (Ho *et al.*, 2014).

The overwhelming complexity of the ionization of many-electron systems in intense x-ray pulses, compared to the simple case of neon (cf. Fig. 9), is demonstrated in Fig. 10. Here the possible transition pathways are theoretically tracked for argon atoms illuminated with 480 eV photons and a photon pulse energy of 0.2 mJ (Ho *et al.*, 2014). The pathway to the experimentally observed highest charge state Ar^{11+} from the Ar ground state is highlighted in colors other than green. This pathway includes all the processes discussed previously, namely, photoionization, Auger decay and autoionization, fluorescence decay, and resonant excitation processes. The inset shows the electronic configurations involved in this pathway in detail. Following these steps it can be seen that sometimes multiple ionization events occur before the relaxation event.

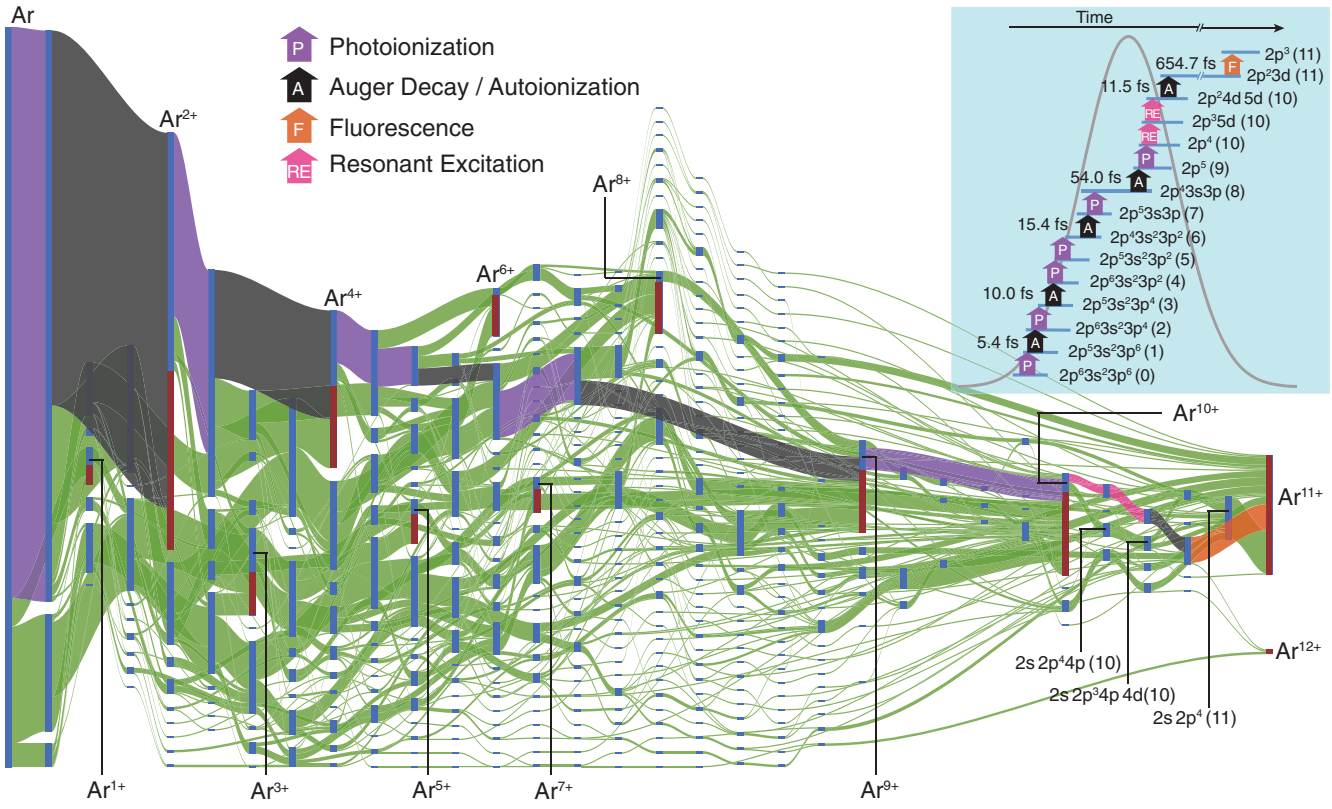

FIG. 10. Sankey diagram illustrating the transition probabilities of argon atoms illuminated with intense x-ray pulses at 480 eV. Vertical bars present possible electronic configurations, and the width of each branch indicates the transition probability. The most prominent ionization pathway to reach the highest observed charge state Ar^{11+} from the Ar ground state is highlighted in colors other than green. The inset shows the electronic configurations involved in the exemplary pathway. From Ho *et al.*, 2014.

b. Double core-hole states and applications to spectroscopy

Already single-photon double ionization can lead to the creation of double core-hole states, often also referred to as hollow-atom states (Diamant *et al.*, 2000; Hikosaka *et al.*, 2007). The cross section for this process, however, is orders of magnitude below the single core-hole ionization. The production of double core-hole states can be greatly increased in intense x-ray pulses through multiple core-level photoionization events during the core-vacancy lifetime. The creation of double core-hole states in an atomic target at LCLS was first demonstrated by detecting double core-hole Auger spectra (Young *et al.*, 2010). The yield of the so-called hypersatellite lines was 30 times larger compared to earlier synchrotron experiments. A subsequent study about the dynamics of hollow-atom formation employed the partial covariance mapping technique to identify multiple competing ionization channels leading to the same final ion charge state (Frasinski *et al.*, 2013). With this technique, it was possible to clearly distinguish between the time sequences of the ionization events and to identify previously unobserved ionization sequences of simultaneous emission of core and valence electrons that share the photon energy. In molecules, multiple double core-hole states can be distinguished. Either vacancies can be created on a single atomic site—a single-site double core hole—or the vacancies can be created on different sites—a two-site double core hole. Photoelectron measurements on N_2 show that the two states differ significantly in their binding energies, with the single-site double core holes having a significantly larger overall energy shift than their two-site counterparts (Fang *et al.*, 2010). Further, compared to the single core-hole state, the single-site double core holes exhibit a much more anisotropic Auger electron angular distribution (Cryan *et al.*, 2010).

The controlled creation of two-site double core holes with intense x-ray pulses from free-electron lasers holds great promise for photoelectron spectroscopy with enhanced chemical sensitivity (see Sec. III.B.2). The binding energies associated with the double core-hole state are a sensitive probe of the chemical environment (Cederbaum *et al.*, 1986; Santra, Kryzhevoi, and Cederbaum, 2009). The clear experimental identification of two-site double core holes in molecules, however, is not a trivial undertaking. Their overall energetic shift compared to the main Auger line is 10 to 20 eV, which is relatively small. Additional spectral congestion can come from competing ionization and decay channels, e.g., Auger decay of the constantly photoionized sample (Fang *et al.*, 2010). Advances in experimental schemes, combining efficient spectrometers with multiparticle spectroscopy techniques, and data analysis utilizing covariance mapping, have allowed one to better disentangle the various ionization channels and to clearly identify the signatures of the double core-hole states (Mucke *et al.*, 2015).

When x-ray pulse durations comparable to the Auger lifetime are used, the creation of double core-hole states is enhanced over the sequential photoionization and they can clearly be identified (Berrah *et al.*, 2011). In Fig. 11, the measured two-site double core holes and their agreement with theory are shown. The data have been taken with sub-10-femtosecond x-ray pulses under focused and defocused

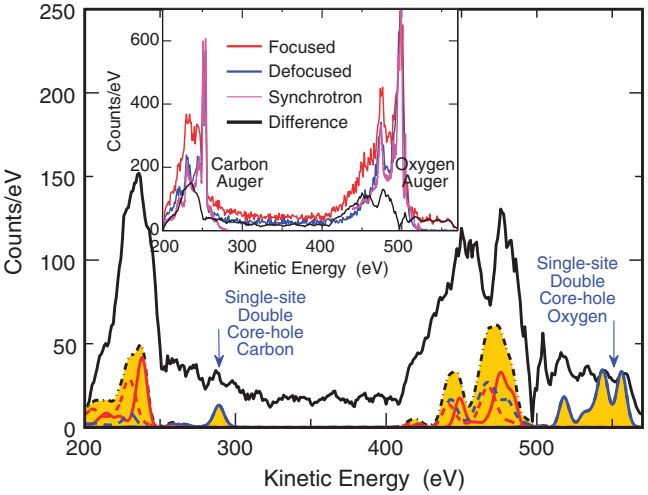

FIG. 11. Measured Auger spectra and their comparison to calculated double core-hole Auger spectra. Inset: The data are taken with different intensities and for reference at a synchrotron radiation source. Main panel: The difference of the two FEL x-ray intensities (black line) shows spectral intensity similar to the calculated spectra (yellow). Adapted from Berrah *et al.*, 2011.

conditions. The difference spectra reveal the power-density-dependent creation of double core-hole states. In a subsequent publication, the binding energies for double core-hole states for a series of small molecules are reported (Salen *et al.*, 2012). For example, the difference in the double ionization potential induced by one oxygen atom when going from CO to CO_2 is measured to be 6.7 eV for the two-site double states compared to 0.3 eV for the single ionization potential. The data show that the two-site double core-hole spectra exhibit an increased sensitivity by more than an order of magnitude. For completeness in recent years coincident photoelectron measurements at synchrotron radiation sources with efficient spectrometers have also allowed measuring single-site double core-hole states from single-photon ionization with great clarity (Eland *et al.*, 2010; Lablanquie *et al.*, 2011). It can be expected that the improving experimental schemes in combination with the upcoming high-repetition rate free-electron lasers (Sec. V.B) will greatly benefit this novel spectroscopy approach.

c. X-ray induced transparency

The x-ray absorption cross section is proportional to the electron population in the inner-shell levels. When an inner-shell electron is removed, the absorption cross section is transiently decreased until the vacancy is filled. As a consequence, shorter, more intense x-ray pulses are less efficiently absorbed than longer pulses of the same pulse energy. In experiments, ion yield spectra show that shorter pulses produce lower average charge states in atoms (Young *et al.*, 2010), molecules (Hoener *et al.*, 2010), and nanoclusters (Schorb *et al.*, 2012b) compared to longer pulses with the same pulse energy. Similar experiments in the extreme ultraviolet spectral regime, involving the shallow core levels of aluminum, showed that also in solid samples the absorption can become saturated with increasing fluence (Nagler *et al.*,

2009). These effects were dubbed x-ray induced transparency, core-level bleaching, or frustrated absorption. X-ray induced transparency becomes increasingly important for higher charge states, as both the single and double core-hole lifetimes increase significantly with increasing ionization. For example, the single core-hole lifetime in Ne^{1+} is only 2.4 fs, but for Ne^{7+} it is already 23 fs, about an order of magnitude longer and comparable to the typical x-ray pulse length (Young *et al.*, 2010).

Detailed knowledge of the ionization dynamics in intense x-ray pulses has direct implications for FEL applications such as single-shot x-ray scattering experiments (see Secs. IV.E.1 and IV.E.5). To a first approximation, the x-ray absorption cross section is proportional to the electron population in the inner-shell levels, but the scattering process is proportional to the total numbers of electrons in the system. Using neon again as an example, the photoabsorption cross section σ_{photo} for a double core-hole state with 1 Å radiation is reduced 20-fold to 11 barns, equal to the coherent scattering cross section σ_{scat}, and the same trend holds for hollow carbon (Young *et al.*, 2010). This numerical example shows that for coherent imaging experiments it is best to use intense x-ray pulses with durations similar to or below the hollow-atom lifetime (see Sec. IV.E).

d. Extended systems and complex environments

The ionization dynamics in intense light pulses can change dramatically with sample size. To investigate size-dependent effects in the intermediate regime between atoms, on the one hand, and bulk samples (see Sec. IV.C), on the other hand, clusters and nanoparticles are ideal. It was shown in the optical spectral regime that at high intensities these nanometer-sized samples very efficiently absorb energy from the light field through plasma heating processes (Fennel *et al.*, 2010). Going toward shorter wavelengths it was established early on that photoionization heating is the dominant pathway for energy absorption in extended systems and that collective effects become negligible (Bostedt *et al.*, 2008). First experiments with van der Waals clusters at LCLS have confirmed these results for intense x-ray pulses (Gorkhover *et al.*, 2012; Thomas *et al.*, 2012; Murphy *et al.*, 2014), but the high photon energies lead to additional consequences. The x-ray photon energies efficiently ionize the nanometer-sized sample, and depending on photon energy and sample size, most of the photoelectrons and Auger electrons are trapped in the deep Coulomb potential and a highly charged nanoplasma is formed. For the highest exposure intensities (cf. Sec. IV.A.4) this nanoplasma disintegrates so rapidly that electron-ion recombination is efficiently suppressed (Gorkhover *et al.*, 2012). Furthermore, the formation of the nanoplasma alters the x-ray ionization dynamics of the clusters and of extended samples in general (Schorb *et al.*, 2012b). The delocalization of the valence electrons in the x-ray-induced nanoplasma decreases the Auger rates and thus increases the inner-shell lifetimes. As a consequence, nanometer-sized samples exhibit an increased x-ray-induced transparency and absorb the femtosecond x-ray pulses less efficiently than smaller molecules or atoms. The fragmentation dynamics of simpler systems with known initial geometry, such as C_{60}, can be well described with classical mechanics and it is predicted that this approach scales well to larger systems such as biomolecules (Murphy *et al.*, 2014).

In complex environments consisting of a mix of light and heavy elements, charge redistribution becomes important and can significantly alter the fragmentation dynamics (Erk *et al.*, 2013). The heavy atom can absorb multiple photons from the x-ray pulse due to its higher absorption cross section. The charge is then redistributed to the molecular environment, leading to Coulomb explosions with high fragment kinetic energies. A study about the ionization dynamics of methylselenol (CH_3SeH) in 5 fs x-ray pulses showed that the charge is efficiently transferred from the Se absorption center to the surrounding carbon atoms. The Se-C bond length changes by more than 1 Å during the ionization process and even more for the lighter hydrogen atoms.

2. Ultrafast and time-resolved studies

X-ray based spectroscopy techniques yield unique insight into local electronic structure with element specificity (Sec. IV.D). The femtosecond x-ray pulses from free-electron laser sources allow using the x-ray spectroscopy toolkit for investigating transient states or time-dependent processes (Sec. III.B.3). In addition to the classical pump-probe approach, the short pulse structure can also be used to investigate ultradilute systems, effectively increasing the signal-to-noise ratio. For all these studies, the time structure of the free-electron laser pulses is exploited rather than the peak intensity. In fact, often these experiments are performed with only moderately focused x-ray pulses in order to avoid nonlinear excitation of the sample.

a. Prepared states

Coherent control techniques allow the preparation of molecules in defined transient states. A classic example is the impulsive or adiabatic alignment of molecular assemblies with optical lasers (Stapelfeldt and Seideman, 2003). With these techniques it is possible to transiently fix the molecular reference frame with respect to the laboratory frame. A variety of experiments have pursued this strategy for angle-resolved Auger spectroscopy (Cryan *et al.*, 2010, 2012), photoelectron diffraction in molecules (Boll *et al.*, 2013; Rolles *et al.*, 2014), or diffraction imaging of molecules (Küpper *et al.*, 2014); see Sec. IV.A.4. Compared to the commonly applied and very successful electron-ion coincidence techniques (Shigemasa *et al.*, 1995; Becker, 2000) and momentum spectroscopy approaches (Dörner *et al.*, 2000; Ullrich *et al.*, 2003), there are a few advantages. First, these methods typically rely on the axial-recoil approximation, limiting their generality. Further, the momentum of the ionic fragments is measured after the reaction and the initial orientation of the molecule is determined in the data postanalysis, restricting this method to reactions involving dissociative channels. Rotational motion of the molecule can compete with the time scale of the dissociative channel, blurring the results.

Photoionization and Auger-decay measurements made in the molecular frame are correlated with the symmetry of the molecule, and this symmetry gives insight into the electronic structure and dynamics. Impulsive, stimulated Raman

scattering leads to transiently aligned molecules in a field-free environment (Glownia *et al.*, 2010). Angle-resolved electron spectroscopy of single-site double core holes in nitrogen molecules showed significantly less isotropic Auger emission compared to the angular yield of the regular Auger line, despite the qualitatively similar line shapes of both processes (Cryan *et al.*, 2010). In a similar study, the angle-resolved Auger spectra for impulsively aligned nitrogen molecules were recorded with high resolution (Cryan *et al.*, 2012), yielding better insight into the spectral features of the Auger lines and even reassigning states in the well-studied nitrogen molecule.

Photoelectron diffraction allows structure determination with high spatial resolution and, if inner-shell electrons are used, sensitivity to the local chemical environment. While this technique is well established for investigations on solids, surfaces, and adsorbates, it has been difficult to apply it to gas-phase molecules because the molecular reference frame has to be known. In a first proof-of-principle experiment, photoelectron diffraction images of adiabatically aligned 1-ethynyl-4-fluorobenzene (C_8H_5F, also referred to as pFAB) molecules in the gas phase have been recorded at LCLS (Boll *et al.*, 2013). The measured angular distribution of the fluorine 1*s* photoelectrons shows a pronounced dependence on their kinetic energies, which compare well to density functional theory (DFT) calculations. In Fig. 12, the calculated fluorine 1*s* photoelectron angular distributions are shown for pFAB in (a) the equilibrium geometry, (b) with doubled F-C bond length, and (c) and (d) in two proposed transition states. In the calculation, only the position of the fluorine atom and the adjacent hydrogen atom have been varied, already causing substantial changes in the photoelectron distributions. The sensitivity of the method to the local geometric structure and bond configuration makes it a strong candidate for time-resolved studies (Rolles *et al.*, 2014).

b. Time-resolved x-ray spectroscopy

The classic application of the pump-probe technique is following the time evolution of an excited system (Sec. III.B.3). The combination of optical and x-ray laser pulses offers unique opportunities. Optical photons interact with the valence electrons responsible for molecular bonds. X-ray photons interact primarily with inner-shell electrons localized at the individual atoms and thus yield local electronic structure information. To date, time-resolved x-ray spectroscopy following optical excitation has been used for very different purposes and different approaches.

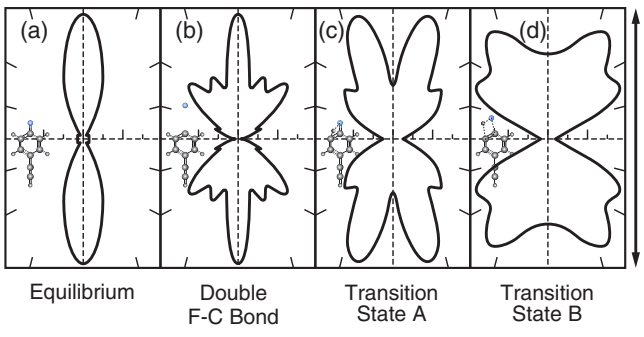

FIG. 12. Calculated fluorine 1*s* photoelectron angular distributions with 45 eV kinetic energy for a pFAB molecule in (a) the equilibrium geometry, (b) with doubled F-C bond length, and in (c) and (d) two proposed transition states. The molecules are one dimensionally aligned and the x-ray polarization is along the arrow. The distributions show a profound sensitivity to the local chemical environment. Adapted from Boll *et al.*, 2013.

One study aimed at following charge-transfer processes in fragmenting molecules (Erk *et al.*, 2014). Charge-transfer processes are the fundamental drivers in many important transformations in physics, chemistry, and biology, particularly in the making and breaking of chemical bonds. The investigation of charge-transfer processes with ion-atom or ion-molecule collisions is central to atomic physics (Lubinski *et al.*, 2001). Expanding this work to time-resolved pump-probe studies at LCLS brings many advantages compared to experiments with ion collisions. Fragmentation of the molecule allows precise control of the internuclear distance as a function of delay time. Further, the fragmentation is slow compared to the charge-transfer process and therefore the processes can be approximated in a static description. The key difficulties for investigating charge-transfer processes in molecules are the creation of spatially localized charge and identifying a clear signature of the transfer. Both difficulties can be overcome at LCLS with a couple of tricks. The sample molecule iodomethane (CH_3I) was probed with x-ray energies of 1500 eV above the iodine *M*-shell excitation energy. At that photon energy, iodine was ionized about 60 times more efficiently than the surrounding carbon atoms. The iodine inner-shell vacancies that were created by the x-ray pulse were rapidly filled through Auger cascades from higher lying shells, leading to a large, localized charge. Further, iodomethane can be dissociated with near-infrared pulses in a well-defined way, with the dominant channels being $CH_3 + I^+$ (0,1 channel), $CH_3^+ + I$ (1,0 channel), or $CH_3^+ + I^+$ (1,1 channel). Following the optically induced dissociation, the internuclear separations between the CH_3 and atomic I fragments are defined by the time delay between the near-infrared and ionizing x-ray pulses. In the experiment, delay-dependent kinetic-energy distributions of the charged fragments were recorded, which allowed identification of the three dissociation channels, as well as tracing of the charge-transfer dynamics as a function of time and thus fragment separation. An example map is shown in Fig. 13 for I^{6+} ions. Because the x-ray pulse almost exclusively ionizes the iodine fragment, the (1,0) and (0,1) channels result in a Coulomb explosion of the molecule with a strong change in kinetic energy at early delay times [channel 2 in Fig. 13(a)]. Channel number 3, on the other hand, appears only after a distinct delay with very low kinetic energies. It stems from the (0,1) channel after time delays that do not allow the charge to redistribute within the molecule. In the projection in Fig. 13(b), it can be seen that after 300 fs the ion yield for I^{6+} leveled off, and thus the distance between the methyl group and iodine fragments became too large for further charge transfer. The data can be well described by a classical over-the-barrier charge-transfer model showing that, at a critical separation, the height of the classical potential barrier between the two bodies becomes larger than the binding energy of the valence electrons.

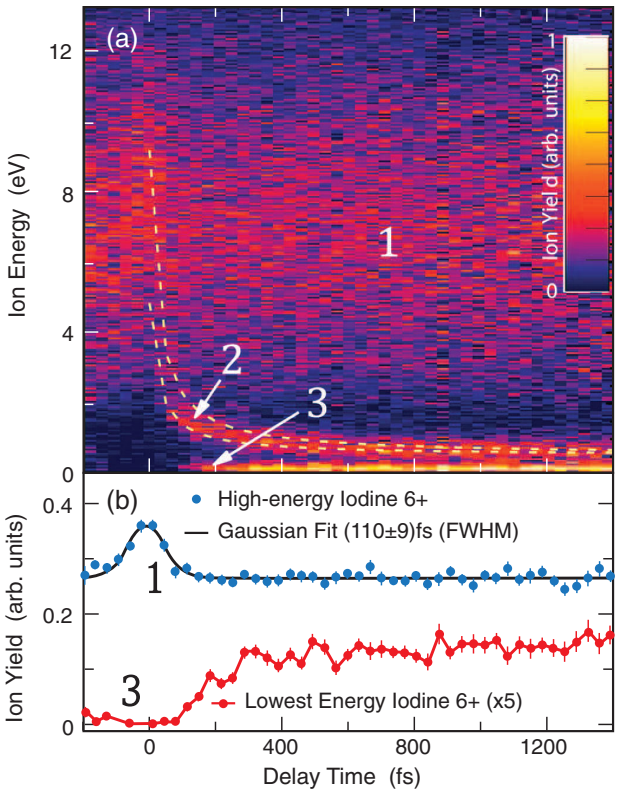

FIG. 13. Time-resolved fragmentation of CH_3I. (a) Map of the delay-dependent kinetic-energy distribution of I^{6+} ions following near-infrared dissociation and x-ray ionization of iodomethane. Channel 1 stems from x-ray induced dissociation of the bound molecules, channel 2 from Coulomb explosion of charged fragments, and channel 3 from x-ray ionization of the CH_3I^+ dissociative channel. (b) Delay-dependent yields of channels 1 and 3. Channel 3 appears only when charge-transfer processes between the iodine and methyl fragments are effectively suppressed in the dissociating molecule. Adapted from Erk *et al.*, 2014.

X-ray FELs are also a promising tool for following photo-induced dynamics. Often such photochemical reactions follow pathways violating the Born-Oppenheimer approximation, meaning that the electronic and nuclear degrees of freedom cannot be decoupled. These so-called non-Born-Oppenheimer transitions proceed on ultrafast time scales and prominently occur on conical intersections (Yarkony, 1996). Ultrafast optical-laser pulses are commonly used to investigate photochemical reactions, but they mostly probe transitions between delocalized valence electrons. At LCLS, Auger spectroscopy was employed to disentangle the ultrafast motion of electrons and nuclei in photoexcited nucleobase thymine (McFarland *et al.*, 2014). Ultrafast Auger spectroscopy has a few advantages over other spectroscopic approaches: The Auger electron kinetic energies yield element- and site-specific information and they are sensitive to both the nuclear and electronic dynamics in the molecule. An additional technical advantage is that the Auger spectra are not sensitive to the bandwidth and energy jitter of the incoming photon pulses, making this the technique of choice for fluctuating SASE sources (Sec. II). From time-dependent Auger yield maps, it was possible to infer that in photoexcited thymine first the C-O bond stretches in the photoexcited $\pi\pi^*$ state, followed by a electronic relaxation into the $n\pi$ state on the 200 fs time scale (McFarland *et al.*, 2014). This experiment demonstrates that time-dependent Auger maps are well suited for distinguishing between ultrafast nuclear and electronic relaxation in photochemical reactions with high local sensitivity.

c. Ultradilute systems

The time structure of LCLS can also be exploited for studying ultradilute systems, providing the opportunity to investigate thin targets with coincidence techniques. These techniques dramatically increase the signal-to-noise level compared to measurements with quasicontinuous synchrotron sources. This approach was used to study the oscillator strength of highly charged iron ions (Bernitt *et al.*, 2012). Fe^{16+}, also referred to as Fe XVII, produces some of the brightest emission lines from hot astrophysical objects, but it is poorly fitted in the astrophysical models. The experiment sought to resolve whether the discrepancy comes from incomplete modeling of the plasma environment or shortcomings in the treatment of the atomic wave functions.

To measure the atomic oscillator strength of Fe XVII with high precision, an electron beam ion trap (EBIT) was set up and fluorescence yield spectra were recorded with monochromatized x-ray pulses (Bernitt *et al.*, 2012). In the EBIT, an electron beam impact ionizes Fe atoms and the created ions are simultaneously trapped. The trapped ions form a cloud that is approximately 50 mm long and 500 μm wide, with an areal density of only 10^{10} ions per cm^2. A high-purity Ge detector is used to detect fluorescence photons. The signal-to-noise increase comes through gating the detector readout to the time window in which the x-ray induced fluorescence photons are created, as demonstrated in Fig. 14. The fluorescence decay times are below picoseconds and the detector response time is on the order of 180 ns. With this coincidence approach, the signal level was increased by a factor of 14 000 over the background signal produced by the interaction of the intense electron beam with the target ions. The experiment revealed that Fe XVII exhibits an unexpectedly low oscillator strength, which primarily indicates that the atomic wave functions need to be refined for a more accurate description of astrophysical emission lines.

3. Multicolor and nonlinear experiments

The unprecedented intensities available at LCLS allow an extension of the concepts of nonlinear optics to the x-ray spectral regime. So far experiments have employed both x-ray–optical and x-ray–x-ray schemes, enabling new experimental possibilities.

a. Sidebands and streaking

Photoelectrons and Auger electrons generated in the presence of an optical-laser field can exchange photons with the field. These spectra, often referred to as "dressed" spectra, exhibit distinct characteristics that sensitively depend on the optical-laser parameters. In general, two cases can be distinguished (see Fig. 15) that are defined by the ratio of the

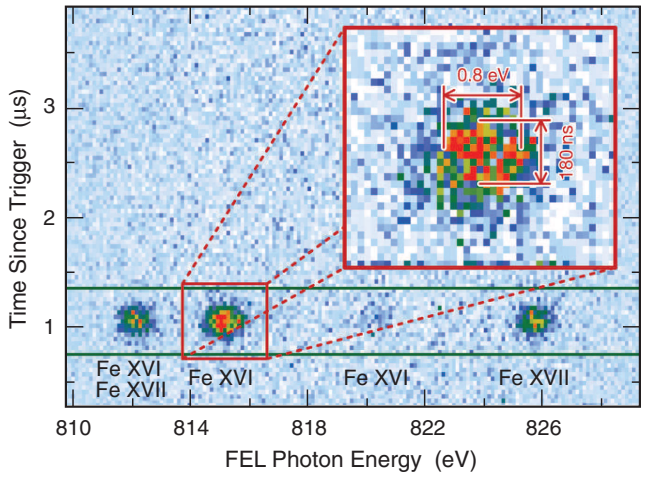

FIG. 14. Time-coincidence map between x-ray pulses and detected fluorescence from Fe XVII in an electron beam ion trap. The x-ray induced fluorescence is measured in a small time window determined only by the time resolution of the Ge detector. Gating on the x-ray time window increases the ratio of signal-to-electron-beam induced background by a factor of 14 000 allowing one to obtain high-quality spectra from ultradilute systems. From Bernitt *et al.*, 2012.

dressing field period to the duration of the x-ray pulse ionizing the spectra.

For periods of the dressing field shorter than the x-ray pulse, additional lines can be observed. These so-called sidebands are separated from the main photoelectron or Auger line by multiples of $\hbar\omega_{\text{optical}}$ [Fig. 15(a)]. Sidebands are symmetrically distributed on both sides of the main line and are sensitive to the contributions of more than one optical period, and thus depend on the cycle-averaged intensity envelope of the dressing field. Sidebands were used early on at LCLS to characterize the mean temporal jitter between the x ray and external optical laser, and to measure the duration of few-tens-of-femtosecond x-ray pulses through

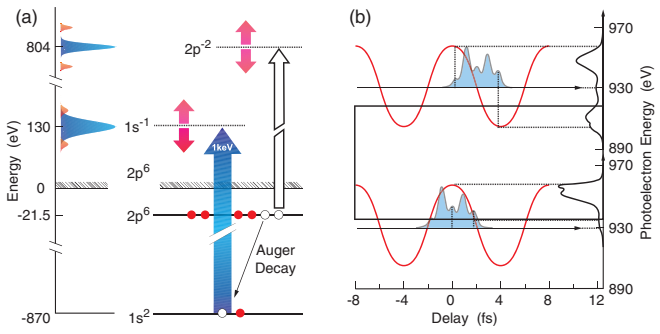

FIG. 15. Comparison of (a) sideband generation and (b) streaking in mixed optical and x-ray laser fields. Sidebands are symmetrically distributed around the main line and they reflect the exchange of photons from both fields during more than one optical period. In streaking experiments (b) the photoelectrons experience a redistribution of kinetic energy that depends on the magnitude of the electric field at the instance of their generation during a subcycle of the optical-laser field. Adapted from Düsterer *et al.*, 2011, and Helml *et al.*, 2014.

x-ray-optical cross correlations (Düsterer *et al.*, 2011). In a following study, the angular dependences of laser-assisted Auger decay were investigated (Meyer *et al.*, 2012). The spectra depend strongly on the emission angle of the electrons and exhibit a strong intensity variation. This variation is caused by the interference of Auger electrons emitted at different times within one optical cycle of the dressing laser, allowing one to probe the dynamics of the Auger process with external optical-laser fields.

In the second case, the x-ray pulses are shorter than the period of the dressing field, which is the so-called streaking regime [Fig. 15(b)]. The photoelectrons generated at different delays between the x ray and external laser field, i.e., at different locations on the electric-field ramp of the external laser, experience a redistribution in energy that depends on the magnitude of the electric field at the instant of their generation. The resulting electron kinetic-energy spectrum is typically broadened and shifted compared to the unstreaked spectrum. Streaking spectroscopy was employed to measure the temporal structure and duration of single ultrashort x-ray pulses down to a few-femtosecond pulse length (Helml *et al.*, 2014). This method is noninvasive to the x-ray beam and exhibits femtosecond resolution, potentially providing complete information about the x-ray pulses on a shot-by-shot basis, transparent to the main experiment.

b. X-ray and optical wave mixing

Another example of extending nonlinear optics into the x-ray regime is x-ray and optical mixing, also referred to as sum frequency generation or optically modulated x-ray diffraction. This process was initially proposed in the 1970s (Freund and Levine, 1970; Eisenberger and McCall, 1971), but could be demonstrated only recently at LCLS (Glover *et al.*, 2012) because extremely bright x-ray sources are needed for such experiments.

X-ray diffraction is a powerful tool for the determination of structure and composition of matter, where hard x-ray photons probe the overall electron distribution and the overall scattering signal is dominated by the large number of core electrons highly localized to the atomic sites. The valence electrons, determining the material's chemical and structural properties, contribute only weakly to the scattering process and so other tools are required to access this information. Sum frequency generation opens a pathway to selectively probe the structure of the valence electrons. An external optical laser modulates the valence electrons and some of the oscillating energy is transferred to the x-ray energy in the scattering process. As a result, the x rays scattered by the valence electrons have a higher energy, equal to the sum of both frequencies according to $\vec{G} = \vec{k}_{\text{scatter}} - (\vec{k}_{\text{xray}} + \vec{k}_{\text{optical}})$ (compare also the schematic in Fig. 16). In principle, all electronic levels can be probed with sum frequency generations as long as the driving light frequency is resonant with the electron binding energies, e.g., deeper valence levels can be probed with extreme ultraviolet light.

X-ray and optical light mixing was first demonstrated in a diamond crystal (Glover *et al.*, 2012). Diamond was chosen as a test sample because its electronic and geometric structure are well known. A monochromatized x-ray pulse with a photon

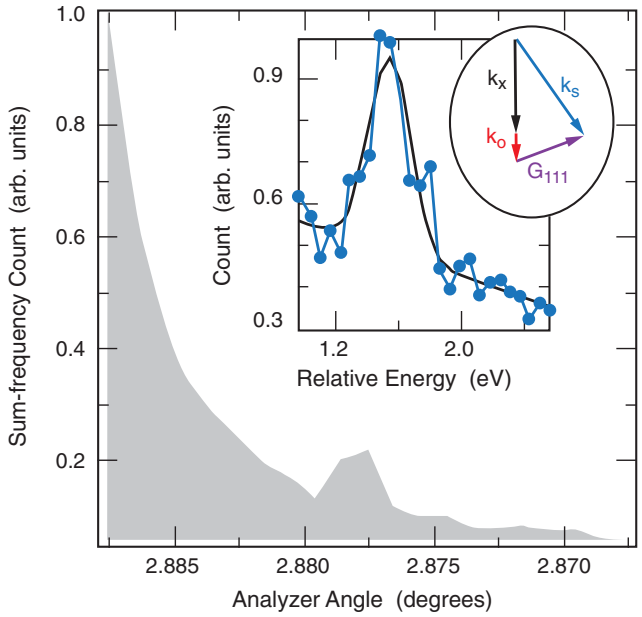

FIG. 16. X-ray and optical wave mixing signal. The additional peak at 2.878° on the sloping background of the main peak stems from sum frequency generation of the x ray and optical pulse. The inset shows the spectral analysis of this peak, confirming that the energy of these photons equaled the sum of the incoming x-ray and optical photon frequencies. Adapted from Glover *et al.*, 2012.

energy of 8 keV and length of 80 fs, as well as an optical pulse with a photon energy of 1.55 eV and a pulse length of 2 ps, simultaneously illuminated the sample. A sum frequency signal, the peak at 2.878° on the sloping background of the main peak in Fig. 16, could be detected at the expected sample and analyzer angles. Spectral analysis of this peak confirmed that the energy of these photons equaled the sum of the incoming x-ray and optical photon frequencies (cf. the inset in Fig. 16). The conversion efficiency in this experiment was only on the order of 10^{-7}, but still around 4000 photons could be detected per second.

c. Anomalous nonlinear x-ray Compton scattering

Nonlinear Compton scattering of two identical hard x-ray photons producing a single higher-energy photon, a fundamental nonlinear process, was recently demonstrated by focusing the full power of LCLS into a solid beryllium target (Fuchs *et al.*, 2015). The x-ray intensity reached 10^{20} W cm^{-2}, which corresponds to an electric field of within almost 4 orders of magnitude of the Schwinger quantum electrodynamic limit. Nonetheless, because of the high frequency of the hard x rays, the interaction is well below the relativistic regime in which electrons are accelerated to near the speed of light within a half period of the x-ray field. This means that the probability of two photons scattering simultaneously from a single electron in any given atom is negligible, but the use of a high target density and a clever experimental setup allowed researchers to identify the nonlinear processes. They compared the scattering response from two simultaneously illuminated, identical targets, which were placed in and out of focus. The scattered radiation was detected with an array of 2D detectors, covering a wide solid angle. Each x-ray shot was recorded separately and the overall signal was averaged over 170 000 shots. Varying the pulse energy revealed a quadratic dependence of the higher-energy Compton signal with the incoming FEL intensity, characteristic for a second-order nonlinear process.

Remarkably, the spectra of the high-energy Compton peaks are substantially broadened and redshifted well beyond expectations for the nonlinear Compton shift using the common free-electron approximation for ground-state electrons. These results suggest a novel scattering mechanism with more significance on the bound state of the electrons, indicating that nonlinear interactions in the hard x-ray regime must be rather rich and more complicated than expected.

d. Stimulated emission processes

LCLS opened the door for stimulated processes in the x-ray spectral regime (see Sec. III.B.2). Examples range from evidence for Rabi cycling in the $1s$-$2p$ inner-shell resonance in singly ionized neon through changes of the Auger-decay channel line shape (Kanter *et al.*, 2011) to an x-ray-FEL-pumped x-ray laser in a dense neon target (Rohringer *et al.*, 2012) and strong stimulated inelastic x-ray scattering (Weninger *et al.*, 2013).

For the x-ray-pumped x-ray laser, first envisioned in the 1960s (Duguay and Rentzepis, 1967), intense x-ray pulses with a photon energy of 960 eV, clearly above the neon K-shell ionization threshold, were focused into a dense neon gas target (Rohringer *et al.*, 2012). The x-ray pulse created a population inversion along the x-ray beam with a plasma channel of inner-shell excited neon atoms. The inner-shell vacancies decay mostly via Auger processes but there is a 1.8% probability for spontaneous radiative decay with a photon energy of 849 eV. Photons that are spontaneously emitted toward the front of the plasma channel can be exponentially amplified along the channel. The lasing line was monitored with a grating spectrometer. Varying the incoming x-ray pulse energy clearly showed an exponential-gain curve. Doubling the pulse energy on the target from 0.12 to 0.24 mJ increased the lasing-line intensity by 4 orders of magnitude. Three examples of the lasing line itself are shown in Fig. 17. The lasing line is very narrow with a Lorentzian line shape and width of only 0.27 eV. The line width is primarily determined by the core-level lifetime. This is much narrower than can be achieved in plasma-based x-ray lasers because in this experiment the gas density is low and the gas itself is relatively cold; therefore, Doppler and collisional broadening effects are virtually absent. Furthermore, the lasing line is jitter free (Fig. 17), demonstrating how this process can convert a fluctuating SASE source into a highly stable, coherent, narrow-bandwidth x-ray source (Rohringer *et al.*, 2012).

In a conceptually similar experiment, a stimulated x-ray Raman signal was observed, but in this case the photon energy was varied across the K-edge ionization threshold of 870 eV (Weninger *et al.*, 2013). For the photon energies below the K edge, neutral atoms are core excited by resonant ionization of the $1s$ levels, and a transient population inversion between

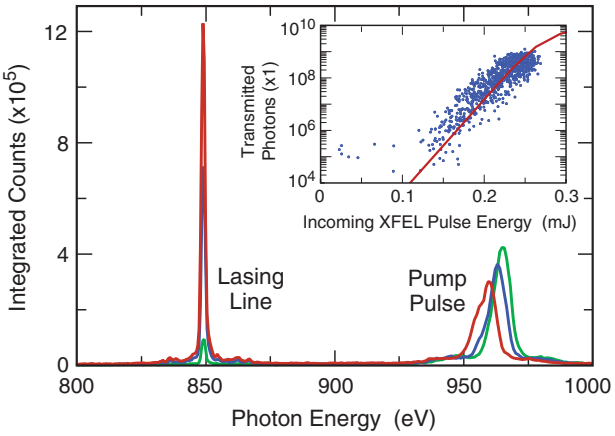

FIG. 17. X-ray pumped x-ray lasing. Selected single-shot spectra of the neon x-ray lasing line at 850 eV and simultaneously transmitted FEL pulse around 960 eV. The x-ray lasing line width is much narrower and jitter free. Note that the FEL pulse is attenuated by the neon gas by about 3 orders of magnitude compared to the incoming pulse energy. The inset displays the exponential gain with increasing pump power. Adapted from Rohringer *et al.*, 2012.

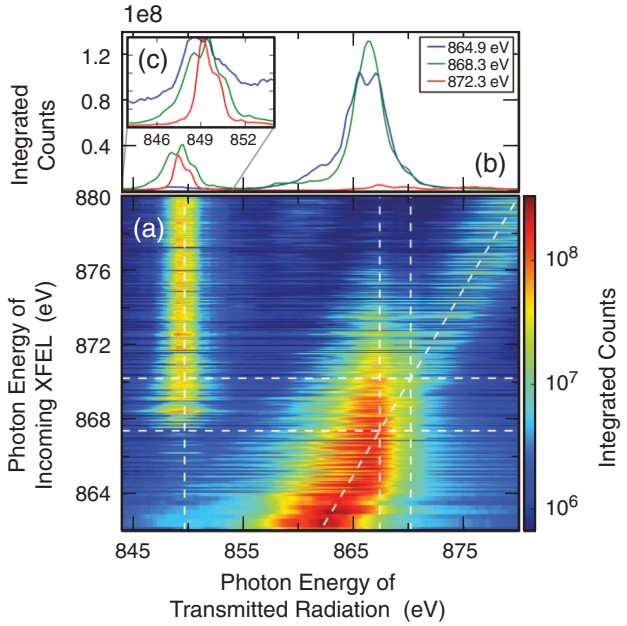

FIG. 18. Measured single-shot emission spectra as a function of the (a) incoming photon energy and three distinct line-outs with (b) as-measured and (c) normalized intensities. The x-ray FEL pulses appear as a diagonal line in (a) which is heavily attenuated for photon energies above the Ne *K* edge at 870 eV. The dominant emission line appears at 850 eV. Below 867.5 eV excitation energy the emission is absent and above 870 eV the line is stable. For the intermediate emission energy regime, the line profile and peak position vary strongly, owing to stimulated electronic x-ray Raman processes. Adapted from Weninger *et al.*, 2013.

the 1*s* and valence shell is achieved. Again, the Auger processes dominate the core-hole decay, but a small probability of radiative decay can lead to an avalanche of stimulated scattering events, which results in exponential amplification of the Raman signal. Analysis of the Raman signal from a fluctuating SASE source is difficult, but a detailed look at the line shapes of the emission signal showed that a Raman signal was observed. In Fig. 18, the single-shot spectra as a function of the incoming photon energy and three distinct lineouts are shown. The FEL pulses can be identified as the diagonal line, which is heavily attenuated as soon as it hits the *K*-edge ionization threshold at 870 eV. The emission line of the dominant 1*s*-2*p* emission is visible at 850 eV. For photon energies below 867 eV, i.e., below the lowest Rydberg state, the emission is absent and for photon energies above 870 eV, the emission is very narrow and stable in energy. In the intermediate regime, the peak position and line profile vary strongly, with a stochastic shift of a few hundred meV, broadening, and multipeak structure. These features can be linked to stochastic detuning of the multiple spectral spikes of the SASE pulses and are strong experimental evidence for stimulated electronic x-ray Raman scattering (Weninger *et al.*, 2013). Ideally such experiments would be performed with narrow-bandwidth, tunable, two-color x-ray sources so that one color could excite an inner-shell transition and the second color could deexcite the electron into the short-lived core hole.

4. New possibilities from imaging

The intense x-ray pulses from free-electron lasers allow diffractive imaging of single, nanometer-sized particles or molecular ensembles in a single shot (see Sec. III.B.1). This approach can be used not only to image biological specimens (see Sec. IV.E.5), but also to gain information about the morphology of samples in the gas phase (Bostedt *et al.*, 2010; Loh *et al.*, 2012) or even to investigate their nonlinear scattering response (Bostedt *et al.*, 2012). Imaging also enables completely new experimental strategies in AMO physics.

a. New insights from coincident imaging and spectroscopy

Many physical processes depend on a single relevant parameter that is often lost during ensemble averaging experiments. Intense LCLS pulses offer the opportunity to develop new experimental strategies for retrieving additional information from single-shot experiments. Single-shot imaging and spectroscopy were combined into a coincidence experiment on single particles in order to gain additional information about the interaction of highly intense x-ray pulses with nanometer-sized samples (Gorkhover *et al.*, 2012). The coherent images of single clusters were used to deconvolute their size distribution and to determine their exposure intensity, i.e., location in the focal volume. The coincident ion time-of-flight spectra shown in Fig. 19 yielded unprecedented insight into the fragmentation dynamics of the clusters exposed to defined power densities. The stochastic sampling of the focal volume distribution with the single clusters showed that within 2 orders of magnitude of power density, the nanoplasma properties changed from a low-temperature plasma, where recombination dominates, to a hot nanoplasma, where recombination is efficiently suppressed and high-charge states prevail (top panel in Fig. 19). In the lower panel of Fig. 19, the focal volume averaged spectra are shown to be

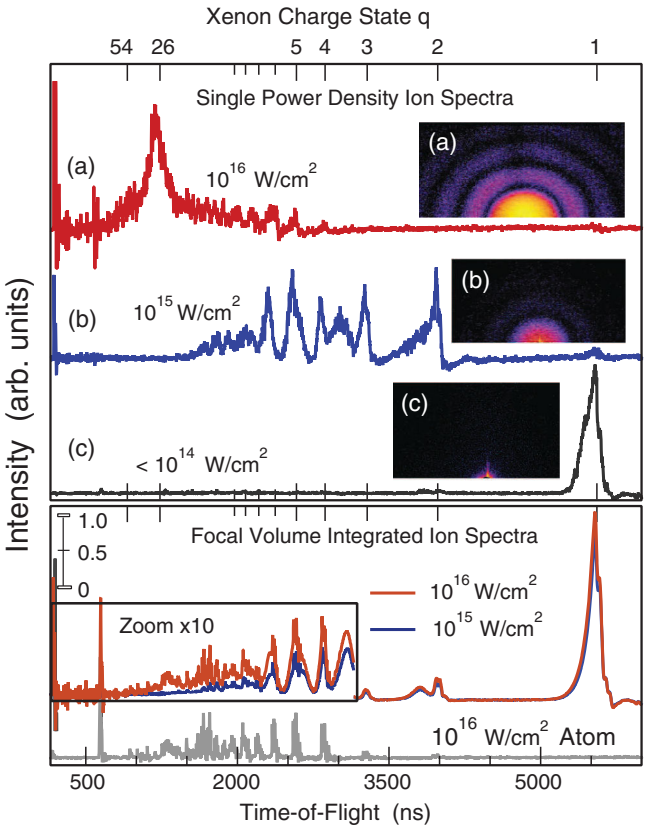

FIG. 19. Single-shot ion time-of-flight spectra of clusters irradiated with intense x-ray pulses, taken in coincidence with their diffraction image. In the three representative shots the clusters were located in the (a) center or (c) outer wings of the focus or (b) in between. The ionization dynamics depend strongly on the exposure intensity. The focal volume averaged data (bottom) are dominated by the low-intensity signal in the outer wings of the focus. Adapted from Gorkhover *et al.*, 2012.

dominated by the sample interacting with the least-intensity regions of the x-ray spot.

Simultaneous imaging and spectroscopy were also incorporated to monitor the radiation damage during structure determination (Sec. IV.E.1). It is noteworthy that in these experiments (Kern *et al.*, 2013) the samples were of a size comparable to the focal diameter, and thus focal volume dependent effects are averaged out.

b. Controlled-molecule imaging experiments

One of the grand visions for free-electron laser sources is the ability to use intense x-ray pulses for structure determination of large and complex molecules in a single-molecule single-shot approach (Sec. IV.E.5). For small molecules, however, an alternative approach of imaging controlled ensembles of molecules may be equally viable. Such experiments would allow the use of less intensely focused x-ray pulses and provide a much lower x-ray dose per atom, circumventing radiation damage. In other words, they take advantage of the short pulse length and not the peak intensity of free-electron laser pulses. The feasibility of this approach was demonstrated by recording x-ray diffraction patterns of quantum-state-selected and strongly aligned 2,5-diiodobenzonitrile molecules (Küpper *et al.*, 2014). This study is the first step toward using x-ray diffractive imaging for investigating ultrafast dynamics in the gas phase with few-femtosecond time resolution. In a subsequent study the prototypical ring-opening reaction in 1,3-cyclohexadiene was followed with diffuse x-ray scattering in combination with simulated diffraction patterns of possible reaction pathways [(Minitti *et al.*, 2015a), see also Sec. IV.D.1.c]. Imaging controlled-molecule ensembles is a promising experimental approach for the upcoming high-repetition-rate free-electron lasers (Sec. V).

c. Imaging quantum phenomena on the nanoscale

Superfluid helium is a quantum mechanical state that extends over macroscopic length scales, much like Bose-Einstein condensates and superconductors. In a superfluid finite droplet, any rotational motion must manifest itself through the formation of vortices. Such vortices have been observed in macroscopic volumes of rotating ^{4}He but insight into superfluid rotational motion on the nanoscale remains elusive.

Single-shot coherent diffractive imaging was used to investigate nanometer-sized superfluid ^{4}He droplets (Gomez *et al.*, 2014). The droplets were formed via expansion of high-purity helium through a 5 μm diameter nozzle at a temperature of 5 K. When passing through the vacuum, the droplet temperature was further reduced below the superfluid transition at 2.17 K by evaporative cooling. The droplets were imaged with a single, intense x-ray pulse. Many of the coherent diffraction images exhibited strong distortions from the spherical symmetry. In the most extreme cases sharp streaks from nearly parallel particle surfaces were observed, indicating "wheel-shaped" particles. From the observed large, centrifugal shape deformations it could be concluded that the droplets spin with rotational velocities beyond the stability limit of viscous classical droplets. In a second step of the experiment, the helium nanodroplets were doped with xenon atoms in a pickup cell. The xenon atoms gather along the vortex cores and act as an x-ray contrast agent due to their higher scattering cross section. In this way, the quantum vortices can be directly imaged. The scattering pattern from the doped ^{4}He droplets showed distinct Bragg peaks in addition to the characteristic pattern of the droplet (see Fig. 20). This Bragg pattern from the xenon clusters trapped

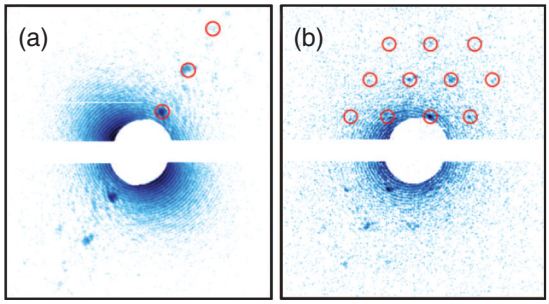

FIG. 20. Single-shot diffraction images (in logarithmic scale) from superfluid helium droplets doped with xenon atoms. The xenon atoms gather at the quantum vortices in the superfluid droplets, giving rise to Bragg peaks. The data suggest that the quantum vortices organize in a regular lattice with high densities. From Gomez *et al.*, 2014.

at the vortex cores showed that the quantum vortices form a lattice inside the droplets with densities up to 5 orders of magnitude higher than in bulk liquid helium.

5. Perspectives

Over the past five years AMO physics at LCLS rapidly developed from fundamental experiments about the interaction of intense x-ray pulses with atoms, molecules, and clusters to using the ultrafast x-ray source for pump-probe-type spectroscopy applications.

First steps have been taken in the direction of nonlinear x-ray physics. Combining the emergence of new FEL sources with decades of experience with optical lasers, it can be easily envisioned that this will become a major area in the future, enabling ample new experimental possibilities. Further, increased longitudinal coherence from future sources will enable exploration of quantum control of inner-shell processes.

Considering the body of work described in this section, a number of conclusions may be drawn regarding the impact of AMO studies on spectroscopic and imaging techniques. First, it is clear that the reduction of the FEL pulse length, as discussed in Sec. II.B, enables the enhancement of spectral signatures in new electron spectroscopy applications described in Sec. IV.A.1.b. Second, sum frequency generation allows selective measurement of a diffraction signal from specific electronic levels, as discussed in Sec. IV.A.3.b. This approach opens the door to investigations of the evolution of valence charges with atomic-scale resolution, yielding insight into chemical reactions, phase transitions, or into light-induced charge redistribution. Third, stimulated x-ray Raman scattering described in Sec. IV.A.3.d is a new way to probe electronic structure. Continuous improvements of current and future FELs will make stimulated electronic x-ray Raman scattering a routine tool for electronic structure investigations (Sec. V.B).

Imaging applications have merged into AMO physics and have already proven their potential impact in areas as diverse as nanoplasma formation and chemical dynamics, as well as providing new insights into quantum phenomena as described in Sec. IV.A.4. Similarly, results from fundamental AMO physics can guide other FEL-based applications. As discussed in Sec. IV.A.1.c, the results of experiments concerned with x-ray induced transparency have direct implications for ultrafast x-ray scattering experiments (Sec. IV.E.1). Heavy atoms, in particular, Se, are often embedded in biomolecules in order to get phase information. It can be expected that these heavy atom centers serve as ionization hot spots as described in Sec. IV.A.1.d, leading to significant local radiation damage. For coincident imaging and structure determination, as discussed in Sec. IV.A.4.a, pump-probe experiments offer a great opportunity; their spectroscopic data yield information about the reaction state, while scattering information determines the corresponding structure of the molecule.

All these examples underline the fact that LCLS has opened new pathways for investigating diverse problems in the field of AMO sciences, and that this is only the beginning of an exciting new era in x-ray physics. As these intense interactions and nonlinear techniques are being better understood and established, the next phase where they have been applied is across the various disciplines to be discussed in the next sections starting with condensed matter.

B. Condensed matter physics

In condensed matter and materials physics studies, one frequently seeks to understand the behavior of a material in the context of electronic and atomic interactions on femtosecond time scales with atomic resolution. In this section, a few examples are presented that demonstrate the benefit that arises from studies leveraging the unique properties of an x-ray FEL source across a wide range of materials applications. Beginning with strongly correlated systems, it is shown that subpicosecond probes provide important insight into the relationship between different types of ordering in these systems and functionality, such as the onset of superconductivity. By combining the ultrafast probe with an optical-laser pump, the nonequilibrium behavior of excited systems can be elucidated, from multiferroic crystals to thin film heterostructures and interfaces. If one also exploits the highly transversely coherent nature of the source, coherent imaging can be used to see magnetic domains and observe phonons in a solid.

1. Strongly correlated systems

In strongly correlated systems, interactions between electrons are such that the quantum effects cannot be properly treated using classical theory. Measurements made at LCLS using ultrashort pulses have greatly added to our understanding of this broad class of systems by allowing observation of competing interactions on short time scales, and the ability to obtain atomic-level information of short-lived intermediate states. This new capability has brought fresh insight into one of the broadest fields in condensed matter physics.

a. High-temperature superconductivity

High-temperature superconductivity is one of the celebrated examples of a strongly correlated material where the transport cannot be adequately described due to incomplete understanding of the electron-electron interactions. Some of the most notable achievements using LCLS in these materials involve measurement of different types of order that either compel or compete with superconductivity, such as magnetic excitations and charge-density waves.

Cupric oxide, the building block for high-temperature superconducting cuprates, displays a spin-spiral phase that can lead to an incommensurate magnetic ordering displaying a ferroelectric moment (Kimura *et al.*, 2008). To measure the magnetic ordering directly through resonant diffraction, an optical excitation was used to excite the system above the band gap and study the effects on that magnetic order. The time it takes for the phase transition to occur from a low-temperature collinear, antiferromagnetic state into the spiral magnetic state was quantified (Johnson *et al.*, 2012). The time for this phase change is 2 ps for low pump fluence, and it decreases with increasing pump fluence until saturating at 400 fs. This implies that there exists a "speed limit" for optical methods to induce magnetic switching. By measuring the magnetic peak as a function of photon energy, resonant

scattering spectra were compared to band structure calculations using finite-temperature DFT. It was found that even when the electron temperature was raised considerably above the antiferromagnetic transition temperature, or Néel temperature, magnetic order persists for hundreds of femtoseconds after the excitation (Staub *et al.*, 2014), demonstrating that magnetic ordering can transiently exist even under highly elevated temperatures.

Using optical sources, it has been possible to observe light-induced superconductivity in a stripe-ordered cuprate system (Fausti *et al.*, 2011); however, LCLS has allowed direct measurement of the charge-stripe structure during the onset of superconductivity. A midinfrared pump was combined with the x-ray pulses from LCLS to measure the charge-stripe destruction in $La_{2-x}Ba_xCuO_4$ for $x = 1/8$ doping, and it was found that the relevant time scale was subpicosecond (Först *et al.*, 2014b). This exactly matched the time scale for superconductivity to be induced in a closely related system, providing strong evidence of a long-held belief that charge stripes directly compete with superconductivity. In addition, it was discovered that the lattice changes on a much slower time scale, on the order of 15 ps. This additional information was particularly interesting because the charge ordering had previously been associated with the low-temperature, tetragonal-structural phase transformation. These measurements have given evidence that these two mechanisms can be unraveled by time-domain studies, and that charge ordering was directly responsible for hindering superconductivity.

The high-temperature superconductor $YBa_2Cu_3O_{6+\delta}$ (YBCO), a bilayered copper-oxygen plane system, is of interest due to the recent discovery of the existence of a charge-density wave (CDW) in the bulk (Ghiringhelli *et al.*, 2012). The behavior of YBCO poses two interesting questions: (1) What is the nature of the transient state that allows coherent interlayer transport above its critical temperature (Hu *et al.*, 2014)? (2) What is the interrelationship between the CDW and the onset of superconductivity (Chang *et al.*, 2012; Dakovski, Lee *et al.*, 2015)? By combining femtosecond x-ray diffraction with first-principles DFT calculations in the local-density approximation, the crystal structure of this transient state has been observed. Starting in a normal state of the material, a midinfrared pump laser pulse was used to induce nonlinear lattice excitation and to drive the new superconductinglike state, while studying the Bragg reflections as a function of time (Mankowsky *et al.*, 2014). Figure 21 shows the time trace of four Bragg reflections, two increasing and two decreasing after excitation, and their fits from the DFT calculations. Out of the 33 Raman active modes known to exist, only 11 preserve the symmetry of the unit cell. Computing all 11 modes (red curves) was shown to be similar to the case of using only the four specific phonon modes, the A_g modes (green curves), that couple most strongly to the optical-laser-driven mode, B_{1u}. These data, combined with theory describing this transient state, show that the Cu atoms within the bilayer are driven away from each other, while being driven toward each other between different bilayers. Additionally, a small amount of buckling of the O-Cu-O bonds was measured.

Resonant scattering was also used to study the in-plane ordering of the CDW to complement the time-resolved

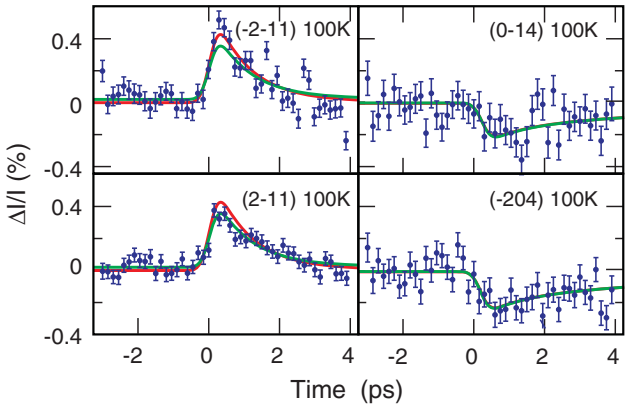

FIG. 21. Nonlinear lattice dynamics. Time-dependent Bragg reflections for four peaks in YBCO. The displacive distortion of the lattice shows a decrease in two peaks while the intensity increases in the other two. The data are for the x-ray diffraction pump-probe experiment, while the fitted curves are for the DFT with local-density approximation (LDA) theory. The green shows calculations of all 11 A_g phonon modes, while the red shows the most important four: Those that couple most strongly to the optically driven, B_{1u} mode. From Mankowsky *et al.*, 2014.

structural measurements of YBCO by using the Cu L-edge resonance, where direct sensitivity to the CDW can be monitored during the nonlinear excitation used to induce the transient state. It was found that 50% of the CDW state vanished on the same time scale as the appearance of the Josephson plasma edge (Först *et al.*, 2014a), the feature from time-resolved optical spectroscopy that is the signature of the superconducting state (Fausti *et al.*, 2011). The melting of charge order and the entry into the transient state both occur on sub-ps time scales, yet the depleted CDW state lasts much longer than the ~6 ps duration of the plasma edge. This correlation implies that the two are strongly competing mechanisms, but that the CDW state takes longer to reform long-range order (Först *et al.*, 2014a).

b. Magnetic oxides

From testing many-body theory to supporting development of next-generation devices, studies of magnetic oxides have found an enabling technology at LCLS. For example, by optically pumping both a charge- and a magnetically ordered stripe state of nickel oxide, it was found that the robustness of certain types of order implied by the thermodynamic transition temperatures could interchange when the sample is out of equilibrium, an effect that is observed only on ultrafast time scales (Chuang *et al.*, 2013). This is not observed in equilibrium measurements because in the nickelate phase diagram, the charge ordering always has a higher ordering temperature, and hence is more robust to thermal fluctuations. Surprisingly, the two different order parameters both decay abruptly and start to recover at a rate of a few picoseconds, but the longer-term recovery differs by an order of magnitude. To determine if the longer recovery of the magnetic state was related to lattice dynamics, time-resolved measurements were also made of the structural Bragg peak, but it was found that no lattice recovery dynamics occurred in the 25 ps window of

the measured magnetic metastable state. To understand this, a Gross-Pitaevskii time-dependent Ginzburg-Landau theory was used to calculate the material response for this system. The calculations could reproduce both sets of dynamics of each superstructure order with a reasonable spin order–charge order coupling parameter together with the metastable magnetic state (Chuang *et al.*, 2013).

The quantum many-body physics was studied further by combining the LCLS measurements with optical reflectivity data, where dynamics of the charge order could be compared to short-range-order electronic effects. It was found that optical measurements also showed two time scales, hundreds of femtoseconds, and a few picoseconds, but that all the data combined from the two methods yielded universal time scales as a function of optical pump fluence. This discovery of three underlying time scales could explain all the responses of both order parameters at different temperatures using the two methods (W. S. Lee *et al.*, 2012). These distinct time scales were subpicosecond, few picoseconds, and tens of picoseconds, describing the electron-phonon, amplitude-phonon, and phason-phonon coupling times. Most surprising was the longest time scale, the coupling that was shown to be due to "phasons"—excitations of the charge-ordered density modulation which decay in about 15 ps—and whose interpretation is consistent with the fact that the fluence dependence found for this coupling was the most sensitive to pulse energy.

Furthermore, one of the oldest known magnetic oxides Fe_3O_4 has been studied using a combination of ultrafast optical techniques commonly employed at LCLS, potentially leading to new technologies. The metal-insulator transition in magnetite represents a model system for understanding the nature of the metal-to-insulator transition, thought to be due to units described as "trimerons," three-iron atom lattice distortions (Senn, Wright, and Attfield, 2012). The electronic ordering and atomic structure were studied as a function of pump fluence and found to collapse onto a single, universal plot (de Jong *et al.*, 2013). Electronic ordering, which is observed as a superlattice, can be destroyed temporarily by an optical pulse, but it was found that only with a fluence of 1.3 mJ cm^{-2} or greater does the system undergo the transition to a metal. At or above this fluence, the long-range structure is partially destroyed, separating into small islands. These islands of electronic ordering are separated by a transient metallic phase, allowing percolation to take place along the conductive pathways between regions. The distinction between partially destroying the order and disrupting the network sufficiently to create a metal was discovered by measuring four parameters using ultrafast methods: three from x-ray diffraction at LCLS and one from optical reflectivity.

The trimeron lattice is destroyed rapidly within the time resolution of the experiment, approximately 300 fs; the intensity is represented by the brown dashed line in Fig. 22. This is followed by a slower, picosecond process. This process is elucidated by the fact that three distinct observations all occur on the same time scale of about 1.5 ps: The trimeron-order coherence length shortens, the lattice structure changes, and the metallic content of the phase increases. These parameters are found to all agree by analyzing the width of the resonant diffraction peak (green squares), the change in diffraction angle (blue diamonds), and the increase of the optical reflectivity data $\Delta R/R$ (red curve), respectively; all fall on a universal curve shown in Fig. 22.

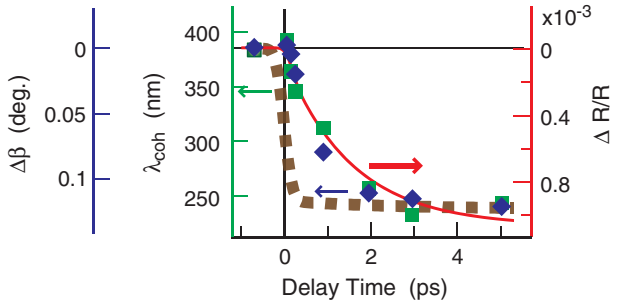

FIG. 22. Universal curve showing the speed of the metal-to-insulator transition in magnetite. X-ray data (blue and green symbols and brown dashed line) taken at the $(0, 0, 1/2)$ reflection (Fe L_3 edge) shown together with the optical reflectivity (red line, representing an exponential fit to the data). The reduction in the electronic ordering coherence length (λ_{coh}, green squares) and the change in diffraction angle ($\Delta\beta$, blue diamonds) occur concomitantly with the increase of the optical reflectivity ($\Delta R/R$, red curve) with a time constant of 1.5 ± 0.2 ps. This decay occurs with a delayed onset as clearly indicated by the unchanged λ_{coh} and $\Delta\beta$ values at 200 fs time delay and reflects the structural modifications toward the cubic lattice where metallic charge fluctuations reduce the coherence of the remnant patches of electronic order. For comparison, the trimeron lattice diffraction intensity vs time (brown dashed line) shows a fast quench, reflecting the time resolution of the experiment. From de Jong *et al.*, 2013.

The picosecond process is correlated with the actual occurrence of the metal-insulator transition and occurs only when the fluence is above a 1.3 mJ cm^{-2} threshold. In this case, not only does the trimeron lattice get destroyed, but the low-temperature insulating phase also breaks up into short-range ordered domains. This functionality of the material was deciphered only by combining different types of ultrafast measurements. This demonstrates that not only can a fundamental question such as the nature of the metal-to-insulator transition be understood, but progress in technology can be gained as well. In measuring the speed limit of the change of state, it was found that the switching in this system outperforms the best graphene transistors reported so far by an order of magnitude (Wu *et al.*, 2011).

c. Complexity

Spontaneous formation of nanostructure in condensed matter is fundamental to the ideas of complexity, emergence, and "self-organization"; these phenomena are at the heart of what drives mesoscale science. The presence of nearly degenerate states representing different types of order—all of which compete—points to the need to make observations of particular types of order collectively, rather than individually (Dagotto, 2003).

The two-dimensional single crystal $La_{0.5}Sr_{1.5}MnO_4$, consisting of two-dimensional sheets of Mn-centered octahedra separated by La and Sr atoms spaced farther apart, has been chosen to compare the mechanisms of magnetic and orbital ordering. The order from each leads to scattering, which is

separated in reciprocal space. An optical pump laser was used to excite the system while measuring the diffraction intensity of each type of ordering. Using a pump pulse tuned to a phonon excitation, the Mn-O bond stretching vibration at 78 meV (or a wavelength of 16 μm), the orbital ordered state was found to decay on a time scale of 6 ps, a factor of 2 faster than the magnetic state (Först *et al.*, 2011). This is attributed to the requirement that magnetic ordering must disorder by a transfer of angular momentum, whereas the orbital only involves the rearrangement of the single electron wave function.

By changing the pump wavelength away from the phonon resonant frequency, the magnetic order was studied and observed to disappear on a 250 fs scale. The shorter characteristic time is due to the electronic excitation, which is much faster because it involves charge transfer across the gap. A mid-IR pulse was then used to compare excitation mechanisms on the magnetic state by inducing the Mn-O bond stretching vibration at 78 meV (16 μm). This type of pump drives a lattice excitation which exhibits much slower magnetic dynamics, since it decouples the exchange mechanisms governing the antiferromagnetic state (Först *et al.*, 2011). By measuring the response of the magnetic structure with different excitations, the role of magnetic dynamics from the ultrafast pulsed x rays was elucidated further for separate energy landscapes. Moreover, by measuring the width of the magnetic diffraction peak in reciprocal space with a two-dimensional detector (Doering *et al.*, 2011), the three-dimensional correlation length of the antiferromagnetic structure could be measured on ultrafast time scales as well. This demonstrates the importance of making measurements in three dimensions even for 2D materials, as a transient, incommensurate ordered state was shown to surface in the out-of-plane direction 1 ps after the IR excitation. However, by about 10 ps, the anisotropic transient state had vanished (Tobey *et al.*, 2012).

When atomic motion becomes a quantity of interest, x rays are used to study lattice dynamics. In manganite systems, the atomic motion is especially important because it determines the Mn-O-Mn bond angle, a critical factor in the magnetism and conductivity of the system (Zener, 1951). In the three-dimensional system $La_{0.7}Sr_{0.3}MnO_3$, a midinfrared femtosecond pulse can be tailored to the same specific lattice vibration as in the 2D systems. The response is measured with ultrafast x-ray diffraction to show that excitation of an infrared-active stretching mode in the nonlinear regime can induce a structural phase transition (Först *et al.*, 2013). By measuring the long-lived state via two different Bragg reflections, ionic Raman scattering theory was shown to properly predict the atomic displacement from the nonlinear excitation.

Resonant x-ray scattering in the hard x-ray regime can be used to study the interplay of different types of order with lattice dynamics, yielding information on the competing collective interactions. Different superlattice and lattice reflections were measured in $Pr_{0.5}Ca_{0.5}MnO_3$, each susceptible to a different component of a phase transition (Beaud *et al.*, 2014). The responses differ because each involves a change of the charge or orbital ordering in addition to the lattice symmetry. By looking at different diffraction peaks for the same process, dynamics could be compared for the orbital order, Jahn-Teller distortion, charge order, and the structural distortion (Beaud *et al.*, 2014). Figure 23 shows the time dependence of the $q = (\bar{2}, 1/2, 0)$ peak identifying the dynamics of the lattice.

Taking all these responses together, a simple model was used to capture the basic dynamics of the much more complicated manganite system. From the equations of motion, simulations were performed on the structural response of the material on ultrafast time scales. This method is analogous to Landau theory if the ratio of the excitation density to a critical excitation density n/n_c is used to replace the traditional T/T_c order parameter, pointing to a new universal description of complex phase transitions in the time domain (Beaud *et al.*, 2014).

d. Multiferroics

When ferromagnetism and ferroelectricity exist within a material without the application of an electric or magnetic

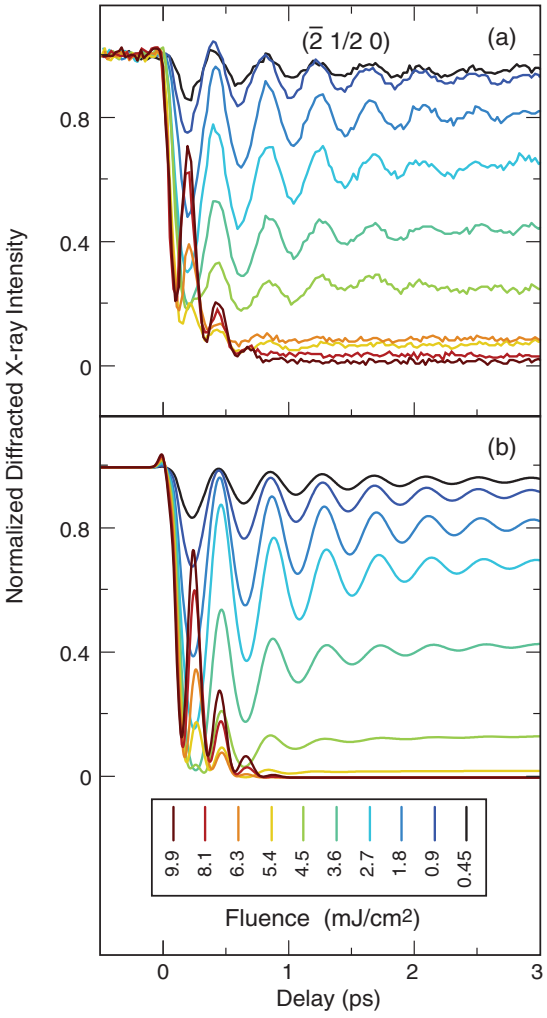

FIG. 23. The x-ray diffraction peak shown as an intensity as a function of time, describing the dynamics of the atomic structure of a $Pr_{0.5}Ca_{0.5}MnO_3$ manganite single crystal. The bottom panel shows a simulation using a simple model based on Landau theory for a second-order phase transition. These are both shown as a function of fluence, the analog of the order parameter, used for the theoretical model. From Beaud *et al.*, 2014.

field, it is said to be multiferroic. Rapid development has occurred in this field, partly due to the potential for practical applications such as electrically controlled magnetic memory, four-state logic, and magnetoelectical sensors (Khomskii, 2009).

Thin ferroelectric nanolayers of $PbTiO_3$ on different substrates were studied at LCLS by Bragg scattering from the crystal structure while exciting the system with UV light to reveal the role of strain in these systems (Daranciang *et al.*, 2012). Changes in the tetragonal structure were found on femtosecond time scales and lasted up to several nanoseconds. The photovoltaic response can be understood by comparing it to a Landau-Ginzburg-Devonshire model, which predicts the relationship between the polarization, the lattice parameters, and the strain of the film. Such a simulation matches the data measured, showing both screening of the internal fields and saturation effects as a function of fluence. The dynamical effects of the photogenerated time-dependent internal fields interacting with the strain of the film portray the intrinsic photovoltaic response of the feroelectric film driven by a current modulation (Daranciang *et al.*, 2012).

By tuning the x-ray energy to a magnetic resonance, a magnetic ordering peak of a multiferroic can be studied while illuminating the system with specific wavelengths of light. By creating a nearly single-cycle THz electric-field pulse, the magnetic structure of a different type of manganite, the multiferroic material $TbMnO_3$, was monitored while the resonance of an electromagnon was excited by the high-field pulse (see Fig. 24). This offered the opportunity to drive a selective spin excitation while studying the precise behavior of the cycloid magnetic structure (Kubacka *et al.*, 2014). The magnetic structure was found to be manipulated by a rotation of about 4 deg. From scaling considerations, it was found that 90-deg switching could be attained by reasonable improvement to the THz field to about 1 or 2 MeV cm^{-1}, less than an order of magnitude increase from the best electric-field strengths currently generated by this method. Not only does this open the door to potential future applications of switching cycloid spiral states, but more importantly it was also shown that ultrafast switching could be done with much less energy, supporting the idea of multiferroic devices being used for switching in a much more efficient manner.

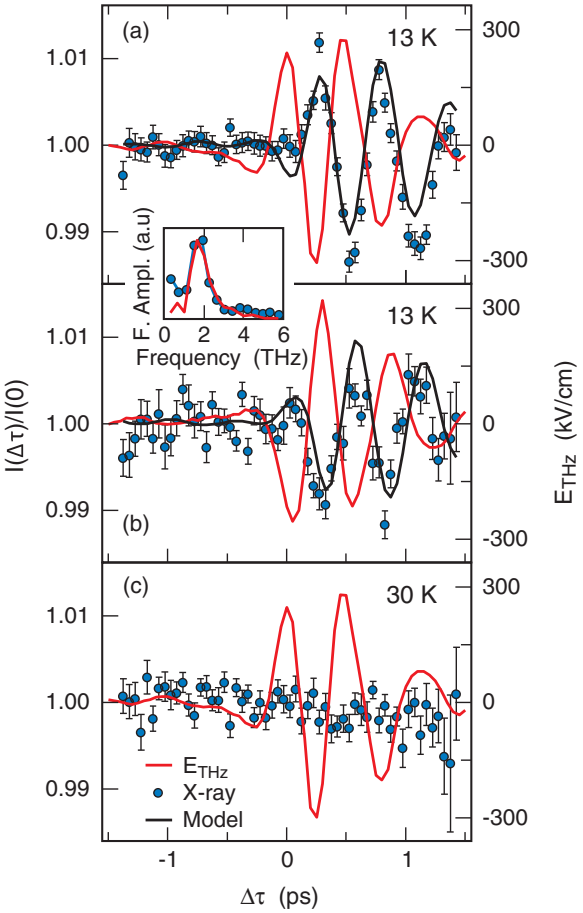

FIG. 24. Time-dependent behavior of an electromagnon. The magnetic diffraction of the $(0k0)$ peak of $TbMnO_3$ (blue symbols) is compared with the electric field of the THz pump (red solid lines) as a function of the time delay. (a) The response of the sample in the multiferroic phase at $T = 13$ K and for (b) an inverted electric-field driving pulse. (c) The response for the system in the spin-density wave phase for $T = 30$ K, where the effect vanishes. From Kubacka *et al.*, 2014.

2. Heterostructures and interfaces

Heterostructure and interface phenomena have gained attention in materials research due to the unusual effects that appear in these states, but differ from the behavior of the bulk system. For instance, in the area of photovoltaics, one example of interface structure that dramatically affects the functionality is in dye-sensitized solar cells (Sec. IV.D.1). These are systems where dye molecules are chemically added to a nanostructured semiconductor to increase the efficiency of photon harvesting (O'Regan and Grätzel, 1991). Charge transfer can also be induced between nonequivalent sites within a heterostructure, such as was done between different Ni ions within an epitaxially grown thin film. In $NdNiO_3$ thin films, for instance, the two magnetic elements each produce a different sublattice of antiferromagnetic order (Scagnoli *et al.*, 2008). By photoexciting the film, charge transfer was induced in the magnetic material to melt the magnetic order while monitoring the magnetic Bragg reflections in time for each of the two magnetic sublattices. The two types of antiferromagnetic order on both the Ni and the Nd sites, which are always locked in equilibrium, were found to decouple, and each produced a different type of dynamics. This rebalancing of spectral weight was also observed as a function of pump fluence, and was found to involve the charge disproportionation from the different types of electronic states, from the t_{2g} to e_g electron states (Caviglia *et al.*, 2013). The change in wave function per site perturbs the hybridization of the magnetic ion and its surrounding oxygen ligands, which is directly coupled to the antiferromagnetic order (Mizokawa, Khomskii, and Sawatzky, 2000).

Another mechanism that LCLS has contributed to understanding is the induction of interfacial phenomena in a heterostructure without direct charge transfer. Because the strain from epitaxial film growth mentioned above can be used to control the film properties such as the transition temperature (Catalan, Bowman, and Gregg, 2000), exciting a specific

phonon mode in the substrate can also lead to a change in the properties of the film via an interfacial lattice distortion. This type of lattice control and how it affects the magnetic structure has been studied in a 30 nm film of $NdNiO_3$ (Först *et al.*, 2015). By resonantly pumping the highest phonon mode in the $LaAlO_3$ substrate at 82 meV (or a wavelength of 15 μm), a magnetic wave front propagates from the substrate interface into the film at a speed that is at, or faster than, sound propagation in the film. This structural change at the interface was due to a heterogeneous magnetic front propagation which was due to electronically driven motion, rather than from heat propagation. Light control at heterointerfaces, to modify magnetization dynamics such as this, could offer potential for novel opportunities in optomagnetism, such as driving domain wall states as a mechanism for transporting information across magnetic devices.

3. Low-dimensional magnetism

Magnetism in low-dimensional systems is important in condensed matter, especially as it relates to future storage device technology, memory, and new types of electronics. By using single-shot imaging techniques in low-dimensional systems, i.e., Fourier transform holography (Eisebitt *et al.*, 2004) or coherent diffraction imaging (Turner *et al.*, 2011), combined with the properties of LCLS, the dynamics of magnetic fluctuations and magnetization relaxation processes can be visualized at nanometer length scales and on femtosecond time scales. First magnetic snapshots were recorded using single LCLS x-ray pulses below 80 fs to capture the real-space image of ferromagnetic domains (Wang *et al.*, 2012). At this pulse duration, it was found that magnetic images could be recorded before the accumulated x-ray pulse energy damaged the 48 nm thin film. Multiplexed x-ray holography allowed the measurement of both the minimum pulse energy it took to extract the image at 5 mJ/cm^2, the damage threshold for single-shot imaging at 25 mJ/cm^2 or greater, and pulse durations of 360 fs or greater. This paves the way for studying excited-state dynamics of ferromagnetic domains, which would offer a first view at magnetization dynamics on the necessary and important length scales of ferromagnetic domains.

Ultrafast resonant diffraction experiments in a forward scattering geometry are also a natural method for understanding magnetic interactions in low-dimensional solids. They offer the same spatiotemporal scales for study in reciprocal space without the added complexity of converting the scattering information into real-space images (Bergeard *et al.*, 2015). For instance, ultrafast scattering experiments were used to study nonequilibrium magnetization dynamics in a ferrimagnetic alloy of GdFeCo (Graves *et al.*, 2013), a material known for its ability to switch magnetic states induced by a laser pulse (Radu *et al.*, 2011). Resonant magnetic scattering was used to enhance and discriminate the charge and magnetic scattering matrix elements:

$$F_q^{\pm} = C_q e^{-i\phi} \pm S_q e^{-i\gamma}, \tag{8}$$

where C_q and S_q are defined as the Fourier amplitudes of the charge and magnetic distributions, and ϕ and γ are the charge and magnetic phases, respectively, using the electric dipole formalism (Hill and McMorrow, 1996). By using the circular polarization of the x-ray beam, the magnetic amplitude can be isolated from the charge scattering. Figure 25 shows this normalized magnetic structure factor, S_q in Eq. (8), as a function of time for Gd $4f$ (red) and Fe $3d$ (blue) spins for both low- and high-q regions and for short times [Fig. 25(a)] and long times [Fig. 25(b)], where the separation in q was defined by $q = 0.2$ nm^{-1}. The chemical inhomogeneity could also be differentiated using other probes and related to the transient spin states that were found to be a result of nonlocal transfer of angular momentum from Fe-rich regions to Gd-rich regions (Graves *et al.*, 2013). These results suggest the possibility of preparing microscopically engineered magnetic materials whose excited spin states could be harnessed in new technologies, such as heat-assisted magnetic recording.

4. Imaging lattice dynamics

The study of deviations from a lattice has long been a mainstay of condensed matter physics and materials science. The concept of the phonon represents the importance of dynamics in these studies and is central to our understanding of mechanical and electronic properties of solids. As condensed matter physics has matured, the study of materials

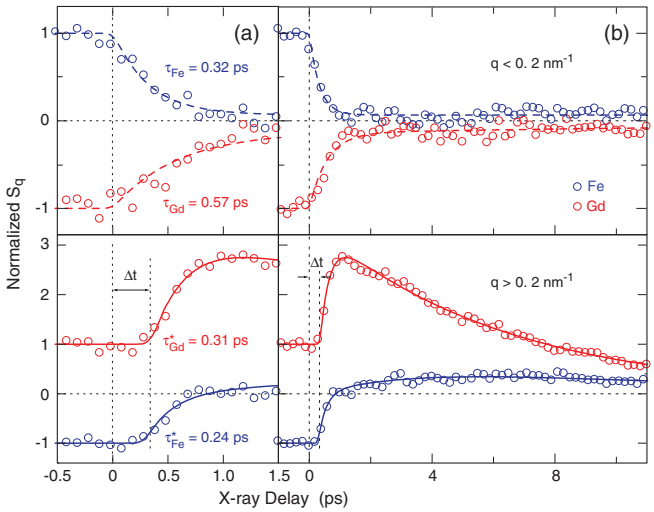

FIG. 25. Reversal of Gd spins within nanoscale Gd-rich regions as measured by resonant x-ray diffraction. (a) Temporal evolution of the magnetic structure factor S_q for Gd $4f$ spins (red) and Fe $3d$ spins (blue) measuring the local deviations from the average magnetization. (b) The same S_q data but on a longer time scale. The S_q signals were integrated over the low-q region of the magnetic diffraction pattern ($q < 0.2$ nm^{-1}) and high-q ($q > 0.2$ nm^{-1}) regions and are normalized to the equilibrium values. Therefore, $|S_q(t < 0)| = 1$ for both q ranges and sublattices, although high-q S_q for Gd is ~4 times greater than for Fe. Dashed and solid lines represent fits of exponential decay and rise functions to the data. The observed delayed onset at $\Delta t = 360 \pm 50$ fs indicates that angular momentum transfer effectively occurs only after this time delay. Beyond 1 ps, the Gd (Fe) data are well described by an exponential decay (rise) with a time constant of 6 ± 2 ps. The Fe data are fit with an additional decay with time constant 8 ps. From Graves *et al.*, 2013.

properties has grown to include increasingly minute deviations in space and time from a perfect lattice, and the effects of this strain within the material are used to explain and model, for example, "ultrastrength" materials (Li, Shan, and Ma, 2014) and optical properties in Si nanowires (Lyons *et al.*, 2002).

LCLS can provide powerful and rare tools for the study of these properties using the high spectral brightness of the source, which allows the explicit use of coherent scattering techniques. In particular, when a crystal is illuminated by an x-ray beam that possesses transverse coherence lengths greater than the extent of the crystal, the far-field diffraction data can be used to recover a three-dimensional map of the index of refraction inside the crystal. It is then possible to infer the strain it is experiencing at the instant of the x-ray illumination. This capability allows for pump-probe experiments that can provide valuable insight into problems ranging from materials failure to catalysis.

The first example of this capability was demonstrated by examining the time response of the lattice of a small metallic particle upon excitation with an optical-laser pump (Clark *et al.*, 2013). In that experiment, the continuous diffraction pattern surrounding a Bragg reflection of the small crystals was measured at a series of time delays with respect to the excitation laser pulse. These diffraction data were used to image the crystal shape and lattice deformation at each delay; thus the data set provides the information needed to visualize the lattice dynamics at small time steps and over a period much longer than it would take for an acoustic wave to traverse the crystal. This difficult-to-obtain information will provide new insight on the time-resolved lattice displacements inside a material, potentially leading to unique opportunities for engineering nanomaterials.

In materials systems where it is difficult to identify a discrete unit, such as a nanocrystalline domain, inelastic x-ray scattering methods can be extended to the time domain. Traditionally, x rays are used to determine the spectrum of the excitations in a single crystal by measuring the energy and momentum of inelastically scattered photons (Krisch and Sette, 2007); however, LCLS can be used to perform this measurement in the time domain directly. Investigations were carried out on a single-crystal germanium sample in an optical-pump x-ray-probe experiment to determine the phonon dispersion at room temperature (Trigo *et al.*, 2013). An optical pulse was used to excite the sample and an x-ray pulse, at variable delay, to probe the resultant excitation by measuring the diffuse x-ray scattering signal. Here the very short pulse duration, compared to the induced vibrational frequency, is used to directly probe the equal-time correlations of the excitation as a function of the pump-probe delay time, effectively executing a direct stroboscopic measurement of large portions of the phonon dispersion in the material. An example of both the individual frames of the diffuse scattering signal and its time evolution is depicted in Fig. 26. The method is particularly valuable in that it provides more-or-less direct access to transient states.

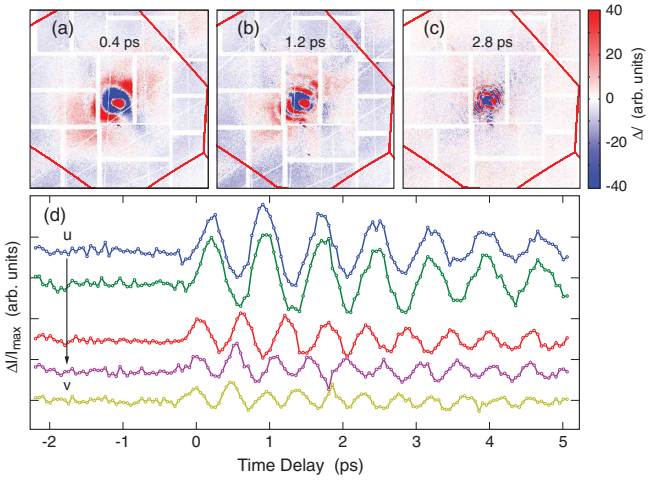

FIG. 26. Time-resolved diffuse scattering measurements of Ge. (a)–(c) Typical frames depicting the oscillatory component of the diffuse scattering collected from the (022) Brillouin zone in Ge, after background correction, at 0.4, 1.2 and 2.8 ps. (d) A demonstration of the variation in the normalized diffuse scattering intensity as a function of time delay at select wave vectors from $u = (-0.1, 0.00, -0.08)$ to $v = (-0.33, 0.15, -0.27)$ in reciprocal lattice units. From Trigo *et al.*, 2013.

5. Perspectives

In the lead-up to first light at LCLS, considerable uncertainty surrounded the applicability of the high spectral brightness to many materials systems. Certainly, the study of matter in extreme conditions, discussed in Sec. IV.C, requires high-energy density beams to transform materials in a irreversible way. However, in materials studies outlined here that use the same sample illumination volume to study excitation and relaxation processes in a time-dependent way, the pulse characteristics become critical for ensuring that the stable-state sample properties are not appreciably changed in a single shot or even after many shots. Because of the ability to avoid sample damage threshold values (Hájková *et al.*, 2011) by both adjusting the x-ray spot size and attenuating the peak pulse energy for precise control of the x-ray flux at the sample position, time-dependent studies of condensed matter have blossomed in the last five years at LCLS. As a result, many discoveries into the electronic and atomic structure in a myriad of materials and in both the spatial and time domains have occurred (Turner, 2014). Based on the results reviewed in this section, the future generation of high-repetition rate facilities is expected to show great promise for the field of condensed matter and materials physics (Sec. V). New techniques becoming standard are anticipated (for example, resonant inelastic x-ray scattering, time-resolved photoemission, and atomic-scale time-resolved structural studies) as well as the possibility of making new measurements that are currently impractical, such as studying changes in x-ray scattering at the 10^{-5} level.

C. Matter in extreme conditions

Understanding the multiscale response of materials under high pressures or temperatures is of central importance to fundamental research in numerous fields, including high-energy density science, geoscience, planetary science, laboratory astrophysics, relativistic laser plasmas, and fusion research. Studying the dynamic behavior of materials under

extreme conditions is a challenge that requires the creation of well-defined and well-diagnosed plasmas. The combination of x-ray free-electron lasers, high power lasers, and advanced diagnostics provides state-of-the-art experimental platforms that can be used to create and study the behavior of matter under these extreme conditions, which generally involve short-lived nonequilibrium states that evolve on tens of femtoseconds to nanoseconds. Diagnostic techniques must be able to resolve these time scales. X-ray FELs with pulse durations in the range of 10–100 fs provide diagnostic sources that can penetrate solid-density material, isochorically heat matter to temperatures of >10 eV, and selectively pump atomic transitions on femtosecond time scales.

Experiments involving high pressures and temperatures often fall under the high-energy density regime, defined as matter at solid density and at temperatures exceeding 1 eV (=11 600 K), or, equivalently, pressures exceeding 1 megabar (Mbar), as shown in Fig. 27 (Cowley *et al.*, 2010). The properties of an x-ray FEL source facilitate experimental access to an important subset of this regime, namely, the properties of dense matter in two extreme states: warm dense matter (WDM) and hot dense matter (HDM). WDM is material at near-solid density and a finite temperature, e.g., from 1 to ∼10 eV, comparable to the Fermi energy (Lee, 2007). Theoretical understanding of this regime is complicated by the fact that it is not well described by condensed matter or plasma theories. Similarly, HDM can also have near-solid density but at temperatures ranging from tens of eV up to many keV. Experimentally, there have been two main challenges to understanding the behavior of these states of matter. First is the creation of dense matter that is uniform and well quantified. Second is the development of diagnostics that can probe the bulk properties of these states. In this section, recent results obtained at LCLS on WDM, HDM, and laser driven shock compression are discussed, followed by a discussion of emerging future research areas that use high-intensity lasers.

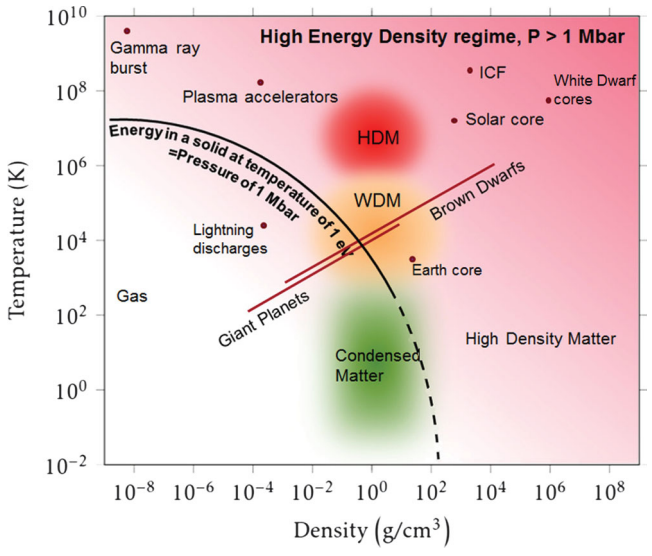

FIG. 27. Map of the high-energy density (HED) regime above $P = 1$ Mbar. HED science includes study of warm dense matter (WDM), hot dense matter (HDM), interior of planets, astrophysics, relativistic laser plasmas, and inertial confinement fusion (ICF) research.

1. Warm dense matter and hot dense matter

Optical-laser systems and x-ray FEL beams can both create high-density plasmas with temperatures up to hundreds of eV. A range of novel conditions can be generated and studied by the FEL beam, making use of the tunability, submicron focusing capability, and highly penetrating nature of these ultrashort bursts of x rays.

Intense pulses from x-ray FELs interact predominantly by rapidly ionizing the K-shell or L-shell electrons, creating plasmas at solid density. These types of plasmas have proven difficult to model and are very challenging to study in a controlled, laboratory environment. As a consequence, there is a great deal of uncertainty regarding how such systems behave. With the ability to create well-defined plasmas using ultrashort x-ray FEL pulses, x-ray emission spectra can be used to yield basic atomic physics information for the development of population kinetic models of the system. Such measurements are key building blocks for understanding the behavior of WDM or HDM (Lee, 2007).

Prior to the advent of LCLS, models predicted that x-ray FELs could be used as pumps to generate measurable emission spectra from WDM (Chung and Lee, 2009). For example, the Lyman-α line at ∼1724 eV, which is unobservable in the He-like background emission before photo pumping with an x-ray FEL pulse, was simulated to rise above the background after an x-ray FEL pump pulse, as shown in Fig. 28. These simulations predicted that LCLS pulses would be capable of providing unique constraints on the complex processes needed to construct a complete kinetics model for highly charged ions. Moreover, the tunability of the x-ray FEL photon energy would allow selective pumping of particular transitions so that specific population changes could be measured. In high-energy density plasmas, models also

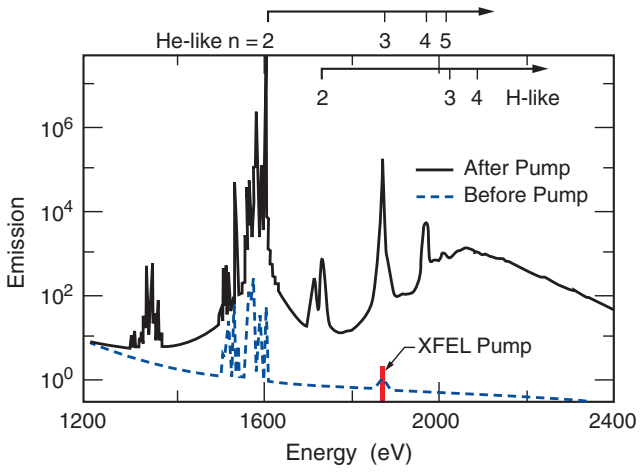

FIG. 28. The logarithm of the calculated emission spectrum from the Al plasma (blue dashed curve) and calculated emission spectrum at 100 fs after the simulated x-ray FEL pumps the He-like $n = 1$ to $n = 3$ transition (black solid curve). The major predicted effect of the intense x-ray pump is to cause photoionization. Adapted from Chung and Lee, 2009.

predicted that the dense environment surrounding an atom would influence the ionization potential of the atoms, modify the energy levels and further impact spontaneous transitions.

Early work in this area using LCLS studied the manner in which x rays ionize and heat the electrons of a metal to above 100 eV, creating *K*-shell holes (Vinko *et al.*, 2012). During this process the free-electron density in the sample increases and the characteristic screening length, i.e., the Debye length, becomes shorter than the interparticle distance. This perturbs the electrostatic potential distribution of the ions, inducing ionization potential depression. Similar physics in the atomic limit for nanometer-sized clusters has been discussed in Sec. IV.A.1; however, for dense plasmas, this type of phenomena strongly affects the ionization, equation of state, and opacity of the system by changing the number of bound states and the charge state distribution. Such properties are of central importance to the ability to predict the evolution of the types of systems shown in Fig. 27.

Subsequent experiments again using LCLS allowed the efficiency and uniformity of heating induced by a hard x-ray FEL source to be investigated in terms of temperature and electronic relaxation processes (Levy *et al.*, 2015). High-energy deposition on the order of 10^{15} W/cm^2 from 8.9 keV x-ray pulses of 60 fs duration within Ag solid foils enabled a rapid transfer of the energy via inner-shell ionization before hydrodynamic expansion. Time- and space-resolved interferometers were used to measure symmetric expansion of front and rear surfaces, illustrating the uniformity of energy deposition over the entire sample thickness. The experimental results were favorably compared with the electron density and temperature spatial profile resulting from two simulation codes, showing that valuable benchmark systems can be created, enabling the study of a range of important phenomena (Gaudin *et al.*, 2012; Peyrusse, 2012).

Multiple experiments have used LCLS to irradiate a solid-density sample and measure subsequent *K*-shell emission of dense aluminum plasmas, revealing saturation of the absorption induced by the ionization in the x-ray regime (Rackstraw *et al.*, 2015) and much larger lowering of the ionization potential (Cho *et al.*, 2012; Ciricosta *et al.*, 2012; Vinko *et al.*, 2012, 2015; Vinko, Ciricosta, and Wark, 2014) than predicted by commonly used plasma models (Stewart and Pyatt, 1966). Spectroscopic measurements observed various emission lines corresponding to different charge states of the aluminum ion as a function of the photon energy of the x-ray pump as shown in Fig. 29. The positions of the *K* edges were extracted from the intensity of various emission lines containing one hole in the *K* shell, created by the LCLS beam, and an additional number of holes in the *L* shell. These studies represented the first direct measurement of ionization potential depression (Ciricosta *et al.*, 2012) and the collisional ionization rate in a dense plasma (Vinko *et al.*, 2015). These results led to a reexamination of long-standing theoretical models (Ecker and Kröll, 1963; Stewart and Pyatt, 1966) and have led to a resurgence of theoretical work in this area (Crowley, 2014; Son *et al.*, 2014).

The conductivity of isochorically heated warm dense aluminum created by hard x-ray FEL irradiation was also studied by measuring plasmon damping (Sperling *et al.*, 2015). From the data obtained in these experiments the imaginary part of the inverse dielectric function associated with plasmon spectral intensity (Glenzer and Redmer, 2009) was extracted while the real part of the inverse dielectric function was evaluated using Kramers-Kronig relations (Toll, 1956). Detailed comparison with theoretical predictions showed that the plasmon spectrum was sensitive to electron-ion collision processes. In addition, the dc conductivity inferred from the data agreed with the Born model in the warm dense matter regime (Reinholz *et al.*, 2015). Warm dense carbon created by a 300 fs duration optical-laser pulse was also studied as it evolved over several tens of picoseconds, and strong evidence for the existence of a glassy state was obtained (Brown *et al.*, 2014). The plasma state explored in this experiment is comparable to the conditions predicted to exist in a white dwarf star, and this result indicated that the existence and duration of an intermediate glassy state in white dwarf stars would affect their thermal conductivity and overall luminosity.

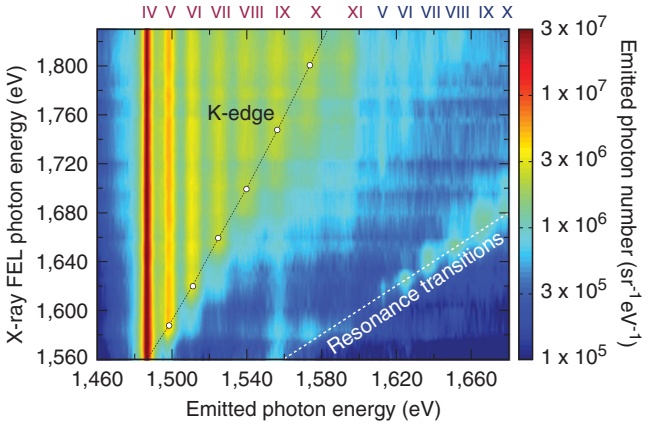

FIG. 29. Spectrally resolved Al Kα emission as a function of the x-ray FEL excitation photon energy from 1460 to 1680 eV. Emission lines from Al charge states from 4^+ to 10^+ are marked in Roman numerals: red for states with a single *K*-shell hole and blue for states with a double *K*-shell hole. Adapted from Vinko *et al.*, 2012.

2. High-pressure states under dynamic compression

High-pressure states at temperature around 1 eV can be generated by dynamically compressing a sample with an energetic optical-laser pulse. These states have long been studied to understand structural transitions (Kalantar *et al.*, 2005), high strain rate phenomena (Remington *et al.*, 2006), melting behavior (Ping *et al.*, 2013), and transition kinetics (Smith *et al.*, 2014) in other facilities. These studies provided insight into the nature and time scales of phase transitions and material response under extreme conditions. The use of nanosecond lasers to drive these high-pressure states allows rigorous comparisons to be made with static compression of the same phenomena as studied using diamond anvil cells. However, there have been considerable challenges in diagnosing phase transitions, dynamic response and kinetics within short time scales that result in a weak diffraction signal from a material undergoing a transition from the solid to a molten phase. The coupling of energetic optical lasers for

dynamic compression with ultrabright femtosecond x-ray FEL probes and associated diagnostics has provided new methods to explore the kinetics of phase transformations with simultaneous high temporal and spatial resolution. Studies to date have extended across a broad span of induced pressures, with key highlights presented next.

In the lower pressure range, the unique capabilities of LCLS were used to study the evolution of a copper structure under dynamic compression on picosecond time scales. This work showed that the material exhibited an elastic response, resisting plastic deformation up to a peak normal stress of ~73 GPa. This agreed well with molecular dynamics (MD) simulations at a strain rate of $10^9/\mathrm{s}$ (Milathianaki *et al.*, 2013). Snapshots of the structure of shock-compressed copper at 20 ps time intervals revealed the subsequent emergence of a diffraction peak, indicating an elastic response. A broad feature associated with plastic relaxation was also observed at longer time delays; see Fig. 30. Efforts to understand material strength at high pressure and strain rate have evoked interest in simulating compression experiments and developing a full model of dynamic compression (Higginbotham and McGonegle, 2014; McGonegle *et al.*, 2015).

Moving beyond elastic and plastic behavior, an understanding of the kinetics of structural phase transitions is desired in order to better understand material strength and the dynamic response of materials in extreme environments. However, obtaining atomic data in the nonequilibrium state during the process of a material phase transition has remained elusive until now. One recent example is the use of LCLS to measure the melting of bismuth during shock loading using x-ray diffraction techniques (Gorman *et al.*, 2015). A phase transition from the high-pressure body-centered cubic Bi-V phase to the liquid phase was observed, allowing an upper limit for the time scale of melting in bismuth to be quantitatively measured. This showed that the process was much more rapid than anticipated, occurring in just a few nanoseconds. A similar experimental approach was then used to provide the first results of shock-induced nanosecond nucleation and growth of a high-pressure crystalline phase from initially amorphous material. The experiment used shock-compressed fused silica, one of Earth's most abundant minerals, under conditions similar to those experienced in a large meteorite strike. The transition from amorphous silica to crystalline high-pressure stishovite was observed within the first few nanoseconds (Gleason *et al.*, 2015), unexpectedly supporting a coalescence growth model rather than a diffusion-based mechanism. Measuring the kinetics of such nonequilibrium processes by which atoms rearrange themselves advances our understanding of phase transformation pathways and this knowledge is of general importance to a range of interesting materials.

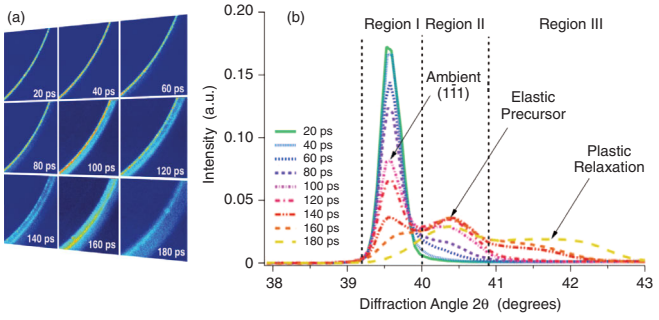

FIG. 30. (a) A section of a Debye-Scherrer ring showing evolution of lattice dynamics with time delay. (b) A diffraction profile illustrating the characteristic lattice response. Adapted from Milathianaki *et al.*, 2013.

Seeding the LCLS beam to produce a narrow-bandwidth (0.05%) source (see Sec. II.B.2) allowed such measurements to extend into the plasma regime and diagnose the evolution of plasmon spectra under shock compression (Fletcher *et al.*, 2013). The plasmon frequency shift from the incident x-ray probe energy is a sensitive measure of the electron density via the Bohm-Gross dispersion relation (Bohm and Gross, 1949; Glenzer and Redmer, 2009). Measurements of this plasmon feature and wave-number-resolved scattering data of shock-compressed aluminum were used to characterize the compression and melting phase of laser heated aluminum as it transitioned from room temperature into warm dense matter (Fletcher *et al.*, 2015).

X-ray phase contrast imaging provides the capability of imaging density perturbations inside optically opaque, but x-ray transparent materials. This technique is sensitive to small changes in the refractive index and can thus reveal subtle phenomena of interest to laser fusion and laboratory astrophysics studies (Snigirev *et al.*, 1995; Montgomery, Nobile, and Walsh, 2004). It can be used with keV x-ray FEL beams to image the evolution of shock fronts driven by a short pulse optical laser, and other density perturbations inside laser heated materials with, in principle, 10 s of femtosecond temporal resolution. For such measurements, it is critically important to characterize the wave front and intensity distribution of the nanofocused x-ray FEL beam. This was recently achieved via use of an x-ray phase contrast imaging instrument utilizing beryllium compound refractive (Schropp *et al.*, 2013). This nanofocused x-ray beam was then used to image shock fronts in diamond with submicron spatial resolution (Schropp *et al.*, 2015). The experiment demonstrated that elastic compression waves and shock widths inside diamond could be visualized *in situ* with high spatial resolutions (~500 nm) by ~50 fs x-ray FEL pulse.

Finally, ultrafast time-resolved x-ray absorption near-edge spectroscopic measurements using x-ray FELs offer information about electronic structure changes and dynamics of the lattice short-range order during metal-nonmetal transitions (Harmand *et al.*, 2015). Using an FEL pulse duration of less than 100 fs and an ultrabright beam of 10^{12-13} photons/pulse generates absorption spectra that can probe fast processes during dynamic compression. By averaging over 20 pulses, significant statistical accuracy can be achieved. Methods that utilize these sharp spectral features of the FEL source as a probe beam have been carefully described (Gaudin *et al.*, 2014). A preedge feature around the Fe K edge, predicted by the hybridization of the $3d$-$4p$ band within the hcp phase (Raji and Scandolo, 2014), was observed in the spectrum when a Fe foil sample was driven to a pressure of 130 GPa by optical-laser compression. The modification and disappearance of this preedge feature was interpreted as a signature of a change of the electronic unoccupied density of state along the Hugoniot

and on the release adiabat, respectively. This result suggested that iron was molten at pressures and temperatures higher than ~260 GPa and ~5680 K along the principal Fe Hugoniot.

3. Perspectives

As illustrated previously, material dynamics have so far been studied up to pressures of 10–500 GPa. Looking forward, the likely availability of optical-laser systems with significantly increased intensity and per pulse energy should enable the creation of plasma conditions of direct relevance to a broader range of astrophysical bodies. For example, a nanosecond optical-laser system at the kJ level can produce material pressures in excess of 1000 GPa. Under these conditions, dense matter becomes strongly coupled and the plasma becomes Fermi degenerate. Studies in this regime are required to understand the formation and evolution of giant planets such as Jupiter and Saturn (Van Horn, 1991; McMahon, Morales, and Pierleoni, 2012). To study these extreme phases of matter, hard x-ray FELs with energies over 20 keV will be required to overcome the plasma self-emission, allowing measurements of compressibility, opacity, plasma dispersion, and the dynamics of previously unexplored phase transitions.

In the area of highly transient plasmas (i.e., 1–1000 fs), compact high power short pulse laser systems in the 100–1000 TW regime make it possible to generate relativistic plasma flows similar to those associated with the phenomena of astrophysical shocks. Numerical simulations using 3D particle-in-cell (PIC) codes have demonstrated the possibility of generating Weibel-instability-mediated collissionless shocks in the laboratory via the interaction of an ultraintense laser pulse with solid-density plasmas. This interaction leads to the generation of short-lived, micron-scale magnetic field filaments in the solid-density plasma (Fiuza *et al.*, 2012). It is impossible to directly visualize these filaments with standard optical diagnostics, which cannot penetrate dense plasmas. X-ray FELs enable direct visualization of submicron-scale filaments as they evolve on the 10–100 s femtosecond time scale inside dense plasmas. The coupling of short pulse, high-intensity laser systems with advanced x-ray FELs therefore represents a unique opportunity to characterize the spatio-temporal structure of phenomena such as the Weibel instability via phase contrast imaging. Small-angle x-ray scattering techniques can also be used to diagnose density features on the nm scale around these filamentary structures.

Studying the time-resolved atomic physics of isochorically heated warm dense matter created by x-ray FELs is challenging due to a lack of broadband spectroscopic probes with better than a picosecond time resolution. However, the recent development of laser driven secondary sources such as betatron x-ray emission from laser accelerated electrons opens the possibility of probing atomic structure on the 50–100 fs time scale. Betatron radiation is driven by GeV electrons, which are accelerated during the interaction of a femtosecond-duration optical-laser pulse with a gas target at high intensity (exceeding 10^{18} W/cm^2). These electrons are accelerated up to GeV energies via highly nonlinear laser-wakefield mechanisms in a well-behaved beam as reported on prior to the existence of LCLS (Faure *et al.*, 2004; Geddes *et al.*, 2004; Mangles *et al.*, 2004). These GeV electrons produce broadband betatron radiation in the keV photon energy range (Albert *et al.*, 2008). This source can be applied to perform x-ray absorption spectroscopy of nonthermal processes (Rousse *et al.*, 2001) and nonequilibrium conditions in warm dense matter on 10–100 s of femtosecond time scales. Such a source will provide a valuable diagnostic for x-ray FEL experiments, allowing the study of electron-ion equilibration dynamics in rapidly heated matter via x-ray absorption near-edge spectroscopy with a resolution approaching 40 fs.

Another important application of short pulse, high-intensity laser-plasma interaction physics is the creation of MeV proton beams. Laser-produced proton beams have been studied extensively over the past 15 years (Macchi, Borghesi, and Passoni, 2013). These protons can be used to probe electric and magnetic fields in plasmas (Borghesi *et al.*, 2002; Mackinnon *et al.*, 2004) or to create warm dense matter (Patel *et al.*, 2003). LCLS can be used as either a pump or probe in experiments with laser-produced protons. For example, laser accelerated MeV protons and other ions can test stopping power models of relevance to fusion structural materials and the fusion burn process itself. The x-ray FEL beam would be used to produce the uniform, well-characterized plasma crucial for the high precision measurements that are required to test various stopping models. Basic proton stopping dynamics have been studied by PIC simulation (Kim *et al.*, 2015). Short pulse laser systems are capable of providing peak laser intensity exceeding 10^{20} W/cm^2, which is high enough to accelerate protons to energies of 1–15 MeV. This is just the range of energies that is interesting for ion energy deposition in thermonuclear fusion plasmas.

D. Chemistry and soft matter

Molecular interactions in lower-ordered systems, for example, fluids or amorphous solids, frequently exhibit high mobility of atoms and molecules. They determine the vast majority of functional biological and chemical processes, but a deep theoretical understanding remains challenging because of the plentitude of coexisting, microscopically individual structures and processes that contribute to macroscopic effects. Measurements usually deal with mixed states of matter and are compared to complex theoretical computational chemistry models (Warshel and Levitt, 1976; Senn and Thiel, 2009). Techniques that freeze molecular motion by measuring snapshots of excited or equilibrium states have proven to be very successful, and experiments at LCLS frequently adopt this strategy. In pump-probe experiments (Sec. III.B.3), a light pulse produces a well-defined excited state of matter. This increases the specificity of measurements, by a probing second pulse, that follow the dynamics of an ensemble of molecules—either directly, by measuring emitted and absorbed x rays, or indirectly, by measuring emitted photoelectrons. During the last three decades, different techniques using short optical light pulses to measure the temporal evolution of a coherently excited molecular population on a potential energy surface (see Fig. 31) established the field of femtochemistry (Fleming, Martin, and Breton, 1988; Zewail, 1988; Maroncelli, Macinnis, and Fleming, 1989; Rose, Rosker, and Zewail, 1989).

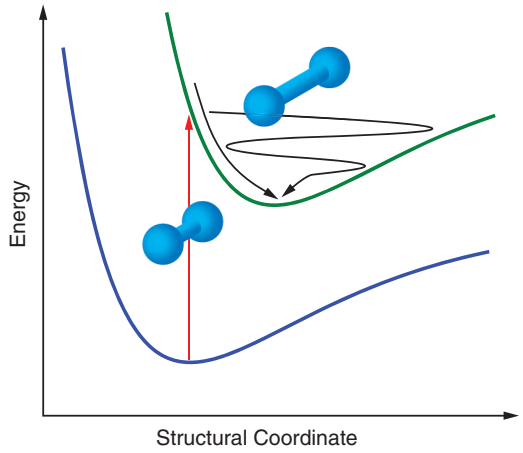

FIG. 31. A schematic of a dynamic structural change upon chemical transition. A model biatomic molecule is optically excited from the ground state to an electronic state with a different energy minimum from the ground state with respect to a structural degree of freedom.

The x-ray pulses produced by LCLS represent an ultrafast, element-specific structural probe for both electronic and nuclear structure that complements information from established techniques in femtochemistry. Additionally, the high transverse coherence allows measurement of microscopic molecular correlations over macroscopic length scales, which represents a totally new probe for liquid dynamics at ultrafast time scales.

1. Stimulated dynamics

a. Local electronic and nuclear structure

In femtochemistry, major attention has been devoted to transition-metal complexes that exhibit charge transfer from a central metal ion to a ligand network, as well as a transition to the high-spin state upon light excitation (Barbara, Meyer, and Ratner, 1996; Chen and Meyer, 1998; McCusker, 2003). A sound understanding of these ultrafast transitions is considered crucial for tailoring the physical and chemical properties of these materials, e.g., for applications in solar light conversion or energy and information storage.

The electronic transitions that determine these ultrafast processes can be effectively studied by x-ray spectroscopy, probing electronic levels of inner-shell electrons (see Fig. 32). Those remain to first order unchanged during chemical reactions, thereby avoiding ambiguities in transitions between core and valence states. This provides complementary information to optical spectroscopy, which explicitly probes valence transitions. The core levels are highly element specific, so local sites can be studied by tuning the x-ray energy to the specific elements (Zhang *et al.*, 2014).

As an example, an iron-based model system, iron(II) tris (2,2′-bipyridine) ($[Fe^{II}(bpy)_3]^{2+}$), has been investigated in solution by ultrafast x-ray absorption near-edge structure (XANES), as well as by x-ray emission spectroscopy (XES) using LCLS pulses. Previous studies by optical and x-ray methods have shown that the molecule, after initial optical excitation to a metal-to-ligand charge-transfer state (MLCT), undergoes a transition to a high-spin (HS) electronic state within less than 200 fs, thereby undergoing several changes in electronic and nuclear structure (Gawelda *et al.*, 2007; Bressler *et al.*, 2009; Chergui, 2013; Canton *et al.*, 2014). An unambiguous assignment of structural changes during these electronic transitions remained challenging, however, due to the short time scales of the processes.

XANES describes the detailed x-ray absorption cross section at energies close to the ionization threshold for core electrons. These electrons can fill the lowest unoccupied

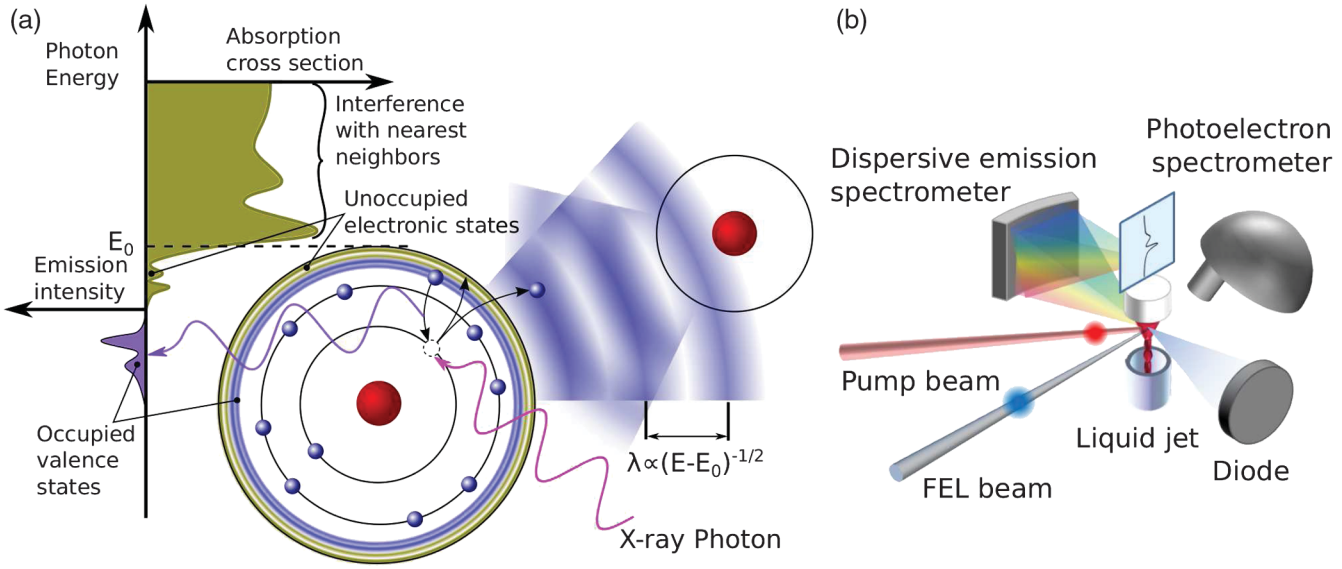

FIG. 32. (a) Representation of x-ray spectroscopy methods. The absorption cross section near an absorption edge of an inner-shell electron is sensitive to unoccupied electronic states just below the ionization energy E_0 and to the local structure around the excited atom. The generated hole can be occupied by a valence electron (e.g., from a highest occupied molecular orbital state, HOMO), thereby emitting x rays that represent electronic configurations. (b) Combination of experimental ultrafast x-ray spectroscopy setups. The absorption of the monochromatic incoming x-ray pulses is measured through the total fluorescence collected by an x-ray diode. Emission spectra are measured using a dispersive spectrometer. The kinetic energy of photoelectrons can be analyzed with a photoelectron spectrometer.

atomic or molecular orbitals (LUMO) of the excited atom or molecule. At higher excitation energies they can also interact with adjacent atoms giving rise to modulations from which nearest neighbor distances can be deduced (cf. Fig. 32). Time-resolved XANES is therefore sensitive to ultrafast changes in both the electronic and nuclear structures in a specific element and is well suited to investigate the charge-transfer and local structural changes due to spin transition experienced by the iron atom in $[Fe^{II}(bpy)_3]^{2+}$. Using a scanning monochromator, it was possible to measure ultrafast XANES spectra at ~150 fs resolution within minutes (Lemke *et al.*, 2013). A few hundred femtoseconds after excitation, the difference spectrum between excited and nonexcited sample solutions already showed the same characteristic shape for an elongation of the Fe-N bond distances as found in synchrotron studies after 100 ps. Measurement of a fixed-energy transient allowed, for the first time, to temporally resolve a direct structural signal representing the main structural reaction coordinate during the spin transition in $[Fe^{II}(bpy)_3]^{2+}$ (see Fig. 33). Spectra taken at the shortest time delay showed an indication of a signal similar to a shift of the absorption edge toward higher energy. Such an increase of the ionization energy is compatible with the transfer of negative charge from the iron atom and was therefore a first indication of the MLCT state in $[Fe^{II}(bpy)_3]^{2+}$.

A population of an intermediate triplet state predicted by theoretical models could not be distinguished from the HS state using XANES, because both states exhibit nearly the same structural change. A complementary technique to study electronic structure changes is XES. Here the incident x rays are tuned above the absorption threshold and create a core hole. Spectral changes of the subsequent fluorescence x rays emitted after electrons from occupied orbitals fill this core hole are measured with high resolution. Characterization of the HOMO can be achieved either directly, by measuring transition from electrons in HOMO states or indirectly, through the exchange interaction of core and HOMO electrons (see Fig. 32).

The ultrafast electronic transitions in $[Fe^{II}(bpy)_3]^{2+}$ were studied measuring the entire $K\beta_{1,3}$ emission line of a $[Fe^{II}(bpy)_3]^{2+}$ solution with a dispersive von Hámos spectrometer (von Hámos, 1933; Alonso-Mori *et al.*, 2012a, 2012b) as a function of the delay between an optical-laser pulse, initiating the spin crossover process, and the x-ray pulse, creating core holes at the iron site (Fig. 32). The $K\beta_{1,3}$ line shape reflects the Fe $3d$-electron spin state through interaction of $3d$ and $3p$ electrons (Glatzel and Bergmann, 2005) as well as the chemical configuration (Lee *et al.*, 2010). The transient combinations of spin states can therefore be interpreted by ground-state reference spectra of compounds with a similar chemical coordination and varying spin state. Different kinetic models using these ground-state spectra, the MLCT state, as well as the ^3T and T HS states, were fitted to the pump–probe time-delay-sorted $K\beta_{1,3}$ data and tested for compatibility (see Fig. 33).

The transient changes at some emission energies do not resolve the ambiguity between the two expected spin states, as the reference spectra show similar features at those energies [Fig. 33(a)]. Regarding the small region around 7054 eV, however, a significant difference appears when allowing the

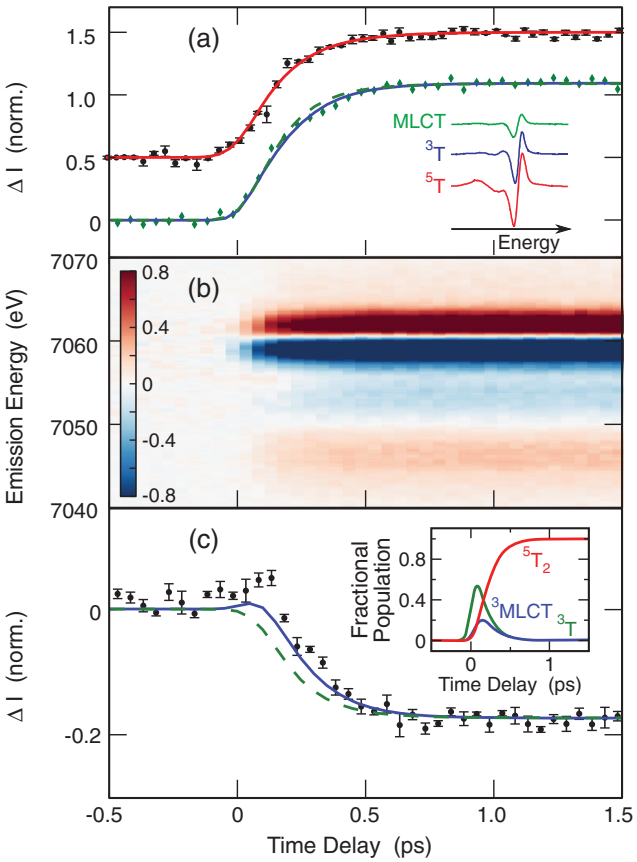

FIG. 33. Spectroscopic pump-probe results from the photoexcited spin transition of $[Fe^{II}(bpy)_3]^{2+}$ in solution. The increased iron-to-ligand distance is tracked by the XANES trace at 7125 eV [(a), black symbols, vertically offset by 0.5]. The structural HS rise time has been fitted by an exponential rise of 162 ± 6 fs (red) (Lemke *et al.*, 2013). (b) Time-dependent $K\beta$ emission difference spectra. The transient traces at 7061 and 7054 eV have been extracted [(a) green diamond symbols and (c) black symbols, respectively]. The data have been overlaid with results from global fits, including (blue lines) and excluding (green dashed lines) population of an intermediate ^3T triplet ligand field state. Adapted from Zhang *et al.*, 2014.

model to populate an intermediate ^3T state. The XES measurements represented are therefore one of the first experimental indications for the existence of the theoretically predicted (Graaf and Sousa, 2011; Sousa *et al.*, 2013) and debated (Bressler *et al.*, 2009) ^3T state.

Detailed information about chemical transitions between the HOMO and LUMO levels can be obtained by measuring emission spectra as a function of x-ray excitation into specific electronic states, a technique commonly referred to as resonant inelastic x-ray scattering (RIXS). In an optical pump-x-ray probe experiment, time-resolved RIXS maps at the iron L_3 edge (710 eV) were measured, revealing electronic configuration details during the photolysis of $Fe(CO)_5$ into $Fe(CO)_4$ and CO (Wernet *et al.*, 2015).

Because of the relatively strong interaction of the soft x-ray probe with matter at 710 eV, the sample solution was delivered as a 20-μm-diameter liquid jet into a vacuum chamber for the interaction with the pump and probe pulses. In $Fe(CO)_5$,

similar to the case of the $[Fe^{II}(bpy)_3]^{2+}$ complex, different electronic transitions within 3*d* levels are triggered after initial optical excitation from a 3*d* into an antibonding $2\pi^*$ state. The different transitions give rise to characteristic peaks in the RIXS map, which represents the intensity distribution of the energy transfer—the difference of incident and emission energy—as a function of the incident energy. The pump-probe difference RIXS map, showing the light-induced changes, was separated into four regions in the energy transfer plane [Fig. 34(b)]. The expected states of excited $Fe(CO)_5$ and the photoproduct $Fe(CO)_4$ contribute to those regions in varying distributions. Scaling those expected contributions with different kinetic models of the transient process allows one to simulate the transient signals for different models and compare them to the experimental result [Fig. 34(c)]. After photodissociation, which happens faster than can be measured with the current experimental time resolution, a relaxation of the photoproduct $Fe(CO)_4$ into both a triplet state and a ligated structure with an ethanol solvent molecule shows good agreement with the data.

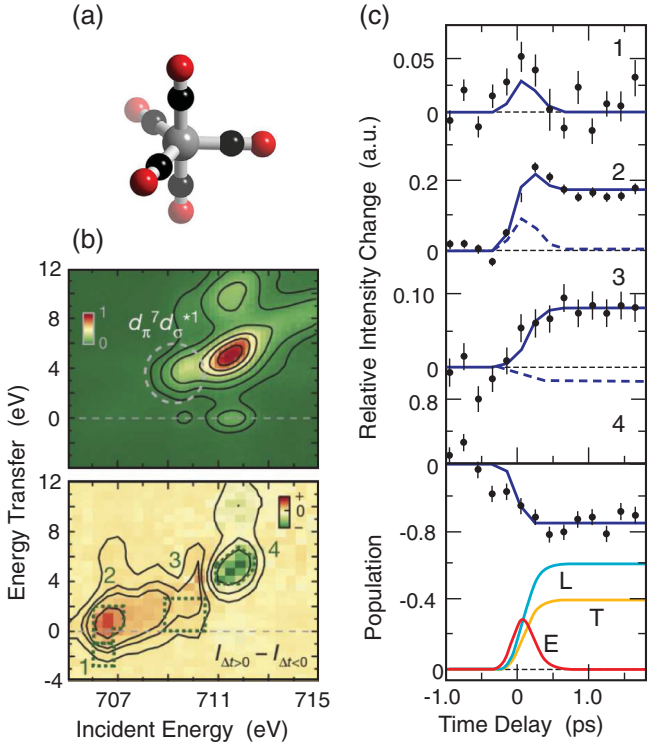

FIG. 34. Time-resolved studies of the photolysis of $Fe(CO)_5$. (a) Chemical structure of $Fe(CO)_5$; (b) ground-state and difference RIXS map between the integrated measurements after 266 nm excitation of $Fe(CO)_5$ solution ethanol and the ground-state map. The transient intensities in the regions labeled in 1–4 [black dot symbols in (c)] have been modeled using a kinetic model using different potential electronic transition states [solid blue lines in (c)]. The result of the global fit is shown in the bottom panel of (c). The compatible model includes an excited (*E*), triplet (*T*), and ethanol ligated (*L*) $Fe(CO)_4$ fragment population. Simulated signals excluding a triplet and a ligated population are indicated by dashed lines in panels 2 and 3. Adapted from Wernet *et al.*, 2015.

Technical applications of light-induced charge-transfer states in transition metals convert the optically generated energy into electrical potential by transferring charge to the conduction band of a chemically bound semiconductor (O'Regan and Grätzel, 1991). The electronic states participating in this process include shared states generated by interfacing the transition-metal complex with the crystalline material. A ruthenium-based model system bound to ZnO nanoparticles has been investigated using element-specific photoelectron spectroscopy (PES) from ruthenium inner-shell electrons (Siefermann *et al.*, 2014), also discussed in Sec. IV.B.2 with regard to interfacial phenomena in materials. The energy spectrum of electrons excited above the ionization potential contains information about the chemical potential and the local structure. Comparing the PES signal, at a 500 fs delay with respect to the optical excitation, with DFT calculations indicates the existence of an interfacial charge-transfer state between the photosensitive complex and the nanoparticle. Such local electronic information of functional entities helps to solve long-standing questions about charge-transfer mechanisms in novel solar energy conversion materials (Siefermann *et al.*, 2014).

As presaged in Sec. IV.A, the assumptions in traditional core-electron spectroscopy can be violated at FEL sources. In an XES study performed with 550 eV x rays on liquid water, a strong dependence upon the incident fluence was observed (Schreck *et al.*, 2014). By studying the spectral response of the system over a range of x-ray fluences from 0.1 to 19.8 J/cm^2, it was demonstrated that the x-ray emission spectrum is significantly distorted and the total emission yield decreased compared to results obtained at a storage ring source. As such, femtochemistry with high-fluence x-ray FEL pulses that are longer than the core-hole lifetime will need to consider these effects while analyzing x-ray emission data; see Sec. IV.A.

b. Chemisorption on solid surfaces

Chemisorption of molecules on solid surfaces is of high relevance for applications in catalysis and energy storage. An understanding of the stochastic and ultrafast adsorption and desorption mechanisms can help to tune the binding energy and molecule mobility on the surface, which determines their functionality as catalysts.

Changes to the bond formed by CO molecules on a ruthenium surface [Ru(0001)] induced by an optically excited temperature spike in the substrate were observed by ultrafast x-ray absorption spectroscopy (XAS) and XES measurements, revealing dynamics of the electronic structure of CO (Dell'Angela *et al.*, 2013). The characteristic LUMO and HOMO spectra measured after 12 ps (see Fig. 35) resemble a linear combination of those for chemisorbed and gas-phase CO.

A fraction of about 30% of the molecules were promoted to a transient, weaker bound precursor state by phonons from the substrate prior to desorption. Such a mechanism had been proposed as a prerequisite for time-reversed chemisorption, or desorption, that allows the molecule to lose rotational and translation energy before forming a bond to the surface. This first experimental evidence was further confirmed by density functional theory modeling combined with simulations of the

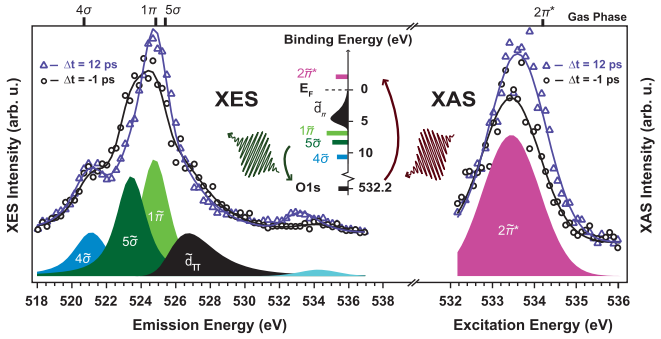

FIG. 35. Oxygen *K*-edge x-ray emission spectroscopy (left) and x-ray absorption spectroscopy (right) data of CO/Ru(0001) with corresponding fits (solid lines) for both before the excitation and for 12 ps afterward. At the bottom, the peak deconvolution resulting from the fit of the spectra is shown, with the elastic peak being indicated in light blue around 534 eV. (Middle) A schematic illustration of the excitation process from the O1*s* level to the unoccupied $2\tilde{\pi}^*$ resonance in XAS and the core-hole decay process from occupied molecular orbitals back to the O1*s* in XES. From Dell'Angela *et al.*, 2013.

experimental data (Öberg *et al.*, 2015). The simulations of the transient potential energy after substrate heating demonstrated an entropic barrier between adsorbed and precursor states of CO that can be overcome in the experimental conditions used.

The electronic changes within the first picosecond after excitation were studied in a dedicated experiment to provide further detail (Beye *et al.*, 2013a). A rapid increase in bond length could be shown, which occurred faster than the transition to the precursor state. Measuring the content of transient species as a function of excitation fluence showed they exist simultaneously by comparison to *ab initio* molecular dynamics simulations of CO adsorbed on Ru(0001). In an extension of the this study aimed at detecting and understanding the precursor state of the carbon monoxide interaction with the Ru surface, the electronic structure of a transition state during the oxidation step of the same laser-pulse-initiated reaction was studied (Ostrom *et al.*, 2015). On a time scale of 800 fs, the optical-laser pulse excites the motion of both CO and oxygen molecules on the surface, inducing collisions of the reactants and producing new electronic states in the O *K*-edge x-ray absorption spectrum. These new states depict the existence of new adsorbed species that resemble neither of the initial reactants adsorbed on the Ru surface. Density functional theory calculations indicate that these result from changes in the adsorption site and bond formation between CO and O with a distribution of OC-O bond lengths close to the transition state (Ostrom *et al.*, 2015). From the computed potential energy surface for the reaction, these fragments can be identified as molecular species present in the transition state region while attempting to form CO_2. Based on a simple quantum oscillator model, a probability analysis is provided that rationalizes the ~10% population of species in this region that was measured during the first few ps in the experiment.

The relative impact of CO desorption mediated by either a precursor state or the interaction with co-adsorbed oxygen was studied by time-resolved XAS. Comparison with density functional theory and *ab initio* molecular dynamics calculations showed that the direct pathway via oxygen outweighs the precursor-mediated pathway found on bare Ru(0001) (Xin *et al.*, 2015), demonstrating the catalytic effect of surface oxidation on the desorption mechanism.

c. Transient nuclear structure studied by diffuse scattering

The spectroscopic methods discussed previously represent local, element-specific probes of electronic and nuclear structure after stimulation. The transient global nuclear structure of excited molecules can be measured through elastic diffuse x-ray scattering, which represents the Fourier transform of the pair distribution function in the sample volume. The diffuse scattering information cannot be inverted to a three-dimensional structure. However, transient structural changes can be identified through comparison with simulated scattering data.

With the bright pulses from LCLS, enough scattering signal from gas-phase molecules can be collected and structural changes on the femtosecond time scale can be followed (also cf. Sec. IV.A.4). This overcomes a limitation of electron diffraction, which has a larger scattering cross section than x rays but physically limited electron pulse length by space charge effects. The structures during ring opening of 1,3-cyclohexadiene upon excitation with 270 nm light were measured in a gas cell on the sub-100-fs time scale (Minitti *et al.*, 2015a). With the exclusively intramolecular interactions in the gas phase, *ab initio* calculation of different excited electronic states and their influence to the nuclear structure at relatively high precision become possible. Various possible trajectories of probable molecular motion were simulated for 1,3-cyclohexadiene and compared to the experimental data. A good agreement with the data was found for a combination of dissociating trajectories together with a component where the molecule relaxes back into the bound ring form under molecular vibrations with a 60 fs period, close to the temporal resolution limit in the experiment.

2. Structure and dynamics of soft and disordered matter

Experimental insight into the equilibrium dynamics of soft and disordered matter represents an experimental challenge due to the coexistence of a large number of very different intermolecular arrangements. These systems can exhibit macroscopic behavior that requires an understanding of the behavior of multiple internal structures, each of which can be composed of various atomic and molecular constituents of the material. This medium-range order is traditionally difficult to measure, but the properties that it imparts to the material are of fundamental importance.

A canonical system for the study of structure-function relationships in disordered materials is that of liquid water. The anomalous thermodynamic properties of water remain the subject of much debate and a study performed at LCLS was aimed at investigating the structure of liquid water below the homogeneous nucleation temperature of 232 K (Sellberg *et al.*, 2014). In this example, water droplets were introduced into a vacuum system and allowed to evaporatively cool before interacting with the x-ray FEL pulse. The diffuse scattering of the supercooled droplet was measured on a 2D

detector. The diffuse scattering curves show an increase of order even below the nucleation temperature that appears to approach both experimentally measured amorphous and crystalline ice structures (Fig. 36). Comparison with molecular simulations showed that the structure at the low temperatures has a much stronger tetrahedral ordering compared to water at ambient conditions.

Other important disordered systems are polymers, for which applications are abundant in everyday technological devices. Whether interacting with other polymer chains or other chemical compounds, polymers self-organize in diverse morphologies and exhibit a rich diversity of mesoscale and hierarchical structures. The common polymer polystyrene has been used by Carnis *et al.* (2014) as an example. X-ray photon correlation spectroscopy (XPCS) is used to study dynamics and can provide high-spatial-resolution information. The goal was to measure the temperature dependence of the relaxation dynamics of an entangled polystyrene polymer melt, while evaluating the accuracy of the result gained in the potentially damaging x-ray FEL beam. The sample consisted of gold nanoparticles, grafted with polystyrene, which were dispersed in a polystyrene homopolymer matrix. The nanoparticles are used as dynamic tracers and are small (i.e., 5.5 nm diameter) so as to not perturb the dynamics of the matrix, while enhancing the signal from the sample. At a sample temperature of 380 K, the dynamics are much slower than the time structure of LCLS (i.e., 8.3 ms).

Time-resolved coherent diffraction patterns were recorded on a two-dimensional detector. A detailed analysis of the recorded frames allowed for characterization of the dynamics of the sample and confirmed what had been observed with other techniques at storage ring sources. The characteristic relaxation time shows a linear behavior as a function of the wave vector transfer, down to length scales of about 10 nm. The sample also clearly showed indications of aging, which is observed by a change in the characteristic relaxation time of the system as a function of measurement time.

The thermodynamics of disordered materials can often lead to a "glassy state" of the material. This state of matter, in terms of structure, can hardly be distinguished from the liquid state and resembles an amorphous solid. Once in the glassy state, the dynamics is extremely slow and can therefore be probed as in the previous example with XPCS. An experiment at LCLS demonstrated that it is indeed possible to properly characterize the coherent diffraction pattern of a disordered system from a single shot with atomic resolution (Hruszkewycz *et al.*, 2012). Most importantly, it showed that the energy deposited in the system from that single shot does not perturb the system. This was an important experimental confirmation. This kind of technical development will allow for measurements of ultrafast dynamics in disordered systems down to the atomic scale.

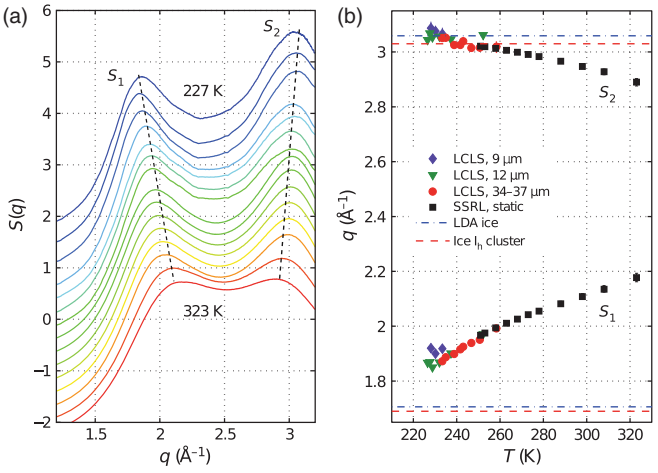

FIG. 36. (a) Diffuse scattering profiles of metastable water, measured at different temperatures. The nine lowest temperature curves were measured using ultrafast pulses from LCLS before nucleation of ice. (b) The increasing separation of the two peaks labeled S_1 and S_2, which approaches order peaks of low-density amorphous ice (LDA, dash-dotted blue lines) as well as hexagonal ice (ice I_h, red dashed lines). From Sellberg *et al.*, 2014.

3. Perspectives

Various experiments have shown that LCLS can contribute important information to the understanding of amorphous and disordered systems by acquiring local and global snapshots of electronic and nuclear structures during ultrafast processes. Higher-order spectroscopic methods like RIXS, XES, and PES suffer from low signal yield despite the high pulse energy at LCLS and are therefore still challenging to apply in some cases. Those techniques will significantly benefit from the higher average x-ray flux provided through a high pulse rate by LCLS-II (Sec. V.B) and will become much more important in the future for answering questions about ultrafast changes of electronic structure. X-ray scattering in combination with calculations can yield the nuclear structure of samples during a chemical reaction. Already demonstrated in the gas phase, the method can be extended to molecular systems in solution thanks to the recent improvements in detector technology and data analysis. FEL solution scattering is on the verge of revealing new experimental insight into the molecular dynamics and solvent interaction on the femtosecond time scale. Challenging technical developments have allowed proof-of-principle measurements of the global structure of disordered materials using x-ray correlation spectroscopy. Once these are overcome, new insights into the ultrafast equilibrium dynamics of liquids can be expected. Additionally, the new high-repetition-rate FEL sources like the European XFEL and LCLS-II will provide the capability of measuring dynamics at time scales not previously available with low repetition rate FELs (typically between 100 ns and 10 ms) thanks to their unique pulse structure.

E. Biology

Biology has been an area of intense effort and technical development at LCLS. The facility offers unique possibilities for biological research that have been explored via technology and technique development, leading to recent scientific discovery. Tools are now available that make use of the short pulses to reduce, and possibly overcome, radiation damage limitations using the diffraction-before-destruction method described in Sec. III.B.1. Given the sensitivity of biological samples to radiation damage, overcoming its effects is a key

contribution of x-ray FELs to life sciences. As a result, many of the biologically motivated studies at LCLS are also closely related to investigations about fundamental physical processes during the intense x-ray–matter interaction which are the focus of Secs. IV.A and IV.C.

The instantaneous nature of the single-pulse measurements allows the study of samples at ambient temperatures, closer to the natural conditions of living organisms, and removes the need for the cryocooling often used when studying biological samples with a continuous x-ray beam or in cryoelectron microscopy. The combination of room-temperature capabilities and snapshot, instantaneous data collection has enabled the study of dynamics in biological samples with high temporal resolution, ultimately limited by the x-ray pulse duration.

This section will review the developments in biological studies and the unique capabilities afforded by LCLS, including serial femtosecond crystallography (SFX). A brief summary of the LCLS-based milestones of this technique and the opportunities it presents for scientific discovery will be discussed with results on new structures, access to different types of samples, and the broadening impact LCLS is having on membrane protein studies. A review of results on dynamic studies of biomolecules will follow.

SFX and other structural biology techniques at LCLS are still very much under development, and therefore a large fraction of the published literature in the field pertains to developments and improvements of the methodology. A review of the existing challenges to making femtosecond crystallography broadly usable will be presented, highlighting recent efforts to address these.

Finally, technique development studies and recent results toward single-particle imaging will be presented. The primary emphasis will be in methodology developments aimed at building these methods into usable tools for the wide range of biological samples.

1. Serial femtosecond crystallography

From the initial conception of LCLS, very small, potentially nanometer-scale, crystals of proteins have been identified as a type of sample where the facility's strengths could be brought to bear on significant scientific problems impacting human health. Through a concerted effort between the facility and its users, rapid development has led to what is now broadly known as serial femtosecond crystallography, a technique for structural analysis of protein crystals potentially as small as a few unit cells.

a. First structural biology experiment at LCLS

The first biological experiments at LCLS aimed to demonstrate the ability of ultrashort x-ray pulses to obtain interpretable diffraction data for very small samples that are typically inaccessible to studies with synchrotron radiation. Crystals of a protein were selected as the best candidate sample due to their constituent periodic arrangement of identical molecules, which gives rise to a significant enhancement of the diffracted intensity at periodic points in reciprocal space, so-called Bragg peaks. The results showed that crystals as small as 200 nm could produce measurable and interpretable diffraction patterns, which were used to generate an electron density map of the molecule of interest (Chapman *et al.*, 2011). Information could be extracted from the data despite a total integrated dose to each crystal as high as 700 MGy, which exceeds the safe dose for data collection using cryocooled crystals at a continuous x-ray source by a factor of more than 30 (Owen, Rudio-Piera, and Garman, 2006). In this particular case, the molecule was photosystem I, a very large membrane protein with a known structure. Comparison of the known structure to the LCLS results showed agreement to within the accuracy of the measurement.

The x-ray beam at the time of this experiment could be used only in the soft x-ray spectral range, below 2 keV. This is not the most suitable range of photon energy for crystallographic techniques, where a resolution of 3 Å or better is typically desired. The available photon energy limited the achievable resolution to 8.5 Å. Nevertheless, a few important conclusions about radiation damage and data analysis could be drawn. These drove the growth of the method to study a wide range of samples, as well as a vigorous effort in technology and methodology development for the following five years, making SFX a widely used technique today.

b. Development of high-resolution techniques

Once hard x-ray instruments became available in 2010, similar experiments were repeated using photon energies capable of producing high-resolution diffraction. A high-resolution structure of a model protein, in this case lysozyme from hen egg white, was obtained from over 10 000 indexed diffraction patterns from individual crystals (Boutet *et al.*, 2012). Two data sets were collected using 40 and 5 fs pulse duration, and these were compared to a low-dose (24 kGy) conventional data set collected at room temperature and known to be free of radiation damage. A thorough comparison between the data sets revealed no significant radiation damage for the LCLS-obtained structures, even at the highest resolution of 1.9 Å. The dose to each crystal in this particular study was estimated to be 33 MGy, roughly the same as the generally accepted dose limit to cryocooled crystals at a synchrotron source. However, the LCLS results were obtained on room-temperature crystals flowing in a liquid stream, and such a dose greatly exceeds the safe room-temperature dose at a conventional x-ray source.

c. First novel biological science

It was not long after the initial demonstration of the high-resolution capabilities of the SFX technique that it was used to obtain new biological information. The first such result was obtained for the Cathepsin B protease (TbCatB) from the parasite causing African sleeping sickness: *Trypanosoma brucei*. SFX was combined with *in vivo* crystallization to allow the study of the natively inhibited state of the TbCatB molecule in its fully glycosolated form. The structure was refined to 2.1 Å and revealed the presence of a bound propeptide, as well as two carbohydrates with well-defined densities (Redecke *et al.*, 2013). Analysis of the structure suggests how the propeptide, which is not present in the mature structure of TbCatB, inhibits the activity of the molecule. Structural details reveal differences between the mature and natively inhibited structures that can be interpreted

to suggest potential avenues to disable TbCatB and provide potential targets for drug design.

d. In vivo structural studies

The tightly focused and extremely intense LCLS beam provides unique opportunities to study samples from which it was not previously possible, or at least very challenging, to obtain structural information. Of particular interest are the developments in the use of *in vivo* crystallization that led to new structural insight in TbCatB (Koopmann *et al.*, 2012; Redecke *et al.*, 2013). In these studies, the *in vivo* grown crystals were extracted from their host cells prior to the measurement. This particular case produced clear differences between the structure obtained from the *in vivo* grown crystals and from crystallizing extracted material.

More recently, a separate study went a step further by studying crystals still inside living cells (Sawaya *et al.*, 2014). It showed that the Cry3A toxin that naturally crystallizes within *Bacillus thuringiensis* cells yielded an essentially identical structure to the extracted and recrystallized protein. *In vivo* structural studies with intrinsically small crystals could become an important use of x-ray FELs, enabling atomic-level structural studies (Duszenko *et al.*, 2015).

2. Novel structural biology

a. Membrane proteins

Membrane proteins are found in the lipid bilayers of living cells. They often have roles in communication between the interior of cells and the rest of the organism and perform a wide variety of roles critical to the proper functioning of living metabolisms. Their natural state, embedded in a lipidic membrane, makes them primarily hydrophobic and typically rather insoluble in water. This causes significant difficulties in extracting, purifying, and crystallizing most membrane proteins, which often limits the availability of large, high-quality crystals. The resultant crystals are likely to be at or below the size that can be used at synchrotron sources, a problem that is exacerbated if one wishes to perform a room-temperature measurement (Carpenter *et al.*, 2008). The majority of membrane proteins are particularly fragile and radiation sensitive. These considerations make LCLS a very useful tool for structural studies of membrane proteins.

A large effort has led to a number of published works on membrane proteins. The very first SFX results published were from studies on photosystem I, a very large membrane protein (Chapman *et al.*, 2011). This work was the beginning of a large effort surrounding photosynthetic and photoactive proteins that will be discussed further in Sec. IV.E.3 on dynamics in biological systems.

b. G-protein-coupled receptors

Activities in structure determination of membrane proteins have focused on a specific type of membrane proteins called g-protein coupled receptors (GPCRs), which are eukaryote transmembrane proteins. They comprise a large class of extremely important molecules that represent ~40% of all drug targets today. They are notoriously difficult to crystallize, and in many cases only small crystals can be obtained, which has led to the relative paucity of known structures. LCLS provides a method to study these molecular structures by allowing smaller crystals to be studied in a near-native environment, i.e., at room temperature.

The first GPCR structure from LCLS was published in 2013 (Liu *et al.*, 2013). The results on the human 5-HT_{2B} receptor bound to the agonist ergotamine showed small but significant differences between the LCLS-obtained, room-temperature structure and the cryogenically cooled synchrotron structure. The structure obtained by SFX is believed to be a better representation of the native ensemble of conformations, more capable of revealing the dynamics that are integral to GPCR biology. Crystals with 2 orders of magnitude smaller volume were used to produce the SFX structure compared to the synchrotron structure, but yielded the same resolution in the final structure.

Activated GPCRs are desensitized via the binding of an arrestin molecule, which blocks interactions with g proteins. Essentially, g proteins activate GPCRs while arrestin stops their function. LCLS was a necessary tool to obtain the first-ever structure of a GPCR in complex with arrestin (Kang *et al.*, 2015). Small, radiation-sensitive crystals of a vision protein called rhodopsin in complex with arrestin provided only limited resolution using synchrotron sources. The LCLS data allowed the structure of the complex to be solved to 3.3 Å. The structure is shown in Fig. 37. The structure reveals how specific components of the rhodopsin molecule are employed to bind arrestin, including transmembrane helix 7 and helix 8. The results also demonstrate how a cleft is open in arrestin via a 20° rotation which can accommodate a short helix in rhodopsin.

c. Structure-based drug design

The study of GPCRs at room temperature has recently yielded a few structures of medically relevant molecules and complexes. The first example was a structural study of a receptor involved in pain regulation bound to a small peptide. This small peptide (DIPP-NH_2) has been shown to have dual capabilities. It can promote the production of natural peptides that reduce pain and are produced by the μ-opioid receptor (μ-OR). It can also inhibit the function of the δ-opioid receptor (δ-OR), involved in adverse tolerance and dependence effects

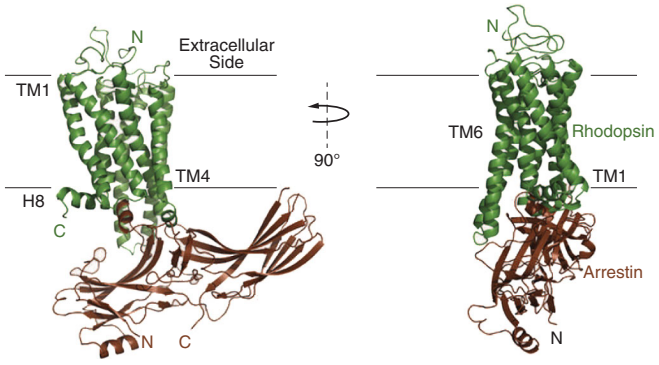

FIG. 37. Structure of rhodopsin in complex with arrestin. TM1TM7 indicates rhodopsin transmembrane helices 17; H8 is intracellular helix 8. Adapted from Kang *et al.*, 2015.

that occur with more traditional painkillers such as morphine. Compounds such as DIPP-NH_2 represent interesting avenues to pursue that could lead to novel pain management drugs with reduced tolerance and dependence concerns. The published work reveals the interactions between the δ-opioid receptor and the inhibiting peptide studied, contributing to a better understanding of the opioid-peptide interactions in general (Fenalti *et al.*, 2015).

A second example of a GPCR bound to a ligand was recently published (Zhang *et al.*, 2015). In this case, the ability of LCLS to obtain structural information from small crystals produced room-temperature structural detail of the angiotensin II type 1 receptor (AT_1R), a primary blood pressure regulating protein, bound to a selective antagonist called ZD7155. The structure, resolved to 2.9 Å, provides new insight on the structural features of AT_1R, and the understanding of the binding of the ligand interactions can be used to simulate the interactions of clinically used AT_1R blockers (ARBs) with AT_1R. This has the potential to provide a sound basis for structure-based drug design targeting AT_1R via improved understanding of its interactions with a specific model compound.

d. Neuroscience

The interaction between synaptotagmin-1 and the neuronal SNARE (soluble *n*-ethylmaleimide sensitive factor attachment protein receptor) complex was studied at a resolution of 3.5 Å (Zhou *et al.*, 2015). This interaction is critical in neurotransmitter release. A model of synaptic vesicle fusion has been proposed based on these results. Contrary to previously discussed results, a different data collection strategy was employed, utilizing not liquid flowing jets of crystals but a limited number of larger cryogenically frozen crystals (Sec. IV.E.4.b). The electron density maps obtained from LCLS were superior to what could previously be achieved at a synchrotron source by limiting radiation damage to Ca ions involved at the interface. The results are shown in Fig. 38.

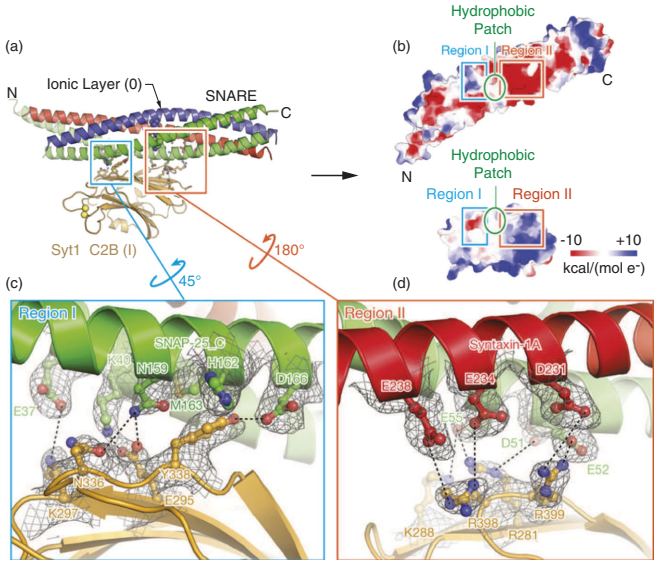

FIG. 38. Interface between synaptotagmin and the neuronal SNARE complex. (a) The primary interface along with interacting residues. (b) Electrostatic potential map of the primary interface shows how two polar regions I and II are connected by a hydrophobic patch (SNAP-25 I44, L47, and V48 and Syt1 V292, L294, and A402). (c), (d) Close-up views of regions I and II. Labels indicate interacting residues. Dashed lines indicate hydrogen bonds or salt bridges. 2 mF_o DF_c electron density maps of the interacting residues are superimposed (gray mesh; contour level = 1.5σ). Adapted from Zhou *et al.*, 2015.

3. Dynamics in biological systems

LCLS naturally provides the potential for exquisite time-resolved measurements, which makes its use for the study of dynamics in all fields of science obvious. This includes structural biology, where ultrafast energy capture and dissipation are involved in light absorption by photosensitive molecules. Studies on slower time scales can also make use of the diffraction-before-destruction method, which allows damage-free snapshot data collection and can enable the study of irreversible reactions.

a. The development of structural dynamics via SFX

The study of dynamics regularly involves a stimulus to initiate a reaction, typically an optical-laser pulse for ultrafast studies. Pump lasers provide the ideal stimulus for photoactive molecules and the study of photosynthesis. Time-resolved biological techniques are established at synchrotrons, and LCLS can push the limits of time resolution (Neutze and Moffat, 2012) and facilitate the study of radiation-sensitive metalloproteins (Kern, Yachandra, and Yano, 2015).

SFX has been the primary technique used to study light-driven dynamics in biology at LCLS, with a few preliminary studies published on the dark (no illumination) states of photosensitive molecules. Such studies are a critical prerequisite to successful time-resolved measurements. The dark state of the *Blastochloris viridis* photosynthetic reaction center was obtained first using soft x rays (Johansson *et al.*, 2012) and then using hard x rays to a resolution of 3.5 Å (Johansson *et al.*, 2013). The light-activated state was later studied via SFX and small-angle x-ray scattering (SAXS) and wide-angle x-ray scattering (WAXS). Dark state studies on photosystem II (Kern *et al.*, 2012) also set the stage for multiple efforts aimed at solving the mechanism of water splitting.

The first study to show that a clear change in structure factors could be observed upon excitation with optical light in a SFX experiment was performed on a complex of photosystem I and ferredoxin (Aquila *et al.*, 2012). Photon capture in this system is known to lead to electron transfer from photosystem I to ferredoxin with microsecond-scale kinetics leading to the undocking of ferredoxin and a large rearrangement in the crystal unit cell that causes the collapse of the crystal. Structure factors were observed to change with delays of 5 and 10 μs but no electron density map was recovered. This demonstration set the stage for future dynamics studies and represents a biological test case for the probing of irreversible structural changes.

The structure of the photoactive yellow protein (PYP), a blue light receptor from bacteria, was solved at high resolution using nanosecond pulses with a wavelength of 450 nm to initiate the PYP photocyle (Tenboer *et al.*, 2014). The PYP

photocycle is well known from synchrotron and other studies on the nanosecond or slower time scales, with multiple intermediate states revealed by spectroscopy and diffraction studies. A direct comparison between the SFX-obtained and synchrotron structures confirmed the ability of time-resolved SFX to obtain high-resolution 1.6 Å (in this case) structural dynamics information. Difference electron density maps between the illuminated and dark states show strong peaks indicative of large-scale motion consistent with synchrotron results. Improved signal levels are seen compared to synchrotron data, likely due to the fact that LCLS can use smaller crystals with more uniform photoabsorption, allowing more molecules to enter the photocycle. The larger crystals used at a synchrotron are optically opaque to the laser light, leading to nonuniform illumination that does not penetrate the entire sample. Also, repeated laser illumination causes strain in the crystal that limits the maximum laser power that can be used. Discarding each crystal after one pulse using the SFX technique removes these limitations.

This proof-of-principle demonstration achieved time resolutions possible at conventional x-ray sources and reproduced existing results. However, LCLS offers the possibility of time resolution 1000 times faster than other light sources due to the short x-ray pulses. This new time regime was successfully accessed in a study of carbonmonoxy-myoglobin (MbCO). A 532 nm wavelength laser of 150 fs duration was used to dissociate a CO molecule bound to an iron atom in the heme of myoglobin. It was previously known from other studies that the CO unbinds very rapidly, but no direct observation of the dynamics via crystallography were previously possible. The results in Fig. 39 show the ultrafast release of the CO molecule after laser illumination followed by the collective motion of the rest of the molecule in response to the bond breaking releasing the CO (Barends *et al.*, 2015b). These results demonstrate that ultrafast time-resolved crystallography at FELs is a reality. The ultrafast response of MbCO was also studied via small-angle scattering and spectroscopic techniques as will be discussed in Secs. IV.E.3.b and IV.E.3.c. The results indicate an immediate collective response of the protein upon ligand dissociation via the coupling of vibrational modes of the heme to global modes of the protein.

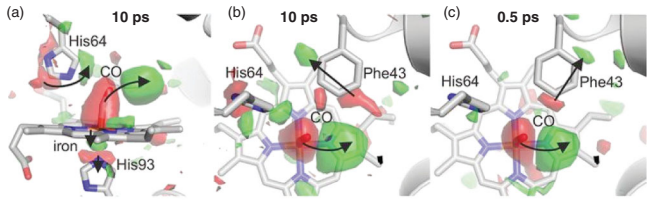

FIG. 39. Difference electron density maps [F(light)–F(dark)] in pump-probe time-resolved serial femtosecond crystallography on carbonmonoxy-myoglobin (MbCO). (a) Results at time delay of 10 ps showing the bound (3σ contour level, red) and photodissociated ($+3\sigma$, contour level green) CO, the doming of the heme, the out-of-plane movement of the iron, and the associated movement of Histidine 93 (His93) away from the heme. Also shown is the rotation of Histidine 64 (His64) and the movement of Phenylalanine 43 (Phe43). (b) Same as (a) rotated by 90°. (c) Same as (b) but for a time delay of 0.5 ps. Adapted from Barends *et al.*, 2015b.

On slower time scales, recent work focused on photosystem II (PSII), which catalyses the splitting of water via the sequential absorption of four photons. This process leads to the release of oxygen in plant and bacterial life, ultimately maintaining the life-supporting oxygen level in the Earth's atmosphere. Multiple laser flashes can be used to advance the oxygen-evolving complex of PSII through the different states of the water-splitting cycle.

Two competing studies approached the question using different laser illumination strategies. One study reports that the Mn_4CaO_5 cluster of the oxygen-evolving complex undergoes an observable conformational change after double laser excitation (Kupitz *et al.*, 2014a). The second study, using a different laser illumination scheme, found no evidence of structural changes in the twice-illuminated state at the achieved resolution (Kern *et al.*, 2014). The differences in the illumination schemes and data processing between the two studies make it difficult to objectively compare the results, but their conclusions seem to be contradictory and subject to debate in the community. Further investigation is necessary to fully understand the mechanism of water splitting in PSII.

b. Spectroscopic techniques

The use of multiple simultaneous techniques is prevalent at LCLS, and structural biology is a field moving toward the use of complementary techniques to solve challenging problems. Studies on photosystem II have combined the simultaneous use of x-ray diffraction and x-ray emission spectroscopy (XES). The x-ray diffraction measurement provides direct structural information while the XES reveals the electronic states of particularly important elements in the sample (Alonso-Mori *et al.*, 2012a; Kern *et al.*, 2013). The XES measurements provide a direct indication of the oxidation state of the Mn atoms in the Mn_4CaO_5 cluster, providing a tool to simultaneously determine whether the x-ray beam damages the manganese cluster and demonstrate the advancement of the sample through the photocycle (Kern *et al.*, 2014). Figure 40 shows the Mn $K\beta$ emission spectra measured for doubly illuminated and triply illuminated PSII solution. A shift in the spectrum is seen for the triply illuminated data set with the longer delay ($3F$), and the spectral shifts can be interpreted based on previous knowledge from synchrotron studies to estimate the population of the states in the photocycle.

With simultaneous data collection, the emission spectrum can be extracted for only the pulses containing good crystal hits identified from the diffraction signal. This should make it possible to unambiguously correlate the electronic state of the Mn_4CaO_5 corresponding to any electron density map obtained from crystal diffraction. It is expected that the use of such simultaneous, or even coincident (Sec. IV.A.4.a) techniques, will become more prevalent in structural biological studies at LCLS to better understand the condition or state of the sample under investigation.

Besides the K edge, other emission lines can be used in XES studies. L edges, for example, are more sensitive to the Mn oxidation state and can provide more detailed information

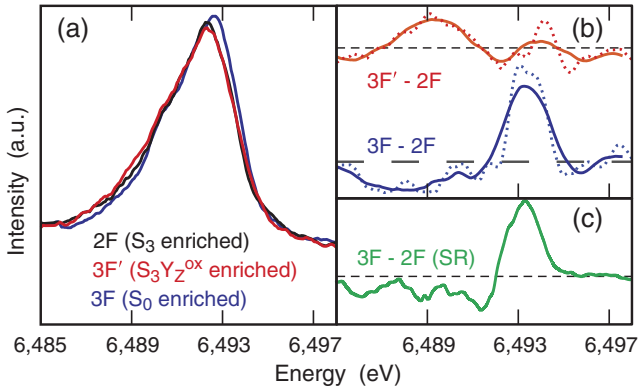

FIG. 40. $K\beta$ x-ray emission in photosystem II (PSII). (a) X-ray emission spectra collected on PSII solution for the doubly illuminated state ($2F$ in black), triply illuminated state after 250 μs delay ($3F'$ in red) and triply illuminated state after 0.5 s delay ($3F$ in blue). (b) Difference between the LCLS-collected $3F$ and $2F$ spectra. (c) Difference between the $3F$ (LCLS) and $2F$ spectra collected at a synchrotron source at 15 K. The similarities between the LCLS and synchrotron results indicate that a similar electronic state of the manganese cluster is being probed in both cases. Adapted from Kern *et al.*, 2014.

than K edges. A preliminary L-edge XES study has been published (Mitzner *et al.*, 2013).

X-ray absorption spectroscopy can also be used to follow the dynamics of a sample after laser illumination. XAS measurements after photolysis of carbonmonoxy-myoglobin revealed a two-step process with a fast (70 fs) and a slow (400 fs) relaxation (Levantino, Lemke *et al.*, 2015). They interpreted their results as an indication that heme doming occurs during the faster step.

c. Time-resolved small-angle and wide-angle scattering

Solution scattering can be used in conjunction with modeling to extract biomolecular structural information. When combined with a pump laser, time-resolved small-angle x-ray scattering (TR-SAXS) or wide-angle x-ray scattering (TR-WAXS) can reveal the dynamics of samples without the need to crystallize them and with relatively simple sample preparation requirements. The same techniques can be used in stimulated dynamics in liquid solutions as described in the chemistry section of this article (Sec. IV.D.1).

TR-SAXS and TR-WAXS was used to visualize the hypothesized "protein quake" caused by light absorption in molecules on picosecond time scales (Arnlund *et al.*, 2014; Neutze, 2014). These results show that proteins can rapidly dissipate energy via an ultrafast global conformation change and that this occurs faster than the propagation of heat from the laser pulse to the sample. The TR-WAXS data were decomposed into solvent and molecule responses and modeling provided for a low-resolution time-resolved structure. The results were obtained in this case using fairly high laser intensity resulting in multiphoton absorption for each molecule, leading to uncertainty about the biological relevance of the dynamics obtained.

Another study demonstrated the existence of the protein quake in carbonmonoxy-myoglobin, in this case with single-photon absorption leading to the dissociation of CO from the heme in myoglobin (Levantino, Schiro *et al.*, 2015). This study showed that perturbations at the active site can propagate at the acoustic speed of sound to the global protein structure. Oscillatory, collective motion damped in a few picoseconds was revealed via the analysis of the time-resolved radius of gyration and volume of myoglobin. The results are surprising considering that modeling of the system predicted overdamped motion, which should have damped away the observed oscillatory behavior. The interpreted TR-SAXS and TR-WAXS data show a clear time evolution and oscillations in Fig. 41.

4. Crystallography challenges and technique development

Despite its success, the liquid jet-based SFX technique was from the start, and still is, faced with significant challenges that limit either its applicability or capabilities and, in some cases, preclude its use completely. The technical challenges involved have given rise to multidirectional efforts that have spawned a host of scientific publications aimed at technique development and improvement, as well as a deeper understanding of the fundamental capabilities and limitations. While less about scientific discovery, these efforts in crystallography method development are important for future scientific progress at LCLS and will be reviewed here by looking at specific challenges and the progress to date in overcoming them.

a. Sample quantity and consumption

In the early days of SFX, the sample delivery system of choice was a gas dynamic virtual nozzle (GDVN) (DePonte *et al.*, 2008; Weierstall, Spence, and Doak, 2012). These are primarily suitable for low-viscosity samples and soluble

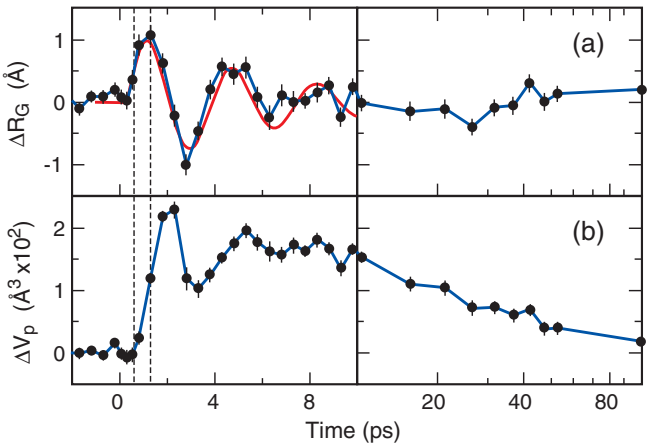

FIG. 41. Time-resolved structural changes in CO:myoglobin. (a) Damped oscillatory behavior of the radius of gyration (ΔR_G) showing a 1 Å increase in 1 ps measured in carbonmonoxy-myoglobin (MbCO) after laser excitation. (b) Time evolution of the volume (ΔV_p) of the molecule after laser excitation showing a delayed response of the volume compared to the radius of gyration. This delayed response indicates an ultrafast redistribution of the mass toward the outside solvent from the active site, verifying the existence of the protein quake. Adapted from Levantino, Schiro *et al.*, 2015.

macromolecules, leading to typically high flow rates of $10-20\ \mu l/\min$. With typical hit rates and indexing rates of 30% and <10%, respectively, and on the order of 10 000 or more indexed patterns used for a structural analysis (Boutet *et al.*, 2012; Redecke *et al.*, 2013), the sample quantities required can be very large—prohibitively so for proteins difficult to express, purify, or crystallize. A typical 4 μm diameter jet flows at >10 000 mm/s, or at the repetition rate of LCLS of 120 Hz, over 75 mm between pulses. Since the LCLS beam is almost always off, with x rays present at the interaction region only for ~50 fs, 120 times per second, the majority of the sample goes to waste by flowing past the interaction region while there are no x rays.

The fraction of the sample that is actually probed by the beam should ideally approach 1. That is, the sample should flow exactly 1 beam size between pulses. Such an ideal situation is not possible due to the high power of the beam, which damages and/or vaporizes a volume significantly larger than the beam size on every pulse. Therefore, time must be given for a sufficient length of the jet to flow into the interaction region between every pulse. This implies that there will always be parts of the sample not directly hit by the FEL beam but damaged by secondary events, and thus not usable for measurements, independent of the nature of the sample delivery technique used. The maximum fraction of a sample that can be probed will always be limited for a tightly focused x-ray beam due to the propagation of damage requiring space between shots.

There are three obvious ways to increase the hit fraction: increase the repetition rate of the machine, reduce the speed of the jet, or trigger the jets to pulse with the x-ray beam. All have the effect of reducing the amount of sample that flows between pulses. Increasing the repetition rate of LCLS, while feasible, is not a simple endeavor. The LCLS-II project may provide such an opportunity in the future (Sec. V). An easier pursuit is reducing the speed of the jet. Two such methods were demonstrated at LCLS: an electrostatically focused jet (Sierra *et al.*, 2012) and a gas-focused jet suitable for viscous media, originally developed for a lipidic cubic phase (LCP) (Weierstall *et al.*, 2014) sample carrying medium. LCP has been developed as a useful medium in which to grow membrane protein crystals, especially GPCRs. The use of this kind of jet has led to the ability to deliver GPCR crystals in their growth medium directly to the beam, at low flow rates compatible with the rarity of GPCRs. The LCP jet was also demonstrated to be a suitable carrier medium for soluble proteins, allowing for a reduced sample consumption (Fromme *et al.*, 2015). The same system can also be used with other carrier media such as agarose (Conrad *et al.*, 2015).

Other issues may exist with liquid jet sample delivery. A study combining cryoelectron microscopy (EM) and SFX with a liquid jet indicated that some damage may be occurring in fragile crystals during the delivery process (Stevenson *et al.*, 2014). Other sample reduction strategies have been explored and developed, all ultimately aimed at increasing the fraction of the sample that is actually hit by the beam, but some also aimed at treating the crystals more gently. Fixed-target approaches have been developed for in-vacuum operation (Hunter *et al.*, 2014). This particular development showed it was possible to use fast-moving stages to hit a fixed-mounted sample at 120 Hz. With high sample coverage on this mount, a high peak hit rate can be achieved—somewhat similar to fast-flowing liquid jet hit rates—while greatly increasing the fraction of the sample used. This study was, however, performed with an attenuated beam and it remains to be demonstrated that the damaging full power beam can be used at this rate without catastrophic failure of the sample mount. Multiple types of sample supports can be imagined and some have been tested (Feld *et al.*, 2015).

As a consequence of the development of fixed-target techniques, a parallel effort led to the demonstration of the feasibility of 2D crystallography at LCLS (Frank *et al.*, 2014; Pedrini *et al.*, 2014). While not related to the same issue of sample consumption, some of the same techniques are employed in 2D crystallography. The resolution achieved to date is less than that attained using cryo-EM. The reason for this is under investigation, with radiation damage induced by the supporting film as a possible culprit. These results represent the first-ever 2D protein crystal diffraction patterns yielding a structure using x rays.

b. Atmospheric pressure operation

For larger crystals, where the removal of all air scatter by use of a vacuum environment may not be necessary, atmospheric pressure approaches have been pursued. Goniometer systems highly similar to synchrotron macromolecular crystallography (MX) beam lines can be used with sample scanning. Such techniques have been used at LCLS, as well as at SACLA in Japan, where damage-free structures of highly radiation-sensitive metal-containing proteins, bovine cytochrome c oxidase (Hirata *et al.*, 2014), and photosystem II (Suga *et al.*, 2015) were obtained at 1.9 and 1.95 Å, respectively. In these studies, large crystals were used and multiple shots taken at different positions on the same crystal, allowing the relative orientation of each shot to be known, a significant advantage over liquid jet approaches where the orientation of each shot is random and *a priori* unknown. The results showed that a significant area of the crystal ($20 \times 20\ \mu m^2$) is damaged by the pulse even with a $1.8 \times 1.2\ \mu m^2$ beam. A total of 1107 exposures were used for analysis from 76 different crystals in the bovine cytochrome c oxidase study while two data sets were collected for PSII, using 254 and 82 crystals, respectively, to collect 5592 and 2058 diffraction patterns.

Recently, a similar concept was described with an atmospheric pressure goniometer system at LCLS (Cohen *et al.*, 2014). Results from multiple molecules were presented along with a description of the instrumentation. The number of FEL shots used to obtained structural information was smaller, on average, than what has been published to date using liquid jets. Improvements in data analysis over the years and new developments in postrefinement (Uervirojnangkoorn *et al.*, 2015) techniques played a role in reducing the amount of data required. The small number of total crystals used makes the technique interesting for cases where few but relatively large crystals are available, especially when these crystals are known to suffer extensive damage during measurement at synchrotron sources. The goniometer system is now regularly used to study various samples (Dao *et al.*, 2015). The versatile

system can also be used for a variety of sample delivery techniques, including in-air jet systems and more recently developed microfluidic crystal trapping techniques (Lyubimov *et al.*, 2015).

c. Sample preparation and delivery

The samples required for effective use of femtosecond crystallography can be very different from what is typically used at synchrotrons. New techniques for preparing large quantities of small high-quality crystals have been developed. Most SFX publications describe in detail the specific sample preparation methods used. Some articles are dedicated solely to the description of the sample preparation methods used and describe all the challenges involved (Gallat *et al.*, 2014; Kupitz *et al.*, 2014b; Tran *et al.*, 2014; Ibrahim *et al.*, 2015; Wu *et al.*, 2015). Preparing lots of small crystals is not necessarily easier than spending the time to make a few single large crystals. Large crystals in LCP are very difficult to prepare and using ~5 μm crystals directly into the jet can save time and effort. However, in general SFX sample preparation has not proven to be easier than conventional methods and still represents a major challenge. Nevertheless, increasingly challenging samples are being studied with SFX, from viruses to molecular complexes (Demirci *et al.*, 2013; Bublitz *et al.*, 2015; Lawrence *et al.*, 2015).

Developments in Japan of a grease matrix method for delivering samples to an x-ray FEL beam represent one of the many ongoing efforts to make sample preparation and delivery simpler (Sugahara *et al.*, 2015). Efforts are primarily focused on viscous jets or extrusion systems that require minimal sample quantities, with exploration of various carrier media and their suitability for different proteins. Many of these techniques are now being adapted for use at synchrotrons, where slowly flowing jets are being used in the nascent technique of synchrotron serial crystallography (Gati *et al.*, 2014; Botha *et al.*, 2015; Nogly *et al.*, 2015).

d. Radiation damage

The SFX method is presumed to lead to damage-free diffraction patterns and structures, even though the intense x-ray pulses rapidly ionize the sample and turn it into a nanoplasma (Sec. IV.A). Under some conditions, this has been shown to be correct to within the accuracy of the measurements (Boutet *et al.*, 2012). However, under other conditions, such as intentionally longer pulses of soft x rays that have very high absorption cross sections, damage during the pulses was observed.

Early studies of damage focused on correlating the damage with loss of Bragg diffraction. One such study proposed the concept of Bragg termination, where the crystals diffract well until a moment when they simply do not anymore, due to random radiation-induced motion. This motion causes the loss of periodicity in the lattice and therefore the loss of Bragg diffraction (Barty *et al.*, 2012). Once Bragg termination occurs, the random distribution of atoms during the explosion produces only a diffuse background, which can be handled by data analysis software using a simple Debye-Waller B factor ($B = 8\pi^2\langle\mu^2\rangle$ with μ the displacement from the ideal lattice positions) correction to the intensities. The part of the pulse that comes prior to the onset of Bragg termination produces a measurable Bragg signal that gets proportionally weaker compared to the diffuse background for longer pulses. Figure 42 shows radiation damage effects consistent with simulations of Bragg termination.

Another study has found that, in addition to global damage, there was evidence of site-specific damage, which cannot be corrected via the use of a B factor (Lomb *et al.*, 2011). A continuation of this work has led to a more recent study at high resolution, reporting site-specific structural changes in metallic clusters in ferredoxin (Nass *et al.*, 2015). Ferredoxin contains two [4Fe-4S] clusters. A high-dose data set using a submicron LCLS focus of 7.36 keV x rays (above the iron K absorption edge) yielded clear difference electron density maps when compared to the synchrotron structure as seen in Fig. 43. The differences in radiation damage behavior between the two clusters suggest that small differences in metal coordination and environment could significantly affect the extent of radiation damage under high power density x-ray FEL illumination. The ultrafast charge rearrangement indicates that pulses of 20 fs or shorter duration are required to reduce radiation damage. The site-specific damage to ferredoxin was modeled by molecular dynamics and showed damage sufficiently reproducible, despite significant atomic motion during the pulse, to prevent Bragg diffraction from terminating (Hau-Riege and Bennion, 2015). These experimental results and simulations offer the first glimpse into LCLS-induced local damage to biomolecules without definitive answers. More studies are required to understand x-ray FEL radiation damage sufficiently to know the range of applicability of the diffraction-before-destruction techniques, especially at high resolution and with a tight x-ray focus approaching 100 nm. Such a tight focus will eventually be required to push the limits to the smallest possible crystals as well as to single-particle imaging (Sec. IV.E.5).

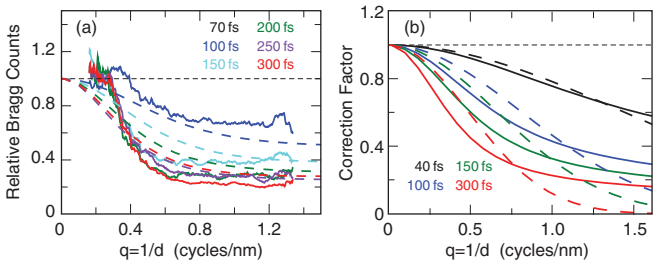

FIG. 42. Bragg termination under x-ray FEL illumination. (a) Integrated powder patterns showing the falloff of the measured Bragg intensity as a function of pulse duration for photosystem I crystals at a photon energy of 2 keV. The integrated intensity is shown relative to the shortest pulse duration (solid lines), along the simulated ratios from damage modeling (dashed lines). (b) Comparison of the simulated damage-driven disorder (solid lines) with the best fit Debye-Waller factor. Reasonable agreement between the two indicates that damage can be corrected to some extent through the use of a standard resolution-dependent correction factor to the intensities. Adapted from Barty *et al.*, 2012.

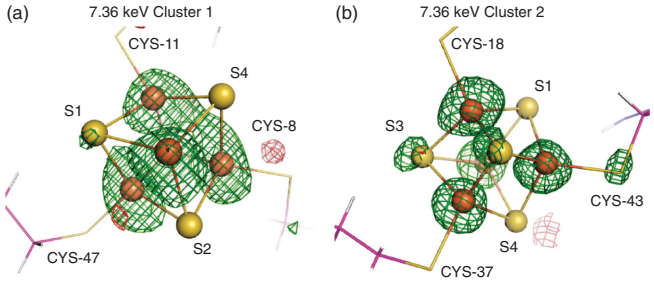

FIG. 43. Difference electron density between a synchrotron structure and an LCLS high-dose structure in ferredoxin. Clear differences in the electron density are visible from the green positive density and the red negative density contoured at the 3σ level. (a) Cluster 1 and (b) cluster 2 at 7.36 keV. *S*1, *S*2, *S*3, and *S*4 represent the sulfur atoms labeled 1 to 4 (*S*3 not shown). The cysteine (CYS) amino acids around the clusters are labeled with the residue number in the protein sequence. Adapted from Nass *et al.*, 2015.

e. Data processing

The multiple techniques of femtosecond crystallography at LCLS consist of collecting diffraction patterns on a fresh volume of crystalline material using individual pulses. Each pulse is unique and fluctuates in all manners: intensity, pointing, spectrum (Zhu *et al.*, 2012), focus size, and location (Sec. III.A). Additionally, the samples themselves often consist of small crystals that are not uniform in size and shape, leading to different scattering properties due to the coherent nature of the beam. Each of these crystals can be hit by the beam head-on or partially. Also, the FEL spectrum is typically narrower than the rocking width of crystals, leading to partial reflections. This leads to every Bragg peak measured representing a different random slice through the full three-dimensional Bragg peak in reciprocal space. All these fluctuations require SFX experiments to sum or average a large number of pulses to reduce the fluctuating quantities and yield meaningful structure factors.

Each Bragg peak must be measured multiple times before one can claim to know the value of its integrated intensity, unless the partiality of the Bragg reflection can somehow be determined accurately. This can in principle be achieved by controlling or measuring specific parameters more accurately. Controlling and measuring the spectrum of LCLS has, for example, been suggested as a way to improve data quality and use fewer pulses. This can be achieved using the self-seeded mode of LCLS operation (Sec. II.B.2). However, a recent study showed an example where little to no advantage in data quality was observed from using a self-seeded beam in SFX (Barends *et al.*, 2015a), which indicates other sources of errors are dominant and there is a need for further studies.

So-called Monte Carlo methods have been developed to deal with the unique properties of FEL crystallography data (Kirian *et al.*, 2011; White *et al.*, 2013; Hattne *et al.*, 2014). Multiple software packages are now available for download and use (Foucar *et al.*, 2012; White *et al.*, 2012; Sauter *et al.*, 2013; Barty *et al.*, 2014; Zeldin *et al.*, 2015). There is a growing consensus within the community that software is one of the primary limitations to the SFX data quality and more sophisticated methods have been developed, including postrefinement methods, with the hope of significant sample and beam time consumption reductions. A few recent publications made use of postrefinement techniques to obtain structures with fewer LCLS pulses or to improve the quality of the results (Ginn *et al.*, 2015a, 2015b; Uervirojnangkoorn *et al.*, 2015).

f. The phase problem

The phase problem is well known in x-ray crystallography. Only the amplitude of the scattered waves is measured and the phases are lost in the measurement. In order to retrieve a structure, the phase information must be acquired. The most commonly used phasing method for macromolecular crystallography is molecular replacement, where a known, similar structure is used to get a good initial guess at the phases, which is subsequently refined. To date, all LCLS published structures were obtained using this method except for one. The technique of single-wavelength anomalous dispersion (SAD) was used to demonstrate the feasibility of *de novo* phasing at LCLS (Barends *et al.*, 2014). A test sample of lysozyme was soaked in gadolinium-containing solution, leading to site-specific binding of Gd atoms. Using the anomalous scattering of Gd at an energy above its L_3 absorption edge, the phases of the diffraction pattern could be retrieved from the data alone.

While this result shows the feasibility of phasing using an x-ray FEL beam, the demonstration does not make the approach routine. Over 60 000 indexed diffraction patterns were required to perform the initial phasing of these data. This very large data volume prohibits practical application of the technique for any valuable, rare and, therefore, likely interesting sample. While the success of phasing is a great step towards making SFX useful for novel structure determination, developments are required to make it a routine technique suitable for a broad range of samples.

Other alternative phasing approaches are being explored. Radiation-induced modification to anomalous scattering signals could make use of the inevitable radiation-induced changes in the sample to produce anomalous differences to be used for phasing (Son, Chapman, and Santra, 2013; Galli *et al.*, 2015). Oversampling methods can make use of the intensity between the Bragg peaks in iterative phase-retrieval algorithms (Chapman *et al.*, 2011; Yefanov *et al.*, 2014). Anomalous dispersion could be used with two wavelengths simultaneously using two colors in a single pulse, allowing anomalous differences to be measured from the same crystal and the same pulse (Marinelli *et al.*, 2015). This could provide a faster and more reliable method for scaling intensities in the two wavelengths used in multiwavelength anomalous dispersion (MAD). All these proposed techniques are under development, awaiting experimental demonstration.

5. Single-particle techniques

The use of crystallographic techniques at LCLS has been a great success but still requires the growth of crystals, which can range from difficult to impossible and can also lock molecular conformations into a limited set of states, not necessarily representative of the native structure. The ultimate tool for studying biological molecules would be a technique

capable of producing a high-resolution image of any sample, especially without a need for crystallization and at biologically relevant temperatures.

a. Single-particle imaging

X-ray FELs such as LCLS can in principle provide a path to single-particle imaging (SPI) by collecting 2D coherent diffractive imaging patterns from individual noncrystalline particles and assembling a three-dimensional pattern from multiple copies of sufficiently identical particles. The promise of single-particle imaging is tantalizing, with all the challenges related to crystal growth and crystallography in general removed. Studying single molecules free of the crystal contacts and interactions that may distort their structure at room temperature would be revolutionary. The extremely weak signal, especially at high resolution, expected from single biological molecules makes imaging them in this way very challenging.

A wide range of preliminary developments toward imaging techniques for FELs began using the FLASH facility as early as 2006 (Sec. III.B.1). As LCLS turned on in 2009, existing developments allowed the technique to be tried immediately. Mimiviruses, the largest viruses known at the time, were delivered to the LCLS 1.8 keV beam in vacuum. Single diffraction patterns were obtained and successfully phased using iterative methods to reconstruct the electron density of a few individual snapshots (Seibert *et al.*, 2011). The resolution of ~32 nm was limited by the interpretable signal level, not by the x-ray wavelength.

The task of moving from demonstration to routine application is daunting: Expected signal levels were, and will remain, weak; hit rates were low when using the tightly focused x-ray beam needed to generate a measurable signal from small particles; algorithms were required to handle the data and merge it into three dimensions. The next few years saw significant efforts toward improving sample delivery methods and developing algorithms. Reconstruction methods were improved for 2D patterns from test objects and some biological molecules (Martin *et al.*, 2011, 2012a, 2012b). Classification methods required to sort the diffraction patterns into groups with identical orientation were developed, showing that the process could proceed in an unsupervised way (Yoon *et al.*, 2011; Park *et al.*, 2013) and leading to three-dimensional reconstructions from multiple copies of the same object (Kassemeyer *et al.*, 2013). Correlations between diffraction patterns can also provide a method for obtaining three-dimensional structures. This was demonstrated using test objects, in this case two polystyrene spheres stuck together (Starodub *et al.*, 2012).

Algorithm development is critical to realizing the single-particle imaging technique, but its success relies on high-quality test data. Real data are ultimately required, since the real properties of background noise cannot at this time be well simulated. This noise often overwhelms the signal, at least at low resolutions (angles close to the direct beam where undesirable beam line noise is the strongest), and its fluctuating nature makes building appropriate noise models for the algorithms difficult. A data repository for entire LCLS data sets was created for the specific purpose of sharing real data for the development of software (Maia, 2012). Entire data sets can be deposited for use by the scientific community (Kassemeyer *et al.*, 2012).

More recently, reconstructed images from significantly smaller objects, carboxysomes, were obtained at a resolution slightly better than 20 nm (Hantke *et al.*, 2014). New processing techniques allowing the sorting of diffraction patterns, based on the size of the object deduced from the diffraction, allowed identification of good single-particle hits for further processing while rejecting bad hits.

Even more recently, coherent diffractive imaging of single cyanobacteria living cells was published (van der Schot *et al.*, 2015). The reconstructed images were limited to ~70 nm resolution, but evidence for speckles extending up to 4 nm was presented. Cell imaging at LCLS, where every cell can see only one pulse, is limited to 2D images due to the nonreproducibility of the cells.

Work continues on improving techniques and data analysis for single-particle imaging. Three-dimensional reconstructions previously achieved on test samples (Kassemeyer *et al.*, 2013) were recently achieved on biological samples. A three-dimensional reconstruction of a mimivirus was obtained from 198 individual diffraction patterns (Ekeberg *et al.*, 2015). The assembled three-dimensional diffraction pattern from these 198 2D snapshots of individual mimiviruses is shown in Fig. 44.

As a side effect of the development of tools for imaging biomolecules, other fields of science benefited from using the same techniques. For example, studies were published on soot aerosols without needing to capture them on a surface, which would likely change their structure and morphology (Loh *et al.*, 2012; Pedersoli *et al.*, 2013). The use of imaging techniques has also led to interesting results in AMO science (Sec. IV.A.4), in magnetic imaging (Sec. IV.B.3), and in lattice dynamics studies (Sec. IV.B.4).

A broad literature discusses the expected signal and noise levels as well as the impacts of radiation damage, with only one clear conclusion at this time—that shorter pulses are better for a given number of photons per pulse. There is a clear advantage for having pulses shorter than the Auger lifetimes of the relevant atoms in the sample (Hau-Riege *et al.*, 2007; Fung *et al.*, 2009; Loh and Elser, 2009; Maia *et al.*, 2009; Son, Young, and Santra, 2011; Hau-Riege, 2012). Continued effort

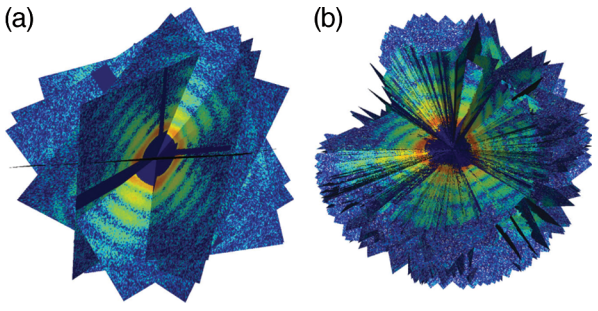

FIG. 44. Assembled three-dimensional mimivirus diffraction pattern from 198 2D diffraction patterns. (a) Subset of ten diffraction patterns shown in their best orientation. (b) All 198 diffraction patterns shown with a cutout showing the origin in reciprocal space. Adapted from Ekeberg *et al.*, 2015.

will be required to systematically resolve the technical challenges involved in single-particle imaging. To this effect, an LCLS-led effort is underway to further push the limits and the understanding of the technique (Aquila *et al.*, 2015).

6. Perspectives

Femtosecond crystallography represents a significant success of LCLS in the area of biology. This method has led to structural insight that could not be obtained without the high-energy short pulses from x-ray FELs. The potential benefits of short x-ray pulses used with the diffraction-before-destruction method for the study of biological samples was one of the driving forces leading to the construction of x-ray FELs, and the field has grown rapidly since the start of LCLS operations.

However, it is not expected to replace conventional crystallography. It will likely remain of limited application for as long as x-ray FEL beam time remains rare, as it is today. X-ray FEL-based crystallography will be useful for challenging problems that elude solution at conventional sources. As an example, while the number of GPCR studies aimed at providing a basis for structure-based drug design is still relatively small, this is an area of expected significant growth and impact, with LCLS providing a unique tool to study these difficult systems. But even before this can become a reality for the majority of those challenging problems, significant improvements are still required in understanding radiation damage, processing data, reducing sample consumption, and making sample preparation easier. Continued improvement in sample delivery in terms of reliability and flexibility of use for all types of samples is still needed. Multiple review articles regarding SFX are available (Fromme and Spence, 2011; Schlichting and Miao, 2012; Spence, Weierstall, and Chapman, 2012; Bogan, 2013; Feld and Frank, 2014; Neutze, Brändén, and Schertler, 2015; Schlichting, 2015).

The damage-free study of dynamics in systems at ambient conditions will likely be the key area of impact in the life sciences for LCLS and x-ray FELs. Time-resolved SFX and SAXS and WAXS are both expected to play an increasing role due to the natural fit of time-resolved studies with the machine capabilities. Typically, interesting L edges for biology will lie at photon energies well below those suitable for high-resolution crystallography, making this a challenge for simultaneous measurements. Two-color x-ray beams with a soft and a hard x-ray component could allow such studies in the future. LCLS-II, with its higher repetition rate, and other x-ray FELs will likely have a significant impact on time-resolved spectroscopic techniques (Sec. V). Time-resolved dynamics measurements will likely broaden to more than the use of a pump laser to initiate dynamics. Small crystals used with LCLS and liquid jets will allow rapid diffusion of reagents inside crystals, and fast-mixing jet systems under development will be an important enabling technology toward these types of studies (Wang *et al.*, 2014). Beyond this, other types of stimuli, such as THz radiation, could allow the study of dynamics in more systems. THz radiation is already used for materials studies, AMO science, and timing diagnostics (Hoffmann and Turner, 2012). Furthermore, recent development in modeling of diffraction data can be used to extract multiple conformations. Combined with computational techniques, mapping the conformational landscape of a molecule in this way can provide important insight on its dynamics. Recent work combined synchrotron and LCLS data to study the structural basis of functional conformational dynamics in an enzyme by using temperature to understand correlated motions (Keedy *et al.*, 2015).

To date, single-particle imaging results in biology from LCLS can be classified as technique development efforts. No new biological information has been acquired, primarily due to the low signal level limiting the resolution, along with noise levels making single-photon identification difficult. Technical challenges in improving beam quality and reducing noise, as well as improving sample delivery and data analysis, along with understanding the radiation damage limits are the subject of the single-particle imaging road map which outlines a path to make the technique a reality (Aquila *et al.*, 2015). Many factors are involved in limiting the resolution achieved to date. Both soft and hard x rays have been used to pursue single-particle imaging, with no clear consensus at this point regarding the ideal photon energy to use for this endeavor, but with some indication it may lie at the boundary between soft and hard x rays.

The combination of damage-free probing, small samples, dynamics capabilities, and room-temperature studies is what makes x-ray FELs such unique and interesting tools for life sciences. A constant push toward smaller samples will hopefully allow the full realization of the potential of the sources.

V. FUTURE OUTLOOK

A. Accomplishments to date

The first five years of LCLS have brought significant new insight in a number of scientific fields. After the x-ray lasing process was brought into routine operation, additional FEL modes beyond the original design were developed. Using the FEL itself as a seed for the SASE process led to improved spectral control, and multiple pulses can now be generated at controllable energy and temporal delay. These advanced modes have expanded the science reach of x-ray FELs. FEL radiation applications that use the high x-ray pulse energy to generate extreme states of matter have produced important scientific results in atomic, plasma, and solid-state physics. Full exploitation of the transverse FEL coherence to measure ultrafast nanoscale dynamics or image single biological particles or molecules has developed to a lesser degree than expected due to technical challenges. However, in the field of macromolecular crystallography of radiation-sensitive biomolecules, FELs are becoming a standard method to resolve important and otherwise inaccessible structure-function relationships. New experimental insight into ultrafast processes that underlie important functions in the fields of materials, chemical, and biological sciences has emerged since the turn-on of LCLS. Constant technical developments and improvements in x-ray detectors, single FEL pulse characterization methods, and timing diagnostics with respect to ultrafast optical light sources have tremendously contributed to this progress.

B. Global x-ray FEL source evolution

The field of x-ray laser science, performed at photon energies greater than 270 eV, is rapidly expanding with more than a half dozen x-ray FELs either in operation or under construction across the globe. The characteristic parameters of these facilities are summarized in Table II. There are many more x-ray FEL facilities in various planning stages, but those will not be discussed here.

In addition to SACLA (Ishikawa *et al.*, 2012; Yabashi, Tanaka, and Ishikawa, 2015) and the European XFEL (Altarelli *et al.*, 2006) mentioned in the Introduction (Sec. I.A), the PAL-XFEL (Kang, Kim, and Ko, 2013) and SwissFEL (Ganter *et al.*, 2010) are near the end of construction, with anticipated first light in 2016 and 2017, respectively. Together with LCLS, these five large x-ray FELs employ multi-GeV energy electron beams and can produce x-ray photons up to 25 keV at the fundamental frequency. At the lower spectral end, both FLASH (Ackermann *et al.*, 2007) and FERMI (Allaria *et al.*, 2012, 2013, 2015) use 1 GeV electron beams to reach from "water window" soft x rays down to the ultraviolet spectral range, with photon energies 10–30 eV. Facilities driven by normal-conducting linear accelerators operate at 10–100 Hz repetition rates, while facilities driven by superconducting linear accelerators (FLASH, European XFEL, and LCLS-II) operate at much higher repetition rates and offer higher average brightness in addition to high peak brightness. In particular, the central part of the LCLS-II facility (Galayda *et al.*, 2014) will be driven by a 4 GeV superconducting linear accelerator in continuous-wave mode with a repetition rate up to 1 MHz, leading to several orders of improvement in average brightness in the photon energy range from 0.2 to 5 keV.

With the exception of the FERMI FEL, all x-ray FEL sources have started or will start operation in the SASE mode. Nevertheless, to overcome the chaotic characteristics of the SASE source in the temporal and spectral domains, most of these facilities are developing seeding methods and seeded x-ray sources. For technical reasons briefly mentioned in Sec. II.B.2, hard x-ray FELs typically employ self-seeding while soft x-ray FELs use a variety of seeding techniques, including self-seeding and external laser seeding. Reaching Fourier transform limited pulses remains one of the ultimate goals for source development. Such pulses enable effective undulator tapering to extract power well beyond saturation and potentially reach terawatt levels. In addition to seeding and power enhancement, various x-ray pulse waveform controls are being pursued in concept and in experiments. These include polarization control, attosecond x-ray pulses, multiple pulses, and two-color pulses. These developments are analogous to that of optical lasers, with the ultimate goal of generating programmable pulse sequences that can be tailored to specific scientific applications (Hemsing *et al.*, 2014; Pellegrini, Marinelli, and Reiche, 2016).

C. Science outlook

The pulse control realized by optical lasers enabled the fields of nonlinear optics, precision spectroscopy, and holography. The expected advances in x-ray FELs described in Sec. V.B will enable new methods (e.g., multidimensional x-ray spectroscopy) and transition other methods from demonstration experiments (e.g., time-resolved resonant inelastic x-ray scattering) to high-output scientific measurement tools.

The extended scientific reach of x-ray FELs will remain broad into the future (Schoenlein *et al.*, 2015). In atomic and molecular physics, coincidence techniques will capture rare events and yield complete insight into charge-transfer processes with femtosecond resolution. In chemistry, advanced x-ray spectroscopic techniques promise to improve our understanding of the electronic mechanisms of photocatalysis, potentially improving solar energy conversion. Two-color x-ray pulses will capture charge dynamics and conformational changes in photoexcited catalytic systems. In strongly

TABLE II. The characteristic parameters of the various x-ray FEL user facilities summarized across the globe. These include the location, name of the facility, linac type (NC: normal conducting, SC: superconducting), maximum electron energy (E energy), photon beam energy range, repetition rate (Rep. rate), and year of start or expected start of operation (Start ops.).

Location	Name	Linac type	E energy (GeV)	Photon energy (keV)	Rep. rate (Hz)	Start ops.
Germany	FLASH	SC	1.2	0.03–0.3	$(1-500)\times 10$[a]	2005
	FLASH-II	SC				2015
	XFEL	SC	17.5	3–25	$(1-2800)\times 10$[b]	2017
				0.2–3		
Italy	FERMI-FEL1	NC	1.5	0.01–0.06	10–50	2012
	FERMI-FEL2			0.06–0.3		2014
Japan	SACLA	NC	8	4–15	30–60	2011
Korea	PAL-XFEL	NC	10	1–20	60	2016
			3	0.3–1		
Switzerland	SwissFEL	NC	5.8	2–12	100	2017
			3	0.2–2		
USA	LCLS	NC	16	0.25–11	120	2009
	LCLS-II	NC	16	1–25	120	2020
	LCLS-II	SC	4	0.2–5	10^6	2020

[a]Pulsed mode operation at 10 Hz, with each macropulse providing up to 500 bunches.
[b]Pulsed mode operation at 10 Hz, with each macropulse providing up to 2800 bunches.

correlated systems, emergent phenomena arising from correlated interactions between lattice, spins, and charges will be explored with time-resolved high-resolution x-ray spectroscopic methods. These methods are enabled by the increased flux of high-repetition-rate x-ray FELs. High-energy FELs (>15 keV) will penetrate deeper into matter in extreme conditions, providing access to transient shock phenomena on atomic length scales. The biological function of interacting complexes will be revealed in real time and in native environments through solution scattering. High-repetition-rate hard x-ray sources will boost the throughput of serial nanocrystallography. As the technical challenges of single-particle imaging are resolved, including the delivery of high-intensity ultrashort x-ray pulses, the ability to routinely characterize the structure of biological molecules without the need for crystallization may be realized.

When considering this outlook, it is worthwhile to recount that the first five years of LCLS operation generated many unanticipated methods and discoveries. With many new next-generation x-ray FEL sources coming online in the next five years, the advancement of science will only continue to accelerate.

ACKNOWLEDGMENTS

We are especially grateful for the guidance and support of Persis S. Drell in the realization of this manuscript. We express our sincere thanks to the many people at SLAC, Argonne, Lawrence Berkeley, and Lawrence Livermore National Laboratories, Cornell University, and the University of California, Los Angeles, who helped build LCLS, and to the accelerator physicists and the user community across the globe who contributed to making LCLS such a success. We also thank John Arthur, Uwe Bergmann, Mike Dunne, Paul Emma, Michael Först, Kelly Gaffney, Jerry Hastings, Jerry LaRue, Richard Lee, Ingolf Lindau, Andy MacKinnon, Claudio Pellegrini, Ilme Schlichting, Jochen Schneider, Robert W. Schoenlein, Joachim Stöhr, Soichi Wakatsuki, and Linda Young for their valuable feedback at various stages of the manuscript. We thank David Goldgof for his substantial effort assembling the reference list. We thank Terry Anderson and Gregory Stewart for helping with the figures. The SXR instrument at LCLS was funded by a consortium whose membership includes LCLS, Stanford University through the Stanford Institute for Materials and Energy Sciences (SIMES), Lawrence Berkeley National Laboratory (LBNL), the University of Hamburg through the BMBF priority program No. FSP 301, and the Center for Free Electron Laser (CFEL). We acknowledge the Max Planck Society for funding the development and operation of the CAMP instrument within the ASG at CFEL. The LAMP end station at AMO was partially funded by Norah Berrah through a U.S. Department of Energy, Office of Science, Office of Basic Energy Sciences, SISGR Grant No. DE-SC0002004. The MEC instrument has additional support from the DOE Office of Science, Office of Fusion Energy Sciences under Contract No. SF00515. C. B. and G. J. W. acknowledge support from the U.S. Department of Energy, Office of Science, Office of Basic Energy Sciences, under Contracts No. DE-AC02-06CH11357 and No. DE-SC0012704, respectively. Use of the Linac Coherent Light Source (LCLS), SLAC National Accelerator Laboratory, is supported by the U.S. Department of Energy, Office of Science, Office of Basic Energy Sciences under Contract No. DE-AC02-76SF00515.

REFERENCES

Ackermann, W., *et al.*, 2007, Nat. Photonics **1**, 336.
Akre, R., *et al.*, 2008, Phys. Rev. ST Accel. Beams **11**, 030703.
Albert, F., R. Shah, K. Ta Phuoc, R. Fitour, F. Burgy, J. P. Rousseau, A. Tafzi, D. Douillet, T. Lefrou, and A. Rousse, 2008, Phys. Rev. E **77**, 056402.
Allaria, E., *et al.*, 2012, Nat. Photonics **6**, 699.
Allaria, E., *et al.*, 2013, Nat. Photonics **7**, 913.
Allaria, E., *et al.*, 2015, J. Synchrotron Radiat. **22**, 485.
Alonso-Mori, R., *et al.*, 2012a, Proc. Natl. Acad. Sci. U.S.A. **109**, 19103.
Alonso-Mori, R., *et al.*, 2012b, Rev. Sci. Instrum. **83**, 073114.
Alonso-Mori, R., *et al.*, 2015, J. Synchrotron Radiat. **22**, 508.
Altarelli, M., *et al.*, 2006, Technical Design Report of the European XFEL.
Amann, J., *et al.*, 2012, Nat. Photonics **6**, 693.
Ament, L. J. P., M. van Veenendaal, T. P. Devereaux, J. P. Hill, and J. van den Brink, 2011, Rev. Mod. Phys. **83**, 705.
Aquila, A., *et al.*, 2012, Opt. Express **20**, 2706.
Aquila, A., *et al.*, 2015, Struct. Dyn. **2**, 041701.
Arnlund, D., *et al.*, 2014, Nat. Methods **11**, 923.
Arthur, J., *et al.*, 2002, Linac Coherent Light Source (LCLS) Conceptual Design Report, Report No. SLAC-R-593.
Ayvazyan, V., *et al.*, 2002, Phys. Rev. Lett. **88**, 104802.
Bajt, S., *et al.*, 2008, Appl. Opt. **47**, 1673.
Bane, K., *et al.*, 2009, Phys. Rev. ST Accel. Beams **12**, 030704.
Barbara, P. F., T. J. Meyer, and M. A. Ratner, 1996, J. Phys. Chem. **100**, 13 148.
Barends, T., *et al.*, 2015a, J. Synchrotron Radiat. **22**, 644.
Barends, T. R., *et al.*, 2014, Nature (London) **505**, 244.
Barends, T. R. M., *et al.*, 2015b, Science **350**, 445.
Barty, A., R. A. Kirian, F. R. Maia, M. Hantke, C. H. Yoon, T. A. White, and H. Chapman, 2014, J. Appl. Crystallogr. **47**, 1118.
Barty, A., *et al.*, 2008, Nat. Photonics **2**, 415.
Barty, A., *et al.*, 2012, Nat. Photonics **6**, 35.
Batchelor, K., *et al.*, 1992, Nucl. Instrum. Methods Phys. Res., Sect. A **318**, 372.
Beaud, P., *et al.*, 2014, Nat. Mater. **13**, 923.
Becker, U., 2000, J. Electron Spectrosc. Relat. Phenom. **112**, 47.
Behrens, C., *et al.*, 2014, Nat. Commun. **5**, 3762.
Bergeard, N., *et al.*, 2015, Phys. Rev. B **91**, 054416.
Bernitt, S., *et al.*, 2012, Nature (London) **492**, 225.
Berrah, N., *et al.*, 2011, Proc. Natl. Acad. Sci. U.S.A. **108**, 16912.
Beye, M., *et al.*, 2012, Appl. Phys. Lett. **100**, 121108.
Beye, M., *et al.*, 2013a, Phys. Rev. Lett. **110**, 186101.
Beye, M., S. Schreck, F. Sorgenfrei, C. Trabant, N. Pontius, C. Schuessler-Langeheine, W. Wurth, and A. Foehlisch, 2013b, Nature (London) **501**, 191.
Bionta, M. R., *et al.*, 2014, Rev. Sci. Instrum. **85**, 083116.
Birgeneau, R. J., and Z.-X. Shen, 1997, Report of the basic energy sciences advisory committee panel on D.O.E synchotron radiation sources and science, Technical Report (U.S. Department of Energy).
Blaj, G., *et al.*, 2015, J. Synchrotron Radiat. **22**, 577.
Bogan, M., *et al.*, 2008, Nano Lett. **8**, 310.
Bogan, M. J., 2013, Anal. Chem. **85**, 3464.
Bohm, D., and E. P. Gross, 1949, Phys. Rev. **75**, 1851.
Boll, R., *et al.*, 2013, Phys. Rev. A **88**, 061402.

Bonifacio, R., C. Pellegrini, and L. Narducci, 1984, Opt. Commun. **50**, 373.
Borghesi, M., D. H. Campbell, A. Schiavi, M. G. Haines, O. Willi, A. J. MacKinnon, P. Patel, L. A. Gizzi, M. Galimberti, and R. J. Clarke, 2002, Phys. Plasmas **9**, 2214.
Borland, M., *et al.*, 2002, Nucl. Instrum. Methods Phys. Res., Sect. A **483**, 268.
Bostedt, C., M. Adolph, E. Eremina, M. Hoener, D. Rupp, S. Schorb, H. Thomas, A. R. B. de Castro, and T. Möller, 2010, J. Phys. B **43**, 194011.
Bostedt, C., *et al.*, 2008, Phys. Rev. Lett. **100**, 133401.
Bostedt, C., *et al.*, 2009, Nucl. Instrum. Methods Phys. Res., Sect. A **601**, 108.
Bostedt, C., *et al.*, 2012, Phys. Rev. Lett. **108**, 093401.
Bostedt, C., *et al.*, 2013, J. Phys. B **46**, 164003.
Botha, S., *et al.*, 2015, Acta Crystallogr. Sect. D **71**, 387.
Boutet, S., M. Bogan, A. Barty, M. Frank, W. Benner, S. Marchesini, M. Seibert, J. Hajdu, and H. Chapman, 2008, J. Electron Spectrosc. Relat. Phenom. **166–167**, 65.
Boutet, S., and G. J. Williams, 2010, New J. Phys. **12**, 035024.
Boutet, S., *et al.*, 2012, Science **337**, 362.
Boutet, S., *et al.*, 2015, J. Synchrotron Radiat. **22**, 634.
Bozek, J. D., 2009, Eur. Phys. J. Spec. Top. **169**, 129.
Bressler, C., *et al.*, 2009, Science **323**, 489.
Brown, C. R., *et al.*, 2014, Sci. Rep. **4**, 5214.
Bublitz, M., *et al.*, 2015, IUCrJ **2**, 409.
Canton, S. E., *et al.*, 2014, J. Phys. Chem. C **118**, 4536.
Carini, G. A., *et al.*, 2014, J. Phys. Conf. Ser. **493**, 012011.
Carlsten, B., 1989, Nucl. Instrum. Methods Phys. Res., Sect. A **285**, 313.
Carnis, J., *et al.*, 2014, Sci. Rep. **4**, 6017.
Carpenter, E., K. Beis, A. Cameron, and S. Iwata, 2008, Curr. Opin. Struct. Biol. **18**, 581.
Catalan, G., R. M. Bowman, and J. M. Gregg, 2000, Phys. Rev. B **62**, 7892.
Caviglia, A., *et al.*, 2013, Phys. Rev. B **88**, 220401.
Cederbaum, L. S., F. Tarantelli, A. Sgamellotti, and J. Schirmer, 1986, J. Chem. Phys. **85**, 6513.
Chalupský, J., *et al.*, 2011, Nucl. Instrum. Methods Phys. Res., Sect. A **631**, 130.
Chalupský, J., *et al.*, 2015, Phys. Rev. Applied **4**, 014004.
Chang, J., *et al.*, 2012, Nat. Phys. **8**, 871.
Chapman, H. N., C. Caleman, and N. Timneanu, 2014, Phil. Trans. R. Soc. B **369**, 20130313.
Chapman, H. N., *et al.*, 2006, Nat. Phys. **2**, 839.
Chapman, H. N., *et al.*, 2007, Nature (London) **448**, 676.
Chapman, H. N., *et al.*, 2011, Nature (London) **470**, 73.
Chen, P., and T. J. Meyer, 1998, Chem. Rev. **98**, 1439.
Chergui, M., 2013, in *Spin-Crossover Materials: Properties and Applications*, edited by M. A. Halcrow (Wiley, New York), Chap. 15, pp. 405–424.
Cho, B. I., *et al.*, 2012, Phys. Rev. Lett. **109**, 245003.
Chollet, M., *et al.*, 2015, J. Synchrotron Radiat. **22**, 503.
Chuang, Y. D., *et al.*, 2013, Phys. Rev. Lett. **110**, 127404.
Chung, H.-K., and R. W. Lee, 2009, High Energy Density Phys. **5**, 1.
Ciricosta, O., *et al.*, 2012, Phys. Rev. Lett. **109**, 065002.
Clark, J. N., *et al.*, 2013, Science **341**, 56.
Cocco, D., *et al.*, 2013, Proc. SPIE Int. Soc. Opt. Eng. **8849**, 88490A.
Cohen, A. E., *et al.*, 2014, Proc. Natl. Acad. Sci. U.S.A. **111**, 17122.
Conrad, C. E., *et al.*, 2015, IUCrJ **2**, 421.
Cowley, S., *et al.*, 2010, *Plasma Science; Advancing Knowledge in the National Interest* (The National Academies Press, Washington, DC).
Crowley, B. J. B., 2014, High Energy Density Phys. **13**, 84.
Cryan, J. P., *et al.*, 2010, Phys. Rev. Lett. **105**, 083004.
Cryan, J. P., *et al.*, 2012, J. Phys. B **45**, 055601.
Dagotto, E., 2003, *Nanoscale Phase Separation and Colossal Magnetoresistance: The Physics of Manganites and Related Compounds* (Springer, Berlin).
Dakovski, G. L., P. Heimann, M. Holmes, O. Krupin, M. P. Minitti, A. Mitra, S. Moeller, M. Rowen, W. F. Schlotter, and J. J. Turner, 2015, J. Synchrotron Radiat. **22**, 498.
Dakovski, G. L., W.-S. Lee, D. G. Hawthorn, N. Garner, D. Bonn, W. Hardy, R. Liang, M. C. Hoffmann, and J. J. Turner, 2015, Phys. Rev. B **91**, 220506.
Dao, E. H., *et al.*, 2015, Struct. Dyn. **2**, 041706.
Daranciang, D., *et al.*, 2012, Phys. Rev. Lett. **108**, 087601.
Deacon, D., L. Elias, J. Madey, G. Ramian, H. Schwettman, and T. Smith, 1977, Phys. Rev. Lett. **38**, 892.
de Jong, S., *et al.*, 2013, Nat. Mater. **12**, 882.
Dell'Angela, M., *et al.*, 2013, Science **339**, 1302.
Demirci, H., *et al.*, 2013, Acta Crystallogr. Sect. F **69**, 1066.
DePonte, D. P., U. Weierstall, K. Schmidt, J. Warner, D. Starodub, J. C. H. Spence, and R. B. Doak, 2008, J. Phys. D **41**, 195505.
Diamant, R., S. Huotari, K. Hämäläinen, C. C. Kao, and M. Deutsch, 2000, Phys. Rev. Lett. **84**, 3278.
DiMitri, S., and M. Cornacchia, 2014, Phys. Rep. **539**, 1.
Ding, Y., C. Behrens, P. Emma, J. Frisch, Z. Huang, H. Loos, P. Krejcik, and M. Wang, 2011, Phys. Rev. ST Accel. Beams **14**, 120701.
Ding, Y., *et al.*, 2009, Phys. Rev. Lett. **102**, 254801.
Doering, D., *et al.*, 2011, Rev. Sci. Instrum. **82**, 073303.
Dolgashev, V. A., and J. Wang, 2012, in *15th Advanced Accelerator Concepts Workshop*, edited by R. Zgadzaj, E. Gaul, and M. C. Downer, AIP Conf. Proc. No. 1507 (AIP, New York), pp. 682–687.
Dörner, R., V. Mergel, O. Jagutzki, L. Spielberger, J. Ullrich, R. Moshammer, and H. Schmidt-Böcking, 2000, Phys. Rep. **330**, 95.
Doumy, G., *et al.*, 2011, Phys. Rev. Lett. **106**, 083002.
Duguay, M. A., and P. M. Rentzepis, 1967, Appl. Phys. Lett. **10**, 350.
Düsterer, S., *et al.*, 2011, New J. Phys. **13**, 093024.
Duszenko, M., L. Redecke, C. N. Mudogo, B. P. Sommer, S. Mogk, D. Oberthuer, and C. Betzel, 2015, Acta Crystallogr. Sect. F **71**, 929.
Ecker, G., and W. Kröll, 1963, Phys. Fluids **6**, 62.
Eckert, S., *et al.*, 2015, Appl. Phys. Lett. **106**, 061104.
Eisebitt, S., J. Luning, W. F. Schlotter, M. Lorgen, O. Hellwig, W. Eberhardt, and J. Stohr, 2004, Nature (London) **432**, 885.
Eisenberger, P. M., and S. L. McCall, 1971, Phys. Rev. A **3**, 1145.
Ekeberg, T., *et al.*, 2015, Phys. Rev. Lett. **114**, 098102.
Eland, J. H. D., M. Tashiro, P. Linusson, M. Ehara, K. Ueda, and R. Feifel, 2010, Phys. Rev. Lett. **105**, 213005.
Emma, P., K. Bane, M. Cornacchia, Z. Huang, H. Schlarb, G. Stupakov, and D. Walz, 2004, Phys. Rev. Lett. **92**, 074801.
Emma, P., R. Carr, and H.-D. Nuhn, 1999, Nucl. Instrum. Methods Phys. Res., Sect. A **429**, 407.
Emma, P., *et al.*, 2010, Nat. Photonics **4**, 641.
Erk, B., *et al.*, 2013, Phys. Rev. Lett. **110**, 053003.
Erk, B., *et al.*, 2014, Science **345**, 288.
Fang, L., *et al.*, 2010, Phys. Rev. Lett. **105**, 083005.
Faure, J., Y. Glinec, A. Pukhov, S. Kiselev, S. Gordienko, E. Lefebvre, J. P. Rousseau, F. Burgy, and V. Malka, 2004, Nature (London) **431**, 541.
Fausti, D., R. I. Tobey, N. Dean, S. Kaiser, A. Dienst, M. C. Hoffmann, S. Pyon, T. Takayama, H. Takagi, and A. Cavalleri, 2011, Science **331**, 189.
Feld, G. K., and M. Frank, 2014, Curr. Opin. Struct. Biol. **27**, 69.

Feld, G. K., *et al.*, 2015, J. Appl. Crystallogr. **48**, 1072.
Feldhaus, J., E. Saldin, J. Schneider, E. Schneidmiller, and M. Yurkov, 1997, Opt. Commun. **140**, 341.
Fenalti, G., *et al.*, 2015, Nat. Struct. Mol. Biol. **22**, 265.
Feng, Y., J. Amann, D. Cocco, C. Field, J. Hastings, P. Heimann, Z. Huang, H. Loos, J. Welch, and J. Wu, 2012, in *34th International Free-Electron Laser Conference*, edited by T. Tanaka, and V. R. Schaa (Joint Accelerator Conferences Website), pp. 205–212.
Feng, Y., *et al.*, 2011, Proc. SPIE Int. Soc. Opt. Eng. **8140**, 81400Q.
Feng, Y., *et al.*, 2015, J. Synchrotron Radiat. **22**, 626.
Fennel, T., K.-H. Meiwes-Broer, J. Tiggesbaumker, P.-G. Reinhard, P. M. Dinh, and E. Suraud, 2010, Rev. Mod. Phys. **82**, 1793.
Ferguson, K. R., *et al.*, 2015, J. Synchrotron Radiat. **22**, 492.
Fiuza, F., R. A. Fonseca, J. Tonge, W. B. Mori, and L. O. Silva, 2012, Phys. Rev. Lett. **108**, 235004.
Fleming, G. R., J. L. Martin, and J. Breton, 1988, Nature (London) **333**, 190.
Fletcher, L. B., E. Galtier, P. Heimann, H. J. Lee, B. Nagler, J. Welch, U. Zastrau, J. B. Hastings, and S. H. Glenzer, 2013, J. Instrum. **8**, C11014.
Fletcher, L. B., *et al.*, 2015, Nat. Photonics **9**, 274.
Först, M., *et al.*, 2011, Phys. Rev. B **84**, 241104.
Först, M., *et al.*, 2013, Solid State Commun. **169**, 24.
Först, M., *et al.*, 2014a, Phys. Rev. B **90**, 184514.
Först, M., *et al.*, 2014b, Phys. Rev. Lett. **112**, 157002.
Först, M., *et al.*, 2015, Nat. Mater. **14**, 883.
Foucar, L., *et al.*, 2012, Comput. Phys. Commun. **183**, 2207.
Frank, M., *et al.*, 2014, IUCrJ **1**, 95.
Fraser, J., R. Sheffield, and E. Gray, 1986, Nucl. Instrum. Methods Phys. Res., Sect. A **250**, 71.
Frasinski, L. J., *et al.*, 2013, Phys. Rev. Lett. **111**, 073002.
Freund, I., and B. F. Levine, 1970, Phys. Rev. Lett. **25**, 1241.
Fromme, P., and J. C. Spence, 2011, Curr. Opin. Struct. Biol. **21**, 509.
Fromme, R., *et al.*, 2015, IUCrJ **2**, 545.
Fuchs, M., *et al.*, 2015, Nat. Phys. **11**, 964.
Fung, R., V. Shneerson, D. K. Saldin, and A. Ourmazd, 2009, Nat. Phys. **5**, 64.
Galayda, J., *et al.*, 2014, in the *International Particle Accelerator Conference 2014, TUCA01*.
Gallat, F.-X., *et al.*, 2014, Phil. Trans. R. Soc. B **369**, 20130497.
Galli, L., S.-K. Son, T. A. White, R. Santra, H. N. Chapman, and M. H. Nanao, 2015, J. Synchrotron Radiat. **22**, 249.
Ganter, R., *et al.*, 2010, SwissFEL-Conceptual design report, Technical Report (Paul Scherrer Institute (PSI), Villigen (Switzerland). Funding organisation: Paul Scherrer Institute (PSI), Villigen (Switzerland)).
Gati, C., *et al.*, 2014, IUCrJ **1**, 87.
Gaudin, J., *et al.*, 2012, Phys. Rev. B **86**, 024103.
Gaudin, J., *et al.*, 2014, Sci. Rep. **4**, 4724.
Gawelda, W., *et al.*, 2007, Phys. Rev. Lett. **98**, 057401.
Geddes, C. G. R., C. Toth, J. van Tilborg, E. Esarey, C. B. Schroeder, D. Bruhwiler, C. Nieter, J. Cary, and W. P. Leemans, 2004, Nature (London) **431**, 538.
Geloni, G., V. Kocharyan, and E. Saldin, 2011, J. Mod. Opt. **58**, 1391.
Ghiringhelli, G., *et al.*, 2012, Science **337**, 821.
Ginn, H. M., A. S. Brewster, J. Hattne, G. Evans, A. Wagner, J. M. Grimes, N. K. Sauter, G. Sutton, and D. I. Stuart, 2015a, Acta Crystallogr. Sect. D **71**, 1400.
Ginn, H. M. *et al.*, 2015b, Nat. Commun. **6**, 6435.
Glatzel, P., and U. Bergmann, 2005, Coord. Chem. Rev. **249**, 65.
Gleason, A. E., *et al.*, 2015, Nat. Commun. **6**, 8191.
Glenzer, S. H., and R. Redmer, 2009, Rev. Mod. Phys. **81**, 1625.
Glover, T. E., *et al.*, 2012, Nature (London) **488**, 603.
Glownia, J. M., *et al.*, 2010, Opt. Express **18**, 17620.
Gomez, L. F., *et al.*, 2014, Science **345**, 906.
Gorkhover, T., *et al.*, 2012, Phys. Rev. Lett. **108**, 245005.
Gorman, M. G., *et al.*, 2015, Phys. Rev. Lett. **115**, 095701.
Graaf, C. D., and C. Sousa, 2011, Int. J. Quantum Chem. **111**, 3385.
Graves, C. E., *et al.*, 2013, Nat. Mater. **12**, 293.
Grguras, I., *et al.*, 2012, Nat. Photonics **6**, 852.
Grübel, G., A. Madsen, and A. Robert, 2008, *Soft-Matter Characterization* (Springer, Heidelberg).
Gutt, C., *et al.*, 2012, Phys. Rev. Lett. **108**, 024801.
Hájková, V., *et al.*, 2011, Proc. SPIE Int. Soc. Opt. Eng. **8077**, 807718.
Halbach, K., 1985, J. Appl. Phys. **57**, 3605.
Hantke, M. F., *et al.*, 2014, Nat. Photonics **8**, 943.
Hara, T., *et al.*, 2013, Nat. Commun. **4**, 2919.
Harmand, M., *et al.*, 2013, Nat. Photonics **7**, 215.
Harmand, M., *et al.*, 2015, Phys. Rev. B **92**, 024108.
Hart, P., *et al.*, 2012a, Proc. SPIE Int. Soc. Opt. Eng. **8504**, 85040C.
Hart, P., *et al.*, 2012b, in *Nuclear Science Symposium and Medical Imaging Conference (NSS/MIC), 2012 IEEE* (IEEE, New York), pp. 538–541.
Hartmann, N., *et al.*, 2014, Nat. Photonics **8**, 706.
Hattne, J., *et al.*, 2014, Nat. Methods **11**, 545.
Hau-Riege, S. P., 2012, Phys. Rev. Lett. **108**, 238101.
Hau-Riege, S. P., and B. J. Bennion, 2015, Phys. Rev. E **91**, 022705.
Hau-Riege, S. P., R. A. London, H. N. Chapman, A. Szoke, and N. Timneanu, 2007, Phys. Rev. Lett. **98**, 198302.
Hau-Riege, S. P., *et al.*, 2010a, Phys. Rev. Lett. **105**, 043003.
Hau-Riege, S. P., *et al.*, 2010b, Phys. Rev. Lett. **104**, 064801.
Heimann, P., *et al.*, 2011, Rev. Sci. Instrum. **82**, 093104.
Helml, W., *et al.*, 2014, Nat. Photonics **8**, 950.
Hemsing, E., G. Stupakov, D. Xiang, and A. Zholents, 2014, Rev. Mod. Phys. **86**, 897.
Higginbotham, A., and D. McGonegle, 2014, J. Appl. Phys. **115**, 174906.
Hikosaka, Y., P. Lablanquie, F. Penent, T. Kaneyasu, E. Shigemasa, J. H. D. Eland, T. Aoto, and K. Ito, 2007, Phys. Rev. Lett. **98**, 183002.
Hill, J. P., and D. F. McMorrow, 1996, Acta Crystallogr. Sect. A **52**, 236.
Hirata, K., *et al.*, 2014, Nat. Methods **11**, 734.
Ho, P. J., C. Bostedt, S. Schorb, and L. Young, 2014, Phys. Rev. Lett. **113**, 253001.
Hoener, M., *et al.*, 2010, Phys. Rev. Lett. **104**, 253002.
Hoffmann, M. C., and J. J. Turner, 2012, Synchrotron Radiat. News **25**, 17.
Hogan, M. J., *et al.*, 1998, Phys. Rev. Lett. **81**, 4867.
Hruszkewycz, S. O., *et al.*, 2012, Phys. Rev. Lett. **109**, 185502.
Hu, W., S. Kaiser, D. Nicoletti, C. R. Hunt, I. Gierz, M. C. Hoffmann, M. Le Tacon, T. Loew, B. Keimer, and A. Cavalleri, 2014, Nat. Mater. **13**, 705.
Huang, Z., M. Borland, P. Emma, J. Wu, C. Limborg, G. Stupakov, and J. Welch, 2004, Phys. Rev. ST Accel. Beams **7**, 074401.
Huang, Z., and K.-J. Kim, 2007, Phys. Rev. ST Accel. Beams **10**, 034801.
Huang, Z., *et al.*, 2010, Phys. Rev. ST Accel. Beams **13**, 020703.
Hunter, M. S., *et al.*, 2014, Sci. Rep. **4**, 6026.
Ibrahim, M., R. Chatterjee, J. Hellmich, R. Tran, M. Bommer, V. K. Yachandra, J. Yano, J. Kern, and A. Zouni, 2015, Struct. Dyn. **2**, 041705.
Ishikawa, T., *et al.*, 2012, Nat. Photonics **6**, 540.

Johansson, L. C., *et al.*, 2012, Nat. Methods **9**, 263.
Johansson, L. C., *et al.*, 2013, Nat. Commun. **4**, 3911.
Johnson, S. L., *et al.*, 2012, Phys. Rev. Lett. **108**, 037203.
Kalantar, D. H., *et al.*, 2005, Phys. Rev. Lett. **95**, 075502.
Kang, H.-S., K.-W. Kim, and I. S. Ko, 2013, in the *International Particle Accelerator Conference 2013, 2074, Shanghai, China*.
Kang, Y., *et al.*, 2015, Nature (London) **523**, 561.
Kanter, E. P., *et al.*, 2011, Phys. Rev. Lett. **107**, 233001.
Kassemeyer, S., A. Jafarpour, L. Lomb, J. Steinbrener, A. V. Martin, and I. Schlichting, 2013, Phys. Rev. E **88**, 042710.
Kassemeyer, S., *et al.*, 2012, Opt. Express **20**, 4149.
Katayama, T., *et al.*, 2013, J. Electron Spectrosc. Relat. Phenom. **187**, 9.
Keedy, D. A., *et al.*, 2015, eLife **4**, e07574.
Kern, J., V. K. Yachandra, and J. Yano, 2015, Curr. Opin. Struct. Biol. **34**, 87.
Kern, J., *et al.*, 2012, Proc. Natl. Acad. Sci. U.S.A. **109**, 9721.
Kern, J., *et al.*, 2013, Science **340**, 491.
Kern, J., *et al.*, 2014, Nat. Commun. **5**, 1.
Khomskii, D., 2009, Physics **2**, 20.
Kim, J., B. Qiao, C. McGuffey, M. S. Wei, P. E. Grabowski, and F. N. Beg, 2015, Phys. Rev. Lett. **115**, 054801.
Kim, K.-J., 1986, Phys. Rev. Lett. **57**, 1871.
Kimura, T., Y. Sekio, H. Nakamura, T. Siegrist, and A. P. Ramirez, 2008, Nat. Mater. **7**, 291.
Kirian, R. A., *et al.*, 2011, Acta Crystallogr. Sect. A **67**, 131.
Koerner, L. J., H. T. Philipp, M. S. Hromalik, M. W. Tate, and S. M. Gruner, 2009, J. Instrum. **4**, P03001.
Kondratenko, A., and E. Saldin, 1980, Part. Accel. **10**, 207.
Koopmann, R., *et al.*, 2012, Nat. Methods **9**, 259.
Krejcik, P., Y. Ding, J. Frisch, Z. Huang, H. Loos, M. Wang, J. Wang, C. Behrens, and P. Emma, 2012, in *Proceedings of the 1st International Beam Instrumentation Conference*, edited by T. Mitsuhashi and A. Shirakawa (Joint Accelerator Conferences Website), pp. 441–444.
Krisch, M., and F. Sette, 2007, in *Light Scattering in Solid IX*, Topics in Applied Physics, Vol. 108, edited by M. Cardona, and R. Merlin (Springer, Berlin/Heidelberg), pp. 317–370.
Krupin, O., *et al.*, 2012, Opt. Express **20**, 11396.
Kubacka, T., *et al.*, 2014, Science **343**, 1333.
Kunnus, K., *et al.*, 2012, Rev. Sci. Instrum. **83**, 123109.
Kupitz, C., *et al.*, 2014a, Nature (London) **513**, 261.
Kupitz, C., I. Grotjohann, C. E. Conrad, S. Roy-Chowdhury, R. Fromme, and P. Fromme, 2014b, Phil. Trans. R. Soc. B **369**, 20130316.
Küpper, J., *et al.*, 2014, Phys. Rev. Lett. **112**, 083002.
Lablanquie, P., *et al.*, 2011, Phys. Rev. Lett. **106**, 063003.
Lawrence, R. M., *et al.*, 2015, Struct. Dyn. **2**, 041720.
Lee, N., T. Petrenko, U. Bergmann, F. Neese, and S. DeBeer, 2010, J. Am. Chem. Soc. **132**, 9715.
Lee, R. W., 2007, Report on the workshop to define the NNSA Mission Need, Report No. 10.2172/924177.
Lee, S., W. Roseker, C. Gutt, Z. Huang, Y. Ding, G. Grübel, and A. Robert, 2012, Opt. Express **20**, 9790.
Lee, S., *et al.*, 2013, Opt. Express **21**, 24647.
Lee, W. S., *et al.*, 2012, Nat. Commun. **3**, 838.
Lehmkühler, F., *et al.*, 2014, Sci. Rep. **4**, 5234.
Lemke, H. T., *et al.*, 2013, J. Phys. Chem. A **117**, 735.
Leone, S. R., 1999, Report of the Basic Energy Sciences Advisory Committee Panel on Novel Coherent Light Sources, Technical Report (U.S. Department of Energy).
Levantino, M., H. T. Lemke, G. Schirö, M. Glownia, A. Cupane, and M. Cammarata, 2015, Struct. Dyn. **2**, 041713.
Levantino, M., G. Schiro, H. T. Lemke, G. Cottone, J. M. Glownia, D. Zhu, M. Chollet, H. Ihee, A. Cupane, and M. Cammarata, 2015, Nat. Commun. **6**, 6772.
Levy, A., *et al.*, 2015, Phys. Plasmas **22**, 030703.
Li, J., Z. Shan, and E. Ma, 2014, MRS Bull. **39**, 108.
Liang, M., *et al.*, 2015, J. Synchrotron Radiat. **22**, 514.
Liu, W., *et al.*, 2013, Science **342**, 1521.
Loh, N. D., *et al.*, 2010, Phys. Rev. Lett. **104**, 225501.
Loh, N. D., *et al.*, 2012, Nature (London) **486**, 513.
Loh, N.-T. D., and V. Elser, 2009, Phys. Rev. E **80**, 026705.
Lomb, L., *et al.*, 2011, Phys. Rev. B **84**, 214111.
Loos, H., R. Akre, A. Brachmann, R. Coffee, F. Decker, Y. Ding, D. Dowell, S. Edstrom, P. Emma, and A. Fisher, 2010, Operational Performance of LCLS Beam Instrumentation, Report No. SLAC-PUB-14121 (SLAC).
Lubinski, G., Z. Juhász, R. Morgenstern, and R. Hoekstra, 2001, Phys. Rev. Lett. **86**, 616.
Lutman, A., *et al.*, 2014, Phys. Rev. Lett. **113**, 254801.
Lutman, A. A., R. Coffee, Y. Ding, Z. Huang, J. Krzywinski, T. Maxwell, M. Messerschmidt, and H. D. Nuhn, 2013, Phys. Rev. Lett. **110**, 134801.
Lyons, D. M., K. M. Ryan, M. A. Morris, and J. D. Holmes, 2002, Nano Lett. **2**, 811.
Lyubimov, A. Y., *et al.*, 2015, Acta Crystallogr. Sect. D **71**, 928.
Macchi, A., M. Borghesi, and M. Passoni, 2013, Rev. Mod. Phys. **85**, 751.
Mackinnon, A. J., *et al.*, 2004, Rev. Sci. Instrum. **75**, 3531.
Madey, J., 1971, J. Appl. Phys. **42**, 1906.
Maia, F. R., 2012, Nat. Methods **9**, 854.
Maia, F. R. N. C., T. Ekeberg, N. Timneanu, D. van der Spoel, and J. Hajdu, 2009, Phys. Rev. E **80**, 031905.
Mancuso, A., *et al.*, 2009, Phys. Rev. Lett. **102**, 035502.
Mangles, S. P. D., *et al.*, 2004, Nature (London) **431**, 535.
Mankowsky, R., *et al.*, 2014, Nature (London) **516**, 71.
Marchesini, S., *et al.*, 2008, Nat. Photonics **2**, 560.
Marinelli, A., A. A. Lutman, J. Wu, Y. Ding, J. Krzywinski, H. D. Nuhn, Y. Feng, R. N. Coffee, and C. Pellegrini, 2013, Phys. Rev. Lett. **111**, 134801.
Marinelli, A., *et al.*, 2015, Nat. Commun. **6**, 6369.
Maroncelli, M., J. Macinnis, and G. Fleming, 1989, Science **243**, 1674.
Martin, A. V., *et al.*, 2011, Proc. SPIE Int. Soc. Opt. Eng. **8078**, 807809.
Martin, A. V., *et al.*, 2012a, Opt. Express **20**, 13501.
Martin, A. V., *et al.*, 2012b, Opt. Express **20**, 16650.
McCusker, J. K., 2003, Acc. Chem. Res. **36**, 876.
McFarland, B. K., *et al.*, 2014, Nat. Commun. **5**, 4235.
McGonegle, D., D. Milathianaki, B. A. Remington, J. S. Wark, and A. Higginbotham, 2015, J. Appl. Phys. **118**, 065902.
McMahon, J., M. A. Morales, and C. Pierleoni, 2012, Rev. Mod. Phys. **84**, 1607.
Meyer, M., *et al.*, 2012, Phys. Rev. Lett. **108**, 063007.
Miao, J., P. Charalambous, J. Kirz, and D. Sayre, 1999, Nature (London) **400**, 342.
Miao, J., T. Ishikawa, I. K. Robinson, and M. M. Murnane, 2015, Science **348**, 530.
Milathianaki, D., *et al.*, 2013, Science **342**, 220.
Milton, S., *et al.*, 2001, Science **292**, 2037.
Minitti, M. P., *et al.*, 2015a, Phys. Rev. Lett. **114**, 255501.
Minitti, M. P., *et al.*, 2015b, J. Synchrotron Radiat. **22**, 526.
Mitzner, R., *et al.*, 2013, J. Phys. Chem. Lett. **4**, 3641.
Mizokawa, T., D. I. Khomskii, and G. A. Sawatzky, 2000, Phys. Rev. B **61**, 11263.

Moeller, S., *et al.*, 2015, J. Synchrotron Radiat. **22**, 606.
Montgomery, D. S., A. Nobile, and P. J. Walsh, 2004, Rev. Sci. Instrum. **75**, 3986.
Moshammer, R., *et al.*, 2007, Phys. Rev. Lett. **98**, 203001.
Mucke, M., *et al.*, 2015, New J. Phys. **17**, 073002.
Mukamel, S., D. Healion, Y. Zhang, and J. D. Biggs, 2013, Annu. Rev. Phys. Chem. **64**, 101.
Murphy, B. F., *et al.*, 2014, Nat. Commun. **5**, 4281.
Murphy, J., and C. Pellegrini, 1985, J. Opt. Soc. Am. B **2**, 259.
Murphy, J., and C. Pellegrini, 1990, *Laser Handbook* (North-Holland, Amsterdam).
Nagler, B., *et al.*, 2009, Nat. Phys. **5**, 693.
Nagler, B., *et al.*, 2015, J. Synchrotron Radiat. **22**, 520.
Nass, K., *et al.*, 2015, J. Synchrotron Radiat. **22**, 225.
Neutze, R., 2014, Phil. Trans. R. Soc. B **369**, 20130318.
Neutze, R., G. Brändén, and G. F. Schertler, 2015, Curr. Opin. Struct. Biol. **33**, 115.
Neutze, R., and K. Moffat, 2012, Curr. Opin. Struct. Biol. **22**, 651.
Neutze, R., R. Wouts, D. van der Spoel, E. Weckert, and J. Hajdu, 2000, Nature (London) **406**, 752.
Nogly, P., *et al.*, 2015, IUCrJ **2**, 168.
Nuhn, H.-D., 2009, in *31st International Free Electron Laser Conference*, edited by S. Waller, V. Schaa, M. Marx, L. Liljeby, J. Poole, and H. Owen (Stanford Linear Accelerator Center), pp. 714–721.
Nuhn, H.-D., *et al.*, 2015, Commissioning of the Delta Undualtor at LCLS, Report No. SLAC-PUB-16404 (SLAC).
Öberg, H., *et al.*, 2015, Surf. Sci. **640**, 80.
O'Regan, B., and M. Grätzel, 1991, Nature (London) **353**, 737.
Ostrom, H., *et al.*, 2015, Science **347**, 978.
Owen, R. L., E. Rudio-Piera, and E. F. Garman, 2006, Proc. Natl. Acad. Sci. U.S.A. **103**, 4912.
Palmer, D., *et al.*, 1997, in *Proceedings of the 1997 Particle Accelerator Conference*, Vol. 3 (IEEE, New York), pp. 2687–2689.
Park, H. J., *et al.*, 2013, Opt. Express **21**, 28729.
Park, J., D. Nam, Y. Kohmura, M. Nagasono, Y. Jeon, J.-B. Lee, T. Ishikawa, and C. Song, 2012, Phys. Rev. E **86**, 042901.
Patel, P. K., A. J. Mackinnon, M. H. Key, T. E. Cowan, M. E. Foord, M. Allen, D. F. Price, H. Ruhl, P. T. Springer, and R. Stephens, 2003, Phys. Rev. Lett. **91**, 125004.
Pedersoli, E., *et al.*, 2013, J. Phys. B **46**, 164033.
Pedrini, B., *et al.*, 2014, Phil. Trans. R. Soc. B **369**, 20130500.
Pellegrini, C., 1992, in Workshop Proceedings on Fourth Generation Light Sources, Stanford Synchrotron Radiation Laboratory, 92-02, p. 345.
Pellegrini, C., 2012, Eur. Phys. J. H **37**, 659.
Pellegrini, C., A. Marinelli, S. Reiche, 2016, Rev. Mod. Phys. **88**, 015006.
Peyrusse, O., 2012, Phys. Rev. E **86**, 036403.
Pierce, M. S., *et al.*, 2005, Phys. Rev. Lett. **94**, 017202.
Pietzsch, A., *et al.*, 2008, New J. Phys. **10**, 033004.
Ping, Y., *et al.*, 2013, Phys. Rev. Lett. **111**, 065501.
Plech, A., M. Wulff, S. Bratos, F. Mirloup, R. Vuilleumier, F. Schotte, and P. Anfinrud, 2004, Phys. Rev. Lett. **92**, 125505.
Rackstraw, D. S., *et al.*, 2015, Phys. Rev. Lett. **114**, 015003.
Radu, I., *et al.*, 2011, Nature (London) **472**, 205.
Raji, A. T., and S. Scandolo, 2014, High Press. Res. **34**, 250.
Ratner, D., *et al.*, 2015, Phys. Rev. Lett. **114**, 054801.
Redecke, L., *et al.*, 2013, Science **339**, 227.
Reiche, S., 1999, Nucl. Instrum. Methods Phys. Res., Sect. A **429**, 243.
Reinholz, H., G. Röpke, S. Rosmej, and R. Redmer, 2015, Phys. Rev. E **91**, 043105.
Remington, B. A., *et al.*, 2006, Mater. Sci. Technol. **22**, 474.
Robert, A., R. Curtis, D. Flath, A. Gray, M. Sikorski, S. Song, V. Srinivasan, and D. Stefanescu, 2013, J. Phys. Conf. Ser. **425**, 212009.
Rohringer, N., and R. Santra, 2007, Phys. Rev. A **76**, 033416.
Rohringer, N., *et al.*, 2012, Nature (London) **481**, 488.
Rolles, D., *et al.*, 2014, J. Phys. B **47**, 124035.
Rose, T. S., M. J. Rosker, and A. H. Zewail, 1989, J. Chem. Phys. **91**, 7415.
Roseker, W., H. Franz, H. Schulte-Schrepping, A. Ehnes, O. Leupold, F. Zontone, A. Robert, and G. Grübel, 2009, Opt. Lett. **34**, 1768.
Roseker, W., *et al.*, 2012, Proc. SPIE Int. Soc. Opt. Eng. **8504**, 85040I.
Rousse, A., *et al.*, 2001, Nature (London) **410**, 65.
Rudek, B., *et al.*, 2012, Nat. Photonics **6**, 858.
Saldin, E., E. Schneidmiller, and M. Yurkov, 1997, Nucl. Instrum. Methods Phys. Res., Sect. A **398**, 373.
Saldin, E., E. Schneidmiller, and M. Yurkov, 2000, *The Physics of Free Electron Lasers* (Springer-Verlag, Berlin).
Saldin, E., E. Schneidmiller, and M. Yurkov, 2004, Nucl. Instrum. Methods Phys. Res., Sect. A **528**, 355,
Salen, P., *et al.*, 2012, Phys. Rev. Lett. **108**, 153003.
Santra, R., N. V. Kryzhevoi, and L. S. Cederbaum, 2009, Phys. Rev. Lett. **103**, 013002.
Sauter, N. K., J. Hattne, R. W. Grosse-Kunstleve, and N. Echols, 2013, Acta Crystallogr. Sect. D **69**, 1274.
Sawaya, M. R., *et al.*, 2014, Proc. Natl. Acad. Sci. U.S.A. **111**, 12769.
Scagnoli, V., U. Staub, Y. Bodenthin, M. Garcia-Fernandez, A. M. Mulders, G. I. Meijer, and G. Hammerl, 2008, Phys. Rev. B **77**, 115138.
Schlichting, I., 2015, IUCrJ **2**, 246.
Schlichting, I., and J. Miao, 2012, Curr. Opin. Struct. Biol. **22**, 613.
Schlotter, W. F., *et al.*, 2012, Rev. Sci. Instrum. **83**, 043107.
Schmüser, P., M. Dohlus, J. Rossbach, and C. Behrens, 2014, *Free-Electron Lasers in the Ultraviolet and X-Ray Regime: Physical Principles, Experimental Results, Technical Realization*, Springer Tracts in Modern Physics (Springer International Publishing, Switzerland).
Schoenlein, R., *et al.*, 2015, New Science Opportunities Enabled by LCLS-II X-ray Lasers, Report No. SLAC-R-1053.
Schorb, S., *et al.*, 2012a, Appl. Phys. Lett. **100**, 121107.
Schorb, S., *et al.*, 2012b, Phys. Rev. Lett. **108**, 233401.
Schreck, S., *et al.*, 2014, Phys. Rev. Lett. **113**, 153002.
Schropp, A., *et al.*, 2013, Sci. Rep. **3**, 1633.
Schropp, A., *et al.*, 2015, Sci. Rep. **5**, 11089.
Seeman, J. T., 1991, Annu. Rev. Nucl. Part. Sci. **41**, 389.
Seibert, M. M., *et al.*, 2010, J. Phys. B **43**, 194015.
Seibert, M. M., *et al.*, 2011, Nature (London) **470**, 78.
Sellberg, J. A., *et al.*, 2014, Nature (London) **510**, 381.
Senn, H. M., and W. Thiel, 2009, Angew. Chem., Int. Ed. Engl. **48**, 1198.
Senn, M. S., J. P. Wright, and J. P. Attfield, 2012, Nature (London) **481**, 173.
Shenoy, G. K., and J. Stohr, 2003, LCLS The First Experiments, Report No. SLAC-R-611.
Shigemasa, E., J. Adachi, M. Oura, and A. Yagishita, 1995, Phys. Rev. Lett. **74**, 359.
Shintake, T., H. Matsumoto, T. Ishikawa, and H. Kitamura, 2001, Proc. SPIE Int. Soc. Opt. Eng. **4500**, 12.
Shintake, T., *et al.*, 2008, Nat. Photonics **2**, 555.
Shpyrko, O. G. *et al.*, 2007, Nature (London) **447**, 68.

Siders, C. W. C., A. Cavalleri, K. Sokolowski-Tinten, C. Tóth, T. Guo, M. Kammler, M. Hoegen, K. Wilson, D. Linde, and C. Barty, 1999, Science **286**, 1340.
Siefermann, K. R., *et al.*, 2014, J. Phys. Chem. Lett. **5**, 2753.
Siegbahn, K., 1981, Nobel Lecture 1981: Electron Spectroscopy for Atoms, Molecules, and Condensed Matter [http://www.nobelprize.org/nobel_prizes/physics/laureates/1981/siegbahn-lecture.html].
Sierra, R. G., *et al.*, 2012, Acta Crystallogr. Sect. D **68**, 1584.
Siewert, F., J. Buchheim, S. Boutet, G. J. Williams, P. A. Montanez, J. Krzywinski, and R. Signorato, 2012, Opt. Express **20**, 4525.
Smith, R., *et al.*, 2014, Nature (London) **511**, 330.
Snigirev, A., I. Snigeriva, V. Kohn, S. Kuznetsov, and I. Schelokov, 1995, Rev. Sci. Instrum. **66**, 5486.
Sokolowski-Tinten, K., *et al.*, 2003, Nature (London) **422**, 287.
Son, S.-K., H. N. Chapman, and R. Santra, 2013, J. Phys. B **46**, 164015.
Son, S.-K., and R. Santra, 2012, Phys. Rev. A **85**, 063415.
Son, S.-K., R. Thiele, Z. Jurek, B. Ziaja, and R. Santra, 2014, Phys. Rev. X **4**, 031004.
Son, S.-K., L. Young, and R. Santra, 2011, Phys. Rev. A **83**, 033402.
Sorokin, A. A., S. V. Bobashev, T. Feigl, K. Tiedtke, H. Wabnitz, and M. Richter, 2007, Phys. Rev. Lett. **99**, 213002.
Sousa, C., C. de Graaf, A. Rudavskyi, R. Broer, J. Tatchen, M. Etinski, and C. M. Marian, 2013, Chemistry **19**, 17541.
Spence, J. C., U. Weierstall, and H. N. Chapman, 2012, Rep. Prog. Phys. **75**, 102601.
Sperling, P., *et al.*, 2015, Phys. Rev. Lett. **115**, 115001.
Stapelfeldt, H., and T. Seideman, 2003, Rev. Mod. Phys. **75**, 543.
Starodub, D., *et al.*, 2012, Nat. Commun. **3**, 1276.
Staub, U., *et al.*, 2014, Phys. Rev. B **89**, 220401.
Stevenson, H. P., D. P. DePonte, A. M. Makhov, J. F. Conway, O. B. Zeldin, S. Boutet, G. Calero, and A. E. Cohen, 2014, Phil. Trans. R. Soc. B **369**, 20130322.
Stewart, J., and K. Pyatt, 1966, Astrophys. J. **144**, 1203.
Strüder, L., *et al.*, 2010, Nucl. Instrum. Methods Phys. Res., Sect. A **614**, 483.
Stupakov, G., 2009, Phys. Rev. Lett. **102**, 074801.
Suga, M., *et al.*, 2015, Nature (London) **517**, 99.
Sugahara, M., E. Mizohata, E. Nango, M. Suzuki, T. Tanaka, T. Masuda, R. Tanaka, T. Shimamura, Y. Tanaka, and C. Suno, 2015, Nat. Methods **12**, 61.
Sutton, M., S. G. J. Mochrie, T. Greytak, S. E. Nagler, L. E. Berman, G. A. Held, and G. B. Stephenson, 1991, Nature (London) **352**, 608.
Tenboer, J., *et al.*, 2014, Science **346**, 1242.
Thomas, H., *et al.*, 2012, Phys. Rev. Lett. **108**, 133401.
Tiedtke, K., *et al.*, 2009, New J. Phys. **11**, 023029.
Tiedtke, K., *et al.*, 2014, Opt. Express **22**, 21214.
Tobey, R. I., *et al.*, 2012, Phys. Rev. B **86**, 064425.
Togawa, K., T. Shintake, T. Inagaki, K. Onoe, T. Tanaka, H. Baba, and H. Matsumoto, 2007, Phys. Rev. ST Accel. Beams **10**, 020703.
Toll, J. S., 1956, Phys. Rev. **104**, 1760.
Tran, R., *et al.*, 2014, Phil. Trans. R. Soc. B **369**, 20130324.
Tremaine, A., *et al.*, 2002, Phys. Rev. Lett. **88**, 204801.
Trigo, M., *et al.*, 2013, Nat. Phys. **9**, 790.
Turner, J. J., 2014, in *Symposium U Magnetic Nanostructures and Spin-Electron-Lattice Phenomena in Functional Materials*, MRS Proceedings, Vol. 1636.
Turner, J. J., K. J. Thomas, J. P. Hill, M. A. Pfeifer, K. Chesnel, Y. Tomioka, Y. Tokura, and S. D. Kevan, 2008, New J. Phys. **10**, 053023.
Turner, J. J., *et al.*, 2011, Phys. Rev. Lett. **107**, 033904.
Turner, J. J., *et al.*, 2015, J. Synchrotron Radiat. **22**, 621.
Turner, J. L., *et al.*, 2014, in *Proceedings of FEL2014, Basel, Switzerland*, p. 337 [http://accelconf.web.cern.ch/AccelConf/FEL2014/papers/tub03.pdf].
Uervirojnangkoorn, M., O. Zeldin, A. Lyubimov, J. Hattne, A. Brewster, N. Sauter, A. Brunger, and W. Weis, 2015, eLife **4**, e05421.
Ullrich, J., R. Moshammer, A. Dorn, R. Dörner, L. P. H. Schmidt, and H. Schmidt-Böcking, 2003, Rep. Prog. Phys. **66**, 1463.
van der Schot, G., *et al.*, 2015, Nat. Commun. **6**, 5704.
Van Horn, H. M., 1991, Science **252**, 384.
Vartanyants, I. A., *et al.*, 2011, Phys. Rev. Lett. **107**, 144801.
Vinko, S. M., O. Ciricosta, and J. S. Wark, 2014, Nat. Commun. **5**, 3533.
Vinko, S. M., *et al.*, 2012, Nature (London) **482**, 59.
Vinko, S. M., *et al.*, 2015, Nat. Commun. **6**, 6397.
von Hámos, L., 1933, Ann. Phys. (Berlin) **409**, 716.
Wang, D., U. Weierstall, L. Pollack, and J. Spence, 2014, J. Synchrotron Radiat. **21**, 1364.
Wang, J.-M., and L.-H. Yu, 1986, Nucl. Instrum. Methods Phys. Res., Sect. A **250**, 484.
Wang, T. H., *et al.*, 2012, Phys. Rev. Lett. **108**, 267403.
Warshel, A., and M. Levitt, 1976, J. Mol. Biol. **103**, 227.
Weierstall, U., 2014, Phil. Trans. R. Soc. B **369**, 20130337.
Weierstall, U., J. C. Spence, and R. B. Doak, 2012, Rev. Sci. Instrum. **83**, 035108.
Weierstall, U., *et al.*, 2014, Nat. Commun. **5**, 3309.
Welch, J., *et al.*, 2011, in *Proceedings of the Free Electron Laser Conference 2011*, pp. 461–464.
Weninger, C., M. Purvis, D. Ryan, R. A. London, J. D. Bozek, C. Bostedt, A. Graf, G. Brown, J. J. Rocca, and N. Rohringer, 2013, Phys. Rev. Lett. **111**, 233902.
Wernet, P., *et al.*, 2015, Nature (London) **520**, 78.
White, T. A., A. Barty, F. Stellato, J. M. Holton, R. A. Kirian, N. A. Zatsepin, and H. N. Chapman, 2013, Acta Crystallogr. Sect. D **69**, 1231.
White, T. A., R. A. Kirian, A. V. Martin, A. Aquila, K. Nass, A. Barty, and H. N. Chapman, 2012, J. Appl. Crystallogr. **45**, 335.
White, W. E., A. Robert, and M. Dunne, 2015, J. Synchrotron Radiat. **22**, 472.
Winick, H., *et al.*, 1993, in *Proceedings of the 1993 Particle Accelerator Conference* (IEEE, New York), pp. 1445–1447, Vol. 2.
Wu, W., P. Nogly, J. Rheinberger, L. M. Kick, C. Gati, G. Nelson, X. Deupi, J. Standfuss, G. Schertler, and V. Panneels, 2015, Acta Crystallogr. Sect. F **71**, 856.
Wu, Y., Y.-m. Lin, A. A. Bol, K. A. Jenkins, F. Xia, D. B. Farmer, Y. Zhu, and P. Avouris, 2011, Nature (London) **472**, 74.
Xiang, D., *et al.*, 2010, Phys. Rev. Lett. **105**, 114801.
Xin, H., *et al.*, 2015, Phys. Rev. Lett. **114**, 156101.
Yabashi, M., H. Tanaka, and T. Ishikawa, 2015, J. Synchrotron Radiat. **22**, 477.
Yabashi, M., *et al.*, 2013, J. Phys. B **46**, 164001.
Yarkony, D. R., 1996, Rev. Mod. Phys. **68**, 985.
Yefanov, O., C. Gati, G. Bourenkov, R. A. Kirian, T. A. White, J. C. H. Spence, H. N. Chapman, and A. Barty, 2014, Phil. Trans. R. Soc. B **369**, 20130333.
Yoon, C. H., *et al.*, 2011, Opt. Express **19**, 16542.
Young, L., *et al.*, 2010, Nature (London) **466**, 56.
Yu, L. H., 1991, Phys. Rev. A **44**, 5178.
Zeldin, O. B., A. S. Brewster, J. Hattne, M. Uervirojnangkoorn, A. Y. Lyubimov, Q. Zhou, M. Zhao, W. I. Weis, N. K. Sauter, and A. T. Brunger, 2015, Acta Crystallogr. Sect. D **71**, 352.

Zener, C., 1951, Phys. Rev. **82**, 403.
Zewail, A. H., 1988, Science **242**, 1645.
Zewail, A. H., 2000, J. Phys. Chem. A **104**, 5660.
Zhang, H., *et al.*, 2015, Cell **161**, 833.
Zhang, W., *et al.*, 2014, Nature (London) **509**, 345.
Zhao, Z., *et al.*, 2012, Nat. Photonics **6**, 360.
Zhou, Q., *et al.*, 2015, Nature (London) **525**, 62.
Zhu, D., M. Cammarata, J. M. Feldkamp, D. M. Fritz, J. B. Hastings, S. Lee, H. T. Lemke, A. Robert, J. L. Turner, and Y. Feng, 2012, Appl. Phys. Lett. **101**, 034103.